ABSTRACT

MECHANICAL STRENGTH AND FRACTURE STUDIES
OF
PARTIALLY CRYSTALLIZED SELENIUM

By

Anwar Rahman Daudi

Partially crystallized selenium samples having various size and volume fractions of crystallites were obtained by heat treating amorphous selenium samples at 62°, 82° and 100°C for different lengths of time. Polarized-light microscopy was used to determine the size and volume fractions of the spherulites present in each specimen. Mechanical tests were carried out under three-point bending. Flexure strength of partially crystallized selenium decreases with increasing size and volume fraction of the crystallites. Scanning electron microscope studies of the fractured surfaces revealed that the fracture always started from spherulites. The fracture nucleates in the weak peripheral regions of the spherulites. Amorphous selenium shows inherent flaw size of about 5 μm. The flaw size in partially crystallized selenium varies from 10 to 100 μm, depending on the crystallite size. The flexure strength of amorphous and partially crystallized selenium can be determined from the mirror radius of fracture, provided the crystallites are less than 14 volume percent. The theoretical expressions of Maxwell and Eucken agree well with the experimentally determined variation of elastic modulus of partially crystallized selenium as a function of volume fraction of crystallites.

MECHANICAL STRENGTH AND FRACTURE STUDIES

OF

PARTIALLY CRYSTALLIZED SELENIUM

by

ANWAR RAHMAN DAUDI

A DISSERTATION

Submitted to
Michigan State University
in partial fulfillment of the requirements
for the degree of

DOCTOR OF PHILOSOPHY

Department of Metallurgy, Mechanics, and Materials Science

1974

To my Parents

ACKNOWLEDGMENTS

The author wishes to express his sincere appreciation to his advisor, Dr. K. N. Subramanian, whose guidance and assistance were invaluable throughout the course of this study. The interest, counsel, and time generously extended by Dr. D. J. Montgomery is gratefully acknowledged.

The writer appreciates the help and guidance offered by Dr. W. Hartmann (Physics) and Dr. G. Martin (Mechanical Engineering). Thanks are also extended to Dr. R. Summitt, Chairman, Department of Metallurgy, Mechanics, and Materials Science for financial assistance.

Finally, he wishes to thank his wife, Rafat, without whose help and consent this would not have been possible.

TABLE OF CONTENTS

Page

LIST OF TABLES

LIST OF FIGURES

Figure Page

Figure Page

I. INTRODUCTION

Many technologically important materials consist of more than one phase. The mechanical properties of such polyphase materials depend on the properties of the individual phases and the characteristics of the boundaries that exist between them. The size, shape, and distribution of the constituents, which depend on the boundary characteristics, play important roles in determining the behavior of the composite. These constituent phases could be crystalline or glassy. The crystalline phase has long-range order, whereas the glassy phase has definite first-order coordination but lacks long-range periodicity. In glasses, the crystallization required by equilibrium conditions has not taken place. As a result, the structure is similar to the liquid state. The polyphase materials containing crystalline materials in glassy matrices have some attractive physical properties. However, the basic mechanisms that control the mechanical behavior of such materials is not fully understood at present. The purpose of the present work is to study the mechanical properties of such a composite through a fairly simple glass-crystal model system, with the hope that the results may shed some light on the mechanical behavior of the glass-crystal materials in general.

In practice, the crystalline phases can be incorporated in a continuous glass matrix by one of the following methods:

1) by suitable heat-treatment schedules as in glass-ceramics, and

2) by hot pressing mixtures of glass and crystalline powders, as in glass-crystal composites.

The glass-crystal composites are ideal materials to verify the theoretical predictions for mechanical strength, since one can produce definite size, shape, and distribution of various crystalline phases in a given glassy matrix. On the other hand, intricate shapes can be produced with glass-ceramic, because objects can be shaped in the glassy state and then heat-treated to produce the crystalline phases. However, one does not have much control in the crystals that will crystallize out of a given glass matrix, with respect to their size, shape, or distribution. Although the glass-ceramic process is not ideally suitable for checking the theoretical predictions, it is the most useful means of producing objects for practical requirements. It would be ideal to have a system which can be formed by glass-ceramic means but can have all the controls on size, shape, and distribution of crystals as in glass-crystal composites. The material selected for the present study, selenium, satisfies these requirements.

The structure of amorphous selenium differs from the structure of glasses used in studies on glass-ceramics and glass-crystal composites. One can group glasses according to their internal structure; such a classification will include,

a) glasses with continuous network structure, such as in silicate and oxide glasses, and

b) glasses with randomly-distributed linear-chain structures such as organic polymers and elemental glass-formers like sulfur, selenium, and tellurium.

Mechanical-strength studies carried out so far in glasses, glass-ceramics, and glass-crystal composites have been on continuous-network structured glasses. However, the inorganic glasses having linear chain structure have not received any attention. The only materials having linear-chain structure, whose mechanical properties have been studied extensively, are the organic polymers, such as polystyrene and polyethylene. These studies would be of great help in understanding the mechanical behavior of inorganic polymers such as sulfur, selenium, and tellurium.

Selenium, having a linear-chain structure in glassy state, is an ideal model for studying the effect of crystallization on mechanical strength of a glass-crystalline material. Partially crystallized selenium contains two crystalline forms of selenium distributed in the amorphous matrix. Further, the transformation from completely amorphous to partially crystallized state is extremely important, since it produces excellent physical, electrical, and magnetic properties in selenium. The electronic industries have used amorphous selenium in a large number of applications such as switching, memory, light-sensing, and photoelectric devices. A very important area, however, the mechanical properties of selenium, has not been explored so far. The object of the present work is to study the role of crystallization on the mechanical strength and fracture behavior of partially crystallized selenium.

1.1 Morphology and Structural Details of Amorphous and Crystallized Selenium.

In the periodic table shown in Figure 1, selenium (atomic number 34) appears as a group VIA element. Its electronic configuration is

Fig. 1. Periodic table showing elemental glass formers. (shown by dark area)

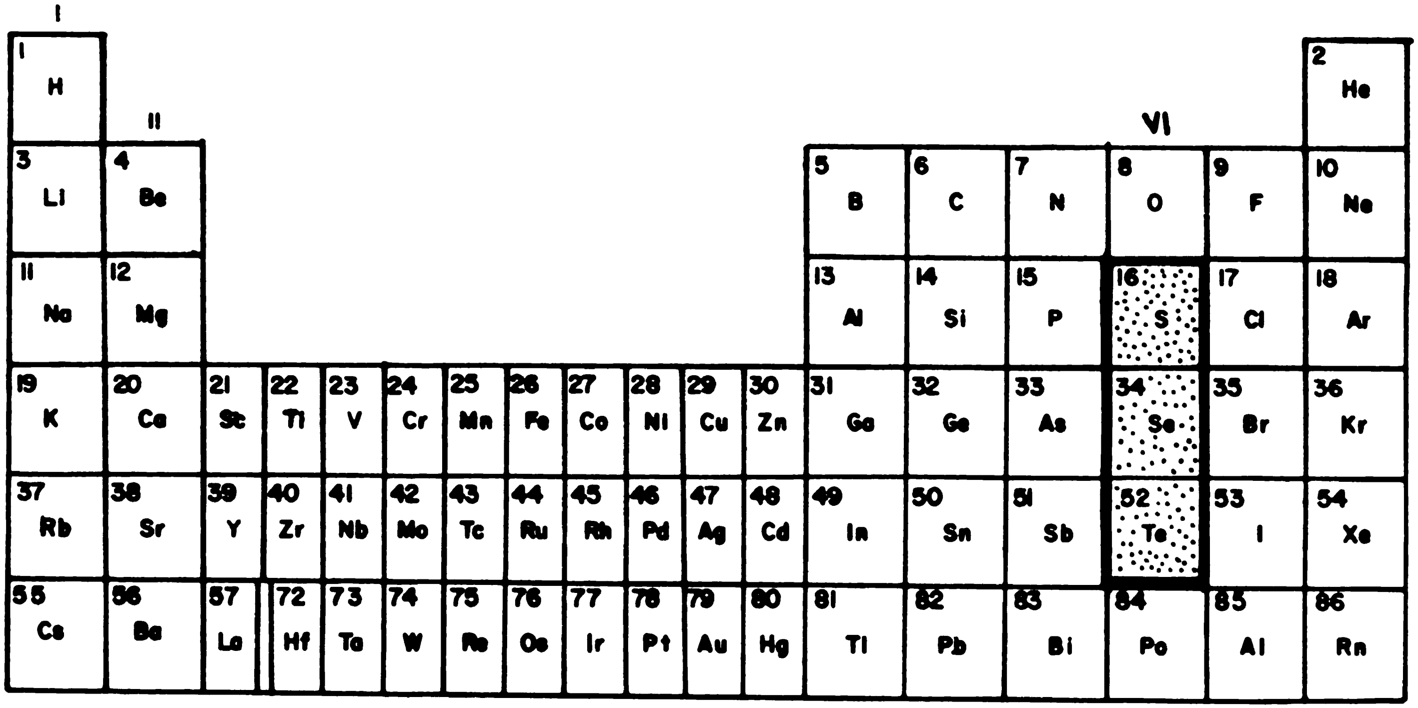

I	II														VI		
1 H																	2 He
3 Li	4 Be											5 B	6 C	7 N	8 O	9 F	10 Ne
11 Na	12 Mg											13 Al	14 Si	15 P	16 S	17 Cl	18 Ar
19 K	20 Ca	21 Sc	22 Ti	23 V	24 Cr	25 Mn	26 Fe	27 Co	28 Ni	29 Cu	30 Zn	31 Ga	32 Ge	33 As	34 Se	35 Br	36 Kr
37 Rb	38 Sr	39 Y	40 Zr	41 Nb	42 Mo	43 Tc	44 Ru	45 Rh	46 Pd	47 Ag	48 Cd	49 In	50 Sn	51 Sb	52 Te	53 I	54 Xe
55 Cs	56 Ba	57 La	72 Hf	73 Ta	74 W	75 Re	76 Os	77 Ir	78 Pt	79 Au	80 Hg	81 Tl	82 Pb	83 Bi	84 Po	85 Al	86 Rn

$1s^2 2s^2 2p^6 3s^2 3p^6 4s^2 4p^4$. It is a well-known small-band-gap semiconductor. Sulfur (atomic number = 16) and tellurium (atomic number = 52) also belong to this group. Sulfur, selenium, and tellurium are well-known glass-formers.

1.1.1 Structure of Amorphous Selenium

The structure of glassy selenium is found to be similar to that of molten selenium at temperatures slightly above the melting point. Caldwell and Fan[1] have shown by infra-red spectroscopy that the structure of glassy selenium and liquid selenium is a mixture of Se_8 rings and long polymeric chains with the atoms approximately equally distributed. There is some indication, however, that the structure is strongly dependent on the preparation procedure. When selenium glass is dissolved in cold CS_2 solution, only part of the glass can be dissolved. Briegleb[2] attributes this phenomenon to the existence of two different molecular species of selenium that could be present in the glassy state. The soluble portion was believed to be composed of Se_8 rings, as in monoclinic selenium, which is also soluble in CS_2; the insoluble species was thought to be long tangled chains, as in trigonal selenium, which is almost insoluble in CS_2. On this basis, Briegleb concluded that the relative amount of rings and chains in the selenium glass depend on its thermal history. Briegleb showed that only 45 weight percent of the selenium glass exists in the ring configuration when quenched from the melting point of trigonal selenium (220°C). Only 15 weight percent, however, exists in the ring configuration when quenched from 600°C. The break-up of Se_8 rings and subsequent polymerization into long chains at a higher temperature depends on the thermodynamic equilibrium that can be established between rings and chains. A knowledge of thermodynamic quantities for the above equilibrium state allows one to evaluate the average chain length and the concentration of Se_8 rings. The two important factors, then, that control the average number of chains and rings in glassy selenium are:

a) the temperature from which the liquid selenium is quenched to produce the glass, and

b) the time allowed for the melt to reach equilibrium in the molten condition.

1.1.2 Structures of Crystalline Selenium

In its crystalline allotropes, selenium--like sulfur--forms sp^2 hybrid bonds with its nearest neighbors. This bonding can lead to either long helical chains or to rings containing either six or eight atoms. Two distinct molecular units are present in the crystalline states, the ring (known as nonoclinic selenium) and the helical chain (known as trigonal selenium). Krebs[3,4] has discussed the structure of both sulfur and selenium in terms of cis-trans model of Foss[5]. In this bonding scheme, as shown in Figure 2, the first three atoms of both arrangements are positioned in a plane perpendicular to the plane of the paper. In the cis-configuration the fourth and fifth atoms are added in such a way as to lead to ring molecules (S_6, S_8, Se_8, etc.) whereas trans-bonding results in long helical chains. In a lighter element like sulfur, cis-bonding is favored, whereas in the heavier, more metallic group VIA elements, like selenium, tellurium, and polonium, there is an increasing tendency toward trans-bonding. Therefore in sulfur, the eight-membered ring characteristic of rhombic sulfur is more stable (although an unstable chain structure has also been observed)[6]. An unstable form of crystalline sulfur, composed of S_6 molecules, has also

Fig. 2. Cis-trans model of selenium proposed by Foss. (A) CIS-MODEL, (B) TRANS-MODEL. (See text for additional description.)

(A)

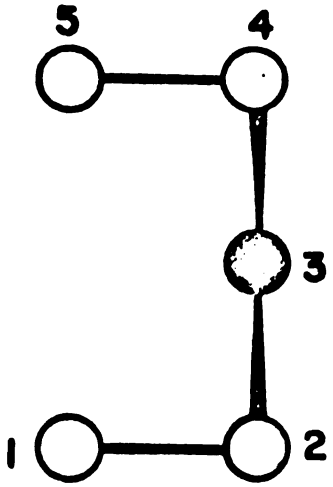

CIS

● PLANE ⊥ TO PAPER

(B)

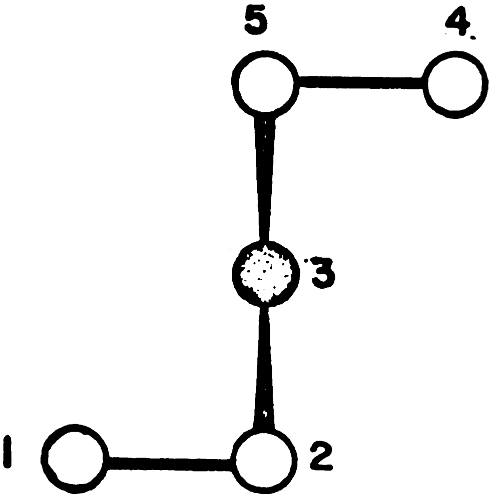

TRANS

been observed[7]. On the other hand, monoclinic selenium, formed by loose packing of Se_8 rings, is unstable and on heating above 70°C transforms to the trigonal form, which is composed of parallel helical chains. In agreement with the findings of Krebs[3] and Tunistra[6], no ring modifications of tellurium have been observed.

The trigonal selenium lattice is shown in Figure 3. It shows the parallel packing of helical chains. Each selenium atom within a chain is bonded to two nearest neighbors, and the Se-Se interatomic distance is 2.374A°. There are six next-nearest neighbors, resulting from atoms in neighboring chains, at a distance of 3.426A°. This is somewhat shorter than the distance[8] expected for van der Waals bonding (about 4.0A°), and hence implies a fairly weak chemical bond.

Selenium can exist in two monoclinic forms[3,8]. The structures of these two allotropes, α-selenium and β-selenium, are essentially the same, as shown in Figure 4. The difference exists in the crystalline packing of rings, the individual selenium rings being almost identical in both forms[9]. The average Se-Se bond length within a ring is 2.34A°. The next-nearest-neighbor distance, for atoms in neighboring rings, varies from atom to atom, the average distance being 3.48A°. The shortest inter-ring distance is 3.48A°, the largest is 3.99A°. The latter is of the magnitude expected for van der Waals bonding.

The two α and β monoclinic forms of selenium are unstable and will readily convert to trigonal selenium on heating above 70°C. According to Burnbank[10], the transformation begins at the points of closest packing where the structure is highly polarized by p- and d-electron interactions between neighboring molecules.

Fig. 3. (A) The trigonal selenium lattice.
(B) The chain structure of selenium.

(A)

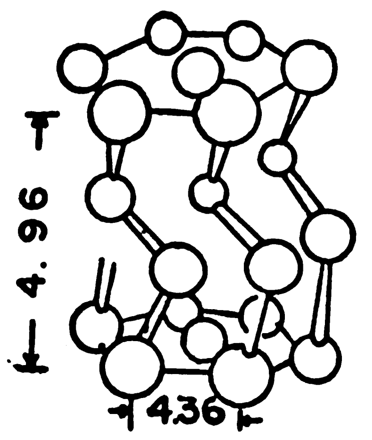

(B)

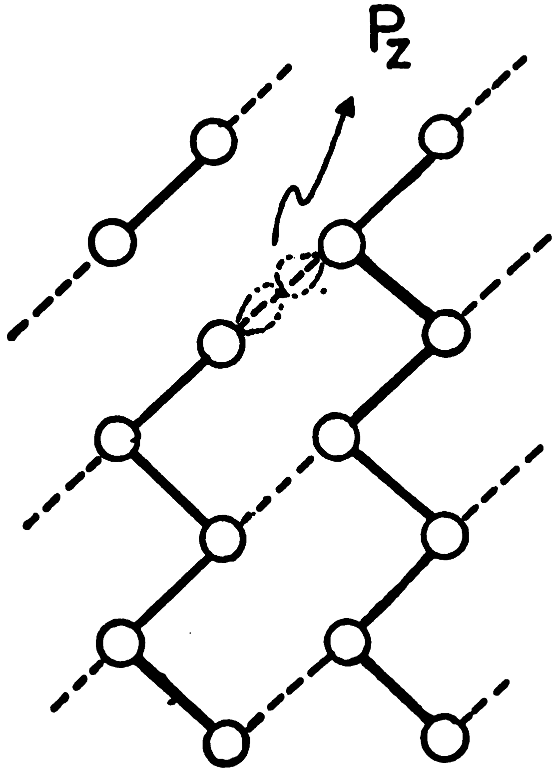

Fig. 4. (A) Ring structure of selenium.
(B) The monoclinic selenium lattice.

(A)

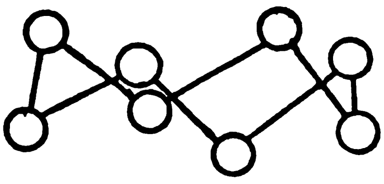

Se RING

(B)

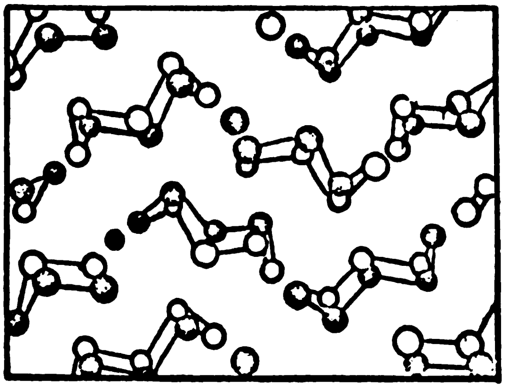

MONOCLINIC LATTICE

1.1.3 Morphology of Trigonal Selenium

The shape, size, and distribution of the trigonal selenium (hexagonal selenium) would be shown later to be important in determining the mechanical strength and fracture properties of selenium.

The crystallization of spherulites of selenium from amorphous selenium is now well-known[11,12,13]. From previous works on the morphology of these spherulites, their crystallization can be considered similar to those found in organic polymers. To check this possibility, a detailed structural examination of spherulites of selenium was undertaken by Fitton and Griffiths[13]. This study showed that crystallization of amorphous selenium occurs by the formation of lamellas in which the molecular axis lies across the wide face and perpendicular to the growth direction. At temperatures below about 200°C the lamellas grow radially from a common nucleus, branching noncrystallographically to produce a spherical crystalline mass. The theoretical selenium chain length in the quenched amorphous phase is much longer than the average lamella observed at large supercoolings[13]. This difference suggests that at the edges of the lamellas the chains must fold back to avoid stress accumulation due to interconnection of the two phases of different density. Fitton and Griffiths suggest that such an array of chain folds introduces a dilation of the lattice which is accommodated if the lamella twists. Where the effect is cooperative, such twisting within the radial array of lamellas is responsible for the spiral structure of selenium spherulites as shown in Figure 5.

1.1.4 Physical States of Amorphous Selenium

Amorphous selenium, as described in the previous sections, has a long-chain molecular structure, and as a result possesses unique

Fig. 5. The spiral structure of selenium spherulites (shown by X).


X
15 μm

typical

higher o

rmer of

he atmo

ration

nces b

therte

ces

he fiel

ationte

ately

elation

[illegible]

an ap

ild ma

ased b

and ang

sider

ifficul

be c

As

increa

seen

dyn

the ther

ted b

that

physical and mechanical properties. A single molecule of this inorganic polymer consists of repeated units linked by primary valence bonds, the number of repeating units being typically of the order of 10^5 atoms. The atoms bonded in the chain can rotate, the degree of freedom of rotation being dependent on the nature of atoms present in the chain. Besides the restriction to rotation within the molecule itself, the presence of other molecules in the bulk amorphous selenium also imposes restrictions on the molecular motion. These may be caused by the field forces of a van der Waals nature. The restrictions are maximized at low temperatures, when internal rotation is almost completely inhibited and the materials are hard and glassy. The glassy selenium is brittle, and has a high elastic modulus, approximately 0.7×10^{11} dynes per cm^2 at 32^oC. In amorphous selenium, the response to an applied stress is believed to be analogous to that found in other solid materials; it is associated with the change in internal energy caused by a stretching of interatomic bonds, or by the distortion of bond angles. In the "ideal" glassy state of selenium the molecules are considered to be randomly disposed. The random configuration is very difficult to realize in practice, and probably the deviations from it can be considered as a flaw in the glassy selenium.

As the temperature is raised, the thermal energy of the molecules is increased to the point where the barriers to motion can be overcome. As seen in Figure 6, in the rubbery region, the elastic modulus is low (10^7 dynes per cm^2 at 70^oC) and the extensibility is high. Because of the thermal energy of the molecules, the large deformation is accompanied by essentially free rotation about the primary valence bonds, so that the molecules adopt an extended configuration. In the rubbery region, the stress in a sample held at constant elongation increases with increasing temperature, but in the glassy region, the stress decreases with increasing temperature[14]. The transition between the two extremes is marked by a region of visco-elastic behavior as seen in Figure 6, where the properties are predominantly time-dependent. It is important that the glass-transition temperature (Tg) be defined, so that the mechanical strength determined in this study is independent of time of test. The glass-transition temperature in amorphous selenium is much lower than that in oxide glasses because in the former case the transition involves the breakage of low-energy van der Waals forces, rather than the breakage of the primary covalent bonds. From studies of properties of amorphous selenium by Eisenberg and Tobolsky[15] the glass-transition temperature is found to be 31.0°C.

The macroscopic elastic properties and the molecular response of glasses possessing long molecular chain structure such as amorphous selenium, are analogous to those of other solid materials.

1.2 General Considerations of Fracture and Strength of Amorphous and Partially Crystallized Selenium

To understand the state in which amorphous selenium exists in this investigation, a study of the physical states of the amorphous selenium was presented, in the preceding section 1.1.4. In the following section, 1.2.1, a review of the existing theories of mechanical strength and fracture properties of inorganic network-structured glasses is presented.

Fig. 6. (A) The physical states of amorphous selenium.
(B) The elastic modulus plotted as a function of time for amorphous selenium when heated to 30°, 50°, and 80°.

(A)

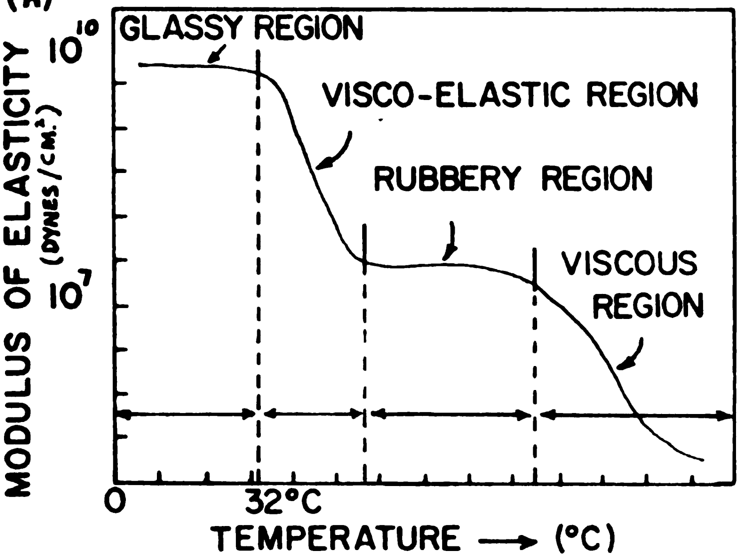

GLASSY REGION IS THE PHYSICAL STATE IN WHICH MECHANICAL TESTS WERE PERFORMED IN THIS WORK

(B)

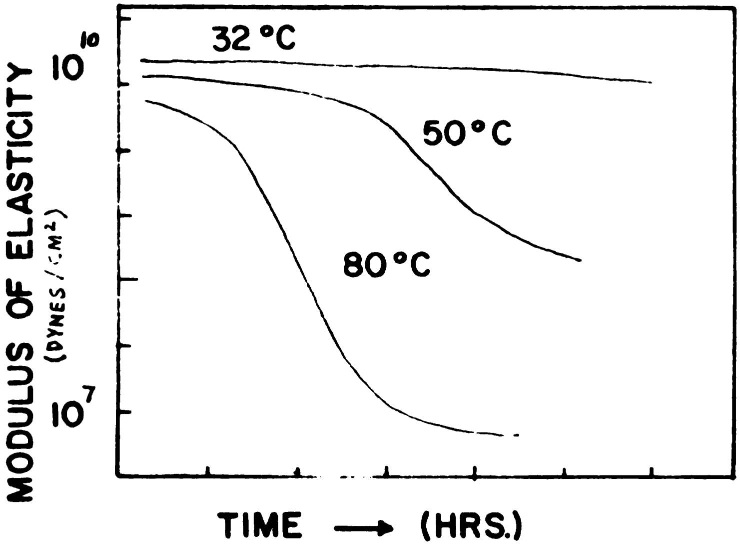

THE MECHANICAL PROPERTY TESTS WERE CARRIED OUT AT 25 - 26 °C

1.2.1 Strength and Fracture Studies on Amorphous Materials

Experimental studies on fracture and strength of amorphous materials have normally been carried out in silicate glasses having continuous network structure. As a result, the existing theories have been developed mainly from the results of silicate-glass studies.

Fracture and strength of amorphous materials are closely related to each other in a brittle material like glass. Fracture of a material implies separation into at least two integral parts; the strength of the material refers to the value of the externally applied stress necessary to achieve this result. In the fracture process, the bonds between the atoms present in tne newly-created surfaces are ruptured; the number of bonds involved can be computed from the structure of the materials. If the nature of bond and the force required to rupture one such bond are known, then the theoretical strength of the material can be calculated[16,17]. There have been several attempts to calculate the theoretical strength of amorphous materials[16,17]. Orowan[18] assumes that the stress (σ) in a rod under tensile loading changes with increasing interatomic spacing according to the relation $\sigma = \sigma_m \sin(2\pi x/\lambda)$, where σ_m is the maximum of σ, the theoretical strength of the material, and x is the increase in interatomic spacing. He equated the work done by fracture to the surface energy of the two new surfaces and derived the strength of glass to be

$$\sigma_m = (2E\gamma/a_o)^{\frac{1}{2}} \qquad [1]$$

where E, γ, and a_o are Young's modulus, fracture surface energy, and the interatomic distance, respectively. The fracture strength σ_m obtained after substituting suitable values if 1000 kg/mm^2 or

10^6 lb/sq.in. The strength values obtained in these studies are usually two or more orders of magnitude greater than those realized experimentally with conventional samples. One of the reasons for this discrepancy is that the method of calculation assumes that the stress is shared equally among all the interatomic bonds present in the cross-section. Then the fracture process would result in instantaneous separation of two planes in the material.

A reasonable assumption, therefore, is to consider that the stress applied is not uniformly distributed over the entire cross-section, and hence that there are regions of relatively high stress. When the applied stress creates a stress large enough to cause rupture of the interatomic bonds, the fracture will be initiated. Therefore, the discrepancy between the theoretical and observed values of the ultimate strength is explicable in terms of stress concentrations present in the samples tested.

Another approach to determine the strength of the material is to consider that physical defects exist in an elastic continuum. This consideration disregards the atomistic nature of the materials, and assumes that the material is completely isotropic except for areas of defects which act like stress raisers. Inglis[19] originated such an approach, and Griffith[20,21] developed the theory. Griffith assumed that the system could be represented by an infinite plate containing a central crack of length 2C, and with an energy criterion for instability derived the condition of applied stress at which the crack would increase in size and lead to fracture. According to Griffith, the critical tensile stress (T), that will cause fracture is given by

$$T = (2E\gamma/\pi c)^{\frac{1}{2}} \qquad [2]$$

where E is Young's modulus, and γ is the specific surface energy, i.e., the energy required to create unit area of surface. Breaking strength T, therefore, depends upon E, γ, and C. Griffith showed that for artificially-made cracks in a silicate glass, the product $TC^{\frac{1}{2}}$ equals 240 when T is in lb/in^2 and C in inches. From this value of $TC^{\frac{1}{2}}$, and the observed values of breaking strength, Griffith calculated that the glass contains cracks of length 2μ. It has been pointed out by Orowan that by equating the interatomic spacing "a_o" in Equation 1 to the radius of curvature ρ at the tip of a crack, and assuming $a_o = \pi C/2$ and $C = 2\mu$, Orowan's expression becomes the same as that of Griffith.

The two-dimensional model discussed above was later developed into a three-dimensional model[22,23]. A further development of this theory is to relate the flaw or defect of the material to the atomistic nature of real materials. These extensions and refinements, however, merely change the numerical constants in Griffith's expression, usually by a small factor, without influencing the functional relationship between the predicted critical stress (T), the material constants (E,γ), and the size of the defect (C).

According to the flaw theories, we can say that the ultimate strength observed in brittle material is not entirely an intrinsic property of the material. From Griffith's equation, the strength of a sample is determined by two factors:

1) the properties of the material, as defined by elastic modulus and the surface energy, and
2) the size of the defect which it contains.

The size of the crack does not depend on the property of the material

itself; it depends on the processing variables. Several distribution functions have been proposed[24,25] to account for the variations in the tensile strength of specimens that have undergone the same processing treatment. This approach provides a convenient way of representing the extent of variability of the data, but the distribution functions themselves do not have any fundamental significance, since they are believed to be caused by unknown or uncontrollable factors during production of the samples tested. A review[26] of the statistical treatment of strength data has been presented very recently, as discussed later in this section.

One serious objection that has been raised against the flaw theories is the representation of a real material with an atomistic structure as an elastic continuum. This representation is unreasonable, since the fracture process which occurs at the tip of the postulated flaw must involve the rupture of interatomic bonds, and on a molecular scale. As a result, the concepts of classical elasticity have no meaning.

To treat fracture phenomena directly in molecular terms, there exists an entirely different approach. Under an applied stress, the interatomic bonds in a body will be subjected to forces which will increase the mean interatomic distance. The characteristic relation of potential energy versus displacement for the atom pair will be so modified that less energy will be required to effect rupture of the bond. As a result, the probability of bond rupture will be increased. To relate the effect to observable quantities, some relation has then to be assumed between the interatomic forces and the applied stress. The problem of defining an instability condition at this point generates

different theories. The instability is attributed to differences in rates[27,28,29], probability[30,31], and nucleation[32]. The final equations provide relations between stress, time to failure, and temperature. These theories do not give the absolute value of fracture stress.

In the earlier portion of this section, it is shown that the fracture strength of brittle solids is dependent on the distribution of Griffith flaws in the material and on the probability that a flaw capable of initiating fracture at a specific applied stress is present. Various statistical theories for the strength of brittle materials have been proposed[33,34]. These theories assume that the number of the critical-size flaws present is related to the volume or surface of the specimen. Most of these theories have been devised to explain the fracture behavior of the materials when prepared by specific techniques. As a result, none of the theories can explain the behavior of all the materials. The best known of these statistical theories was developed by Weibull[33,34]. According to Weibull, the risk of rupture R is proportional to the function of stress and the volume of the body, and is given by

$$R = \int f(\sigma) dv \qquad [3]$$

where $f(\sigma)$ is a stress function and the dv is an infinitesimal volume. It is assumed that

$$f(\sigma) = (\sigma/\sigma_o)^m \qquad [4]$$

where σ_o is a "characteristic strength" dependent on the distribution function best fitting the data, and m is a constant related to the material homogeneity. The applied tensile stress $f(\sigma)$ was integrated over the volume of the body.

In conclusion, the two types of theories, based on atomistic or statistical basis, that have been proposed to explain the strength and fracture phenomena of amorphous materials, are not completely satisfactory in the light of the experimental evidence. But the flaw theories utilizing the statistical considerations appear to be widely accepted at present.

1.2.2 Strength and Fracture Studies on Glass-Crystalline Materials

All theories of strength and fracture properties of materials containing glass and crystalline phases have been experimentally verified with glass-ceramics and glass-crystal composites. If a material has a glass phase and a crystalline phase with a relatively small volume fraction of the latter, the glass forms a continuous matrix in which isolated crystals are dispersed. McMillan[35] noted that the strength of such materials would be dependent on the properties of the glassy phase. At high volume fractions of crystalline phase, the glassy phase may take the form either of a thin layer between adjacent crystals or, in some cases, of small isolated pockets. The strength of such materials would be independent of properties of the glassy phase. For all intermediate volume fractions, the strength of glass-crystalline materials would be dependent on the property of the individual phases. Only a few factors, such as volume and density of individual phases, can be averaged either on a weight or volume basis to give the properties of the composite. Mechanical strength of the glass-crystalline material is a complex function of a number of factors such as elastic moduli, thermal-expansion coefficients, size, shape, and distribution of the phases. These properties do not follow the simple additive rule.

Generally glass-ceramics are stronger than the conventional glasses, when tests are carried out on specimens that have received the same pre-abrasion treatment. Theoretical studies by Hashin[36], Hashin and Strikhman[37], Rosi[38,39], and Paul[40] have predicted increase of strength in glass-ceramics because of the increase in Young's modulus of the glass-crystalline material through the introduction of the crystalline phases having higher rigidities than the glass[41,42]. However, the observed increase of the elastic moduli is insufficient to account for the increase of mechanical strength. McMillan et al[43] experimentally verified this, by working on Li_2O-ZnO-SiO_2-P_2O_5 system and showed that strength of glass-ceramics increases from 1800 to 3500 kg/cm^2 when heat-treated at 600^oC for one hour, whereas the Young's modulus increases by a much smaller factor from 7.2×10^5 to 9.2×10^5 kg/cm^2.

Another possibility for the increase of strength of glass-ceramics may be due to differential thermal expansion of the crystalline and glassy phases. The difference of thermal-expansion coefficients could cause a favorable system of microstresses to develop there by enhancing the mechanical strength. This factor was verified experimentally by McCollister and Conrad[44]. Studies of the rough path of fracture in an intercrystalline material indicate that the fracture toughness and mechanical strength of the glass-ceramics are higher than that in the transgranular or fairly smooth fracture in completely crystalline and completely glassy materials, respectively. Hence the mode of fracture propagation in a glass-crystal composite could determine the strength of the glass-crystalline material.

If the thermal expansion of the crystalline phase is lower than that of the glassy phase, the stress at the glass-crystal interface in the radial direction is compressive in both phases. In the circumferential direction the stress is tensile in the glass phase and compressive in the crystalline phase. In this case, the fracture is transgranular; that means a crack approaching the crystal tends to propagate across the interface because the stresses normal to the glass-crystal interface are compressive. If the expansion coefficient of the crystal is higher than that of the glass, however, the stresses in the radial direction in both phases are tensile; in the circumferential direction, the stress is compressive in the glass, and tensile in the crystal. In this case, intergranular fracture is favored since the stress normal to the glass-crystal interface is tensile.

McCollister and Conrad[44] have investigated the influence of microstresses caused by differences in thermal-expansion coefficients on the fracture propagation in glass-ceramics, and have experimentally verified the general ideas discussed above. These investigations dealt with Li_2O-Al_2O_3-SiO_2 and CaF_2 in glass matrix. The expansion coefficient of the crystalline phase was 6×10^{-7} per °C, and that of the glassy phase was 41×10^{-7} per °C [44]. An average compressive stress of 17000 lb/in^2 ± 15% was measured by birefringence techniques, at the glass-crystal interface. As predicted on examination of the fracture surfaces, transgranular fracture was predominant in these materials. In the second system, calcium fluoride crystals were present in the glassy matrix. The crystalline phase had an expansion coefficient of 195×10^{-7} per °C, and the glassy phase had an expansion coefficient of 93×10^{-7} per °C [44]. The birefringence technique showed tensile stress of 43000 lb/in^2 ± 15% at the glass-crystal interface. In this case, as expected, the fracture was almost exclusively intergranular.

The stress concentration caused by the shape, size, and distribution of the crystalline phase in the glassy matrix may be of the greatest importance in determining the fracture stress. Hasselman and Fulrath[45] postulated that the effect of stress concentrations on the strength is governed by the relative size of the Griffith flaw and the volume of material over which the stress concentration acts. On this basis the effect of porosity on the strength of material can be analyzed in three distinct ways:

a) when the pore size is much larger than the flaw size (as in Hasselman and Fulrath, case I), flaws located near pores will be entirely within a stress-concentration field. A precipitous decrease in strength would be expected with the introduction of the first pore into the loaded area under such loading conditions.

b) as the size of the pore approaches the flaw size, (Hasselman and Fulrath, case II), the flaw will not be entirely located in areas of high stress concentration. A smaller decrease in strength would be expected than in case I.

c) when the pore size is much smaller than the flaw size (Hasselman and Fulrath, case III), the stress concentration field will no longer be large enough to affect the strength of the material appreciably, so only slight decreases of strength with porosity will be observed.

It is possible that the mechanical strength of glass-ceramics, like that of glasses, is dependent on the density and distribution of microcracks[46]. If this is the case, the mean sizes of the microcracks, and

thereby the mechanical strength, might be expected to be influenced by the microstructure of the glass-ceramic.

According to this approach[46] the mechanical strength of glass-ceramic (σ) is given by

$$\sigma = Kd^{-\frac{1}{2}} \qquad [5]$$

where K is a constant and d is the mean diameter of the grain. This suggests that crack length "C" of Griffith equations

$$\sigma = (\pi E\gamma/2C)^{\frac{1}{2}}$$

or

$$\sigma = Kc^{-\frac{1}{2}} \qquad [6]$$

to be proportional to or equal to the grain diameter. The critical flaws are therefore present within the crystalline grains and do not extend into the glass-crystal interface, and are therefore proportional to the circumference of the grains.

Another theory explaining the strengthening due to crystalline phase dispersed in glassy matrix is proposed by Hasselman and Fulrath[47]. They suggest that in glass-ceramics containing strong crystalline dispersions, the fracture will be initiated within the glass matrix. For such composites at a sufficiently high volume fraction of the crystalline phase, the maximum size of the flaws present in the glass may be restricted because of the presence of the dispersion. Hence the conclusion from this theory is that the flaws present in the glass matrix are terminated at the glass-crystal boundaries. The spacing between the crystals, or the mean free path in the glass phase, will therefore be a critical parameter in determining the mechanical strength. Let the mean free path be represented by "p", and

$$p = d(1-V)/V \qquad [7]$$

where V is the volume fraction of the crystalline phase and d is the diameter of the grain. There are two possible cases:

<u>Case I.</u> For small volume fractions and large grain diameters, the value of the mean free path will be larger than the flaw size, C, in the original glass, and therefore little effect of the crystalline dispersion on mechanical strength would be expected;

Case II. For higher volume fractions and small particle size, the mean free path becomes smaller than the original flaw size, and therefore the flaw size in the glass-crystal composite is controlled by the interparticle spacing in the glass matrix.

As a result, two regions exist--one in which the strength is not greatly affected by the crystalline dispersion since the interparticle spacing is too large, and a second in which the strength will be proportional to $p^{-\frac{1}{2}}$, if p, the mean free path, and c the flaw size, can be equated.

Freiman and Hench[48] determined the mechanical strengths of a series of glass-ceramics derived by heat-treating a glass of the molecular percentage composition Li_2O (33%) - SiO_2 (67%). The glass was given nucleation treatments at 475°C for times ranging from three to forty-eight hours, and was then heat-treated at 575°C to develop lithium disilicate crystals. The crystal sizes varied from 4.2 to 61 μm, the volume fractions ranged from 0.05 to 0.95, and the mean free paths varied from 2.8 to 178 μm. With Griffith's expression, they calculated a critical flaw size of 85 μm, and showed that in the early stages of crystallization when the strengthening effect was maximum, fracture is controlled by the initiation of flaws in the glassy phase rather than in the lithium disilicate spherulites. The mechanical strength was found to be proportional to $p^{-\frac{1}{2}}$ where p is the mean free path.

Hence there are five existing theories to explain the strengthening due to the crystalline phases present in a glassy matrix. These theories have explained the strengthening of glass by the introduction of crystalline phase in the following manner:

i) the strengthening is due to difference in elastic moduli of the crystalline phase and the glassy matrix.

ii) the strengthening is due to the difference in thermal-expansion coefficients of the crystalline phase and the glassy matrix.

iii) the strengthening is due to stress-concentration effects of the crystalline phase in the glassy matrix.

iv) the strength is affected by the number and size of the microcracks in the crystalline and the glassy phases.

v) the strengthening is due to the limiting of the size of the microcracks by the hard crystalline phase dispersed in the glass matrix.

1.2.3 Mode of Fracture in Glassy and Glass-Crystalline Materials

Experimental studies of fracture in glassy materials indicate that fracture originates at flaws or cracks of critical size, most of which are at the surface. The fracture propagates through the glass when the local stress at the tip of the crack exceeds a minimum value. The rate of propagation increases with crack length. Shand[49,50] claims that this rate of propagation of fracture reaches a limiting crack velocity at a particular crack length when the stress at the crack tip reaches a critical value. This limiting condition has been identified with the boundary of the mirror surface of the fracture.

The surface of fracture when examined under the microscope shows four prominent areas of fracture. Figure 7 illustrates diagramatically the type of surface observed.

1) The origin of the fracture which shows the flaw at which the fracture starts,
2) the mirror region of fracture which appears as a brightly polished region,
3) the rough region of fracture surrounds the mirror region, and
4) the hackled region of fracture, which clearly shows grooves radiating out from the origin of fracture.

These regions of fracture have been discussed in detail by Shand[49,50], Smekal[51], Murgatroyed[52], and Barson[53]. Smekal pointed out that there was no exact boundary between the rough zone and the mirror-like zone. More recently Gölz[54] studied the boundary between the mirror and rough regions of fracture, under the electron microscope, with the technique of Mahl, and concluded that the mirror zone also contained hackles, and that the roughness became increasingly small towards the origin of the fracture. The observance of the mirror zone was attributed to the inability of the instrument to resolve the fine-scale roughness. Smekal[51] has also noted that occasionally the glass rod under uniaxial tension may break from a sub-surface flaw, which results in a circular mirror area with hackle regions radiating from it.

Shand[55] has shown that there exists a close relationship between the fracture velocity and the topography of fracture surface. A typical fracture surface of borosilicate glass broken in bending is shown in

Fig. 7. Schematic illustrating the four prominent regions of fracture.

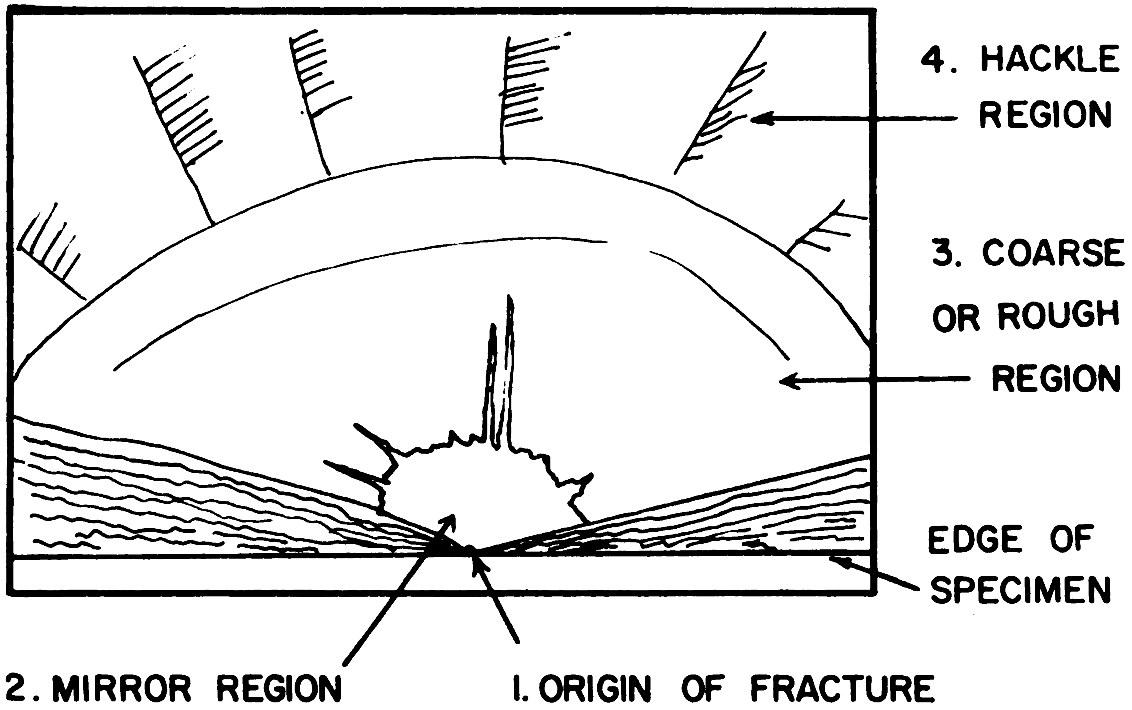
4. HACKLE REGION
3. COARSE OR ROUGH REGION
EDGE OF SPECIMEN
2. MIRROR REGION
1. ORIGIN OF FRACTURE

Figure 8. The fracture surface generally consists of four regions -- i) origin of fracture, ii) mirror, iii) rough, and iv) hackle regions. As the crack begins to propagate from the originating flaw, the fracture front moves along D - D and passes into a section in which the nominal stress decreases with distance. The extremities, however, follow the tension surface of the bar where initially the nominal stress remains constant. In both cases, the local stress concentration increases with the crack dimensions. The local stress distribution around the semicircular boundary of the crack is such that the stress is a maximum along the axis D - D. This results in a corresponding velocity difference, so that the crack spreads more in the lateral directions, and the crack boundary therefore is no longer semicircular, but tends to become semi-elliptical, as indicated by the "intermediate crack front." The local stresses at the fracture extremities soon reach the critical value, resulting in the transition to the violent phase of fracture as evidenced by triangular shattered areas. As a result of a certain segment's being shattered, the cross-sectional area that supports load is reduced. This reduction permits accelerated rates of deflection of the bar, and consequently a pronounced relaxation of the applied bending moment. The mirror surface shows the stage when fracture velocity is increasing; the boundary of the mirror and rough region is the stage when fracture velocity reaches the maximum value, which occurs when the stress reaches a critical value. The rough and hackle regions represent the latter stages of fracture when the applied bending moment is reduced, resulting in a reduction of fracture velocity. Walner lines, as defined by Walner[57], are lines on fracture surface formed by intercepts made by the elastic wave travelling at a constant velocity (as determined by the

physical properties of glass) and the fracture front. The closing of the Walner lines near the final crack front is characterized by a slowing down of the crack velocity. Hackles are produced by the fracture fronts from two different planes meeting in the plane of fracture.

It is generally accepted that there is some relationship that exists between the dimensions of the mirrored section of a glass fracture and the normal stress causing the fracture. Smekal[58] and his co-workers found that when circular glass rods are broken in tension, the nominal breaking stress in the section outside the mirror is essentially constant over a fairly wide range of mirror sizes. However, Terao[59] found that the breaking stress of glass rod σ_b is approximately proportional to the inverse square root of the mirror radius r;

$$\sigma_b = K/r^{\frac{1}{2}} \qquad [8]$$

where K is a constant of proportionality. This relation has been confirmed by Lavengood[60] and Orr[61] for specific types of fractures. Shand[49,50,51,56] has experimentally determined the breaking stress by utilizing the dimensions of the mirror area in the fracture process.

According to Shand[55], during the fracture of glass a critical velocity of crack propagation and a critical value of local stress are reached at the boundary of the mirror region. The nominal breaking stress (σ_b) is the critical stress (σ_m) of the glass divided by the stress-concentration factor of a crack with dimensions of the mirror surface; i.e.,

$$\sigma_b = \sigma_m/K \qquad [9]$$

and

$$K = f(D,r)/(\rho)^{\frac{1}{2}} \qquad [10]$$

$$f(D,r) = K\sqrt{\rho} = \frac{1.27\sqrt{r}\sqrt{D-r}}{\sqrt{1.27^2 r + (D-r)}} \qquad [11]$$

where ρ is the effective radius of the crack tip, D is the diameter of the rod, r is the mirror radius, and f(D,r) is a function dependent on the stress-concentration factor K. This stress-concentration factor K is determined by the size and geometrical form of the exposed surface of the fracture crack, and also by the characteristic deformation which occurs at the crack tip. In the case of glass it is estimated that if the flaw extends to a depth of only a few atom spaces, the effect on the size of the mirror surface, and consequently the change in the value of ρ, will be very small. For some glass-ceramic bodies, the extent of this plastic flow is apparently much greater, and therefore the change in the value of ρ will be very large. The factor f(D,r) can be computed from the geometrical form of the crack. The quantity $\sigma_m \rho^{\frac{1}{2}}$ can then be determined. Two possible limitations exist in taking the mirror radius as an indication of breaking stress:

i) the glass specimen should be free from residual stresses, and

ii) the dimensions of the mirror should be small in relation to those of the section of the specimen.

In Shand's bending tests, in the limiting case, the mirror radius is fifteen percent of the diameter of the specimen.

A typical mirror region of a glass fracture is shown in Diagram 8. Measurements of mirror areas were made by Shand[55] by optical microscopy. Mirror radii were measured along two axes OA and OB displaced 45° from the center line of the mirror. This procedure tends to compensate for local irregularities of the mirror locus and for the lack of symmetry.

This asymmetry tends to increase with the angle θ where θ is the angle shown in Diagram 8.

The mirror areas of glass fractures are formed because of the homogeneity and continuity of the body. Such considerations may be carried to the structural levels. The mirror areas of the glass-ceramics which are composed of large crystalline particles in the glassy matrix, lack homogeneity and continuity of the body. Consequently, the detailed record on the mirror surface is lost, and the fracture of the material extends over a large area. For certain ceramic materials, such as sintered alumina, no mirror region is formed at all. Shand[55] has plotted the mirror radius versus breaking stress for glass and glass-ceramic specimens in Figure 9. Distribution of variance of individual test points is shown in Figure 10. For eighty percent of the glass specimens the variance for fracture-stress values obtained from flexure tests are within ± 4%. It is much larger in the case of glass-ceramic specimens (approximately fifteen percent). This method is probably adaptable to some glass-ceramic bodies, but the results will be less accurate than in materials which are completely glassy.

1.3 Objective of this Research

The foregoing review of the present state of the theoretical and experimental studies of materials containing glass and crystalline phases shows that the factors affecting the strength and the mechanism of fracture of glass-crystalline materials are not clearly understood. In the present research an attempt was made to understand some of the basic factors that affect the mechanical properties of glass-crystalline materials with the hope that the results may elucidate the basic mechanism of fracture of brittle materials. The material chosen for the present

Fig. 8. Diagram of mirror surface of glass fracture showing inner and outer loci and axes of measurement (Shand[58])

Fig. 9. Plot of mirror radius versus breaking stress for glass and glass-ceramic specimens 0.457" in diameter. Curves represent corresponding mean values of $\sigma_m(\rho)^{\frac{1}{2}}$ for flexure (Shand[55]).

Fig. 10. Distribution of variances of individual test points from curves of Figure 9.

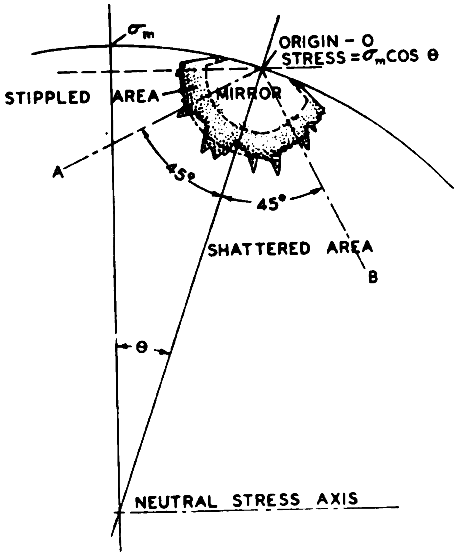

σ_m
ORIGIN - O
STRESS = σ_m COS θ
STIPPLED AREA
MIRROR
A
45°
45°
SHATTERED AREA
B
θ
NEUTRAL STRESS AXIS

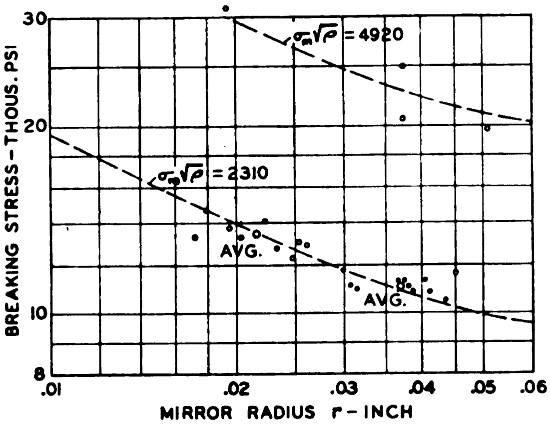

BREAKING STRESS - THOUS. PSI
30
20
10
8
$\sigma_m\sqrt{\rho} = 4920$
$\sigma_m\sqrt{\rho} = 2310$
AVG.
AVG.
.01
.02
.03
.04
.05
.06
MIRROR RADIUS r - INCH

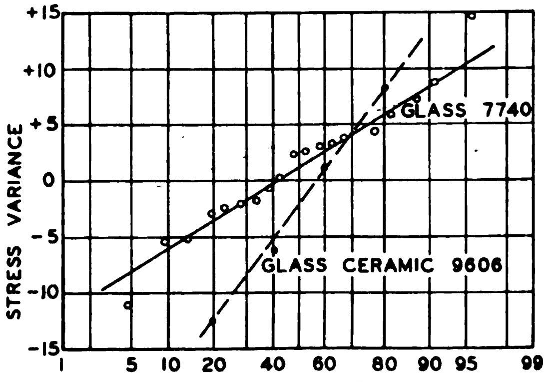

STRESS VARIANCE
+15
+10
+5
0
-5
-10
-15
GLASS 7740
GLASS CERAMIC 9606
1
5
10
20
40
60
80
90
95
99
CUMULATIVE PERCENT

investigation, moreover, is an elemental glass-former, whose mechanical properties are not well documented. As a result, one of the aims was to understand the mechanical properties of this elemental glass-former, selenium, a commercially-useful material, especially in the electronic industries.

The first objective of this investigation was to determine the mechanical properties of an inorganic linear-chain-structured glassy material, such as selenium, and to compare the results with those reported on glasses having continuous-network structure, such as oxide or silicate glasses. The second objective was to investigate the effects of the microstructure of partially crystallized selenium on its mechanical properties, and to correlate the results with reported investigations on glass-ceramic composites having various crystalline phases dispersed in the network-structured glassy matrices. Since varied microstructures can be produced in selenium by different heat-treatment schedules, it is possible to determine the effect of volume fraction, size, and distribution of various crystalline forms present in an amorphous matrix, on the mechanical properties of the material. The third objective was to determine the flexure strength of glassy and partially crystallized selenium from the dimensions of the mirror region of fracture surface. A further objective was to obtain an understanding of the basic fracture mechanism in such a glass-crystalline material. The fourth objective was to study the mechanical properties of selenium in bulk form rather than in thin-film form.

II. EXPERIMENTAL PROCEDURE

2.1 Sample Preparation

The selenium for this investigation was obtained from Kawecki Chemical Company in pellet form 99.99+% pure.

2.1.1 Safety Precautions

Selenium is an extremely hazardous material. According to Encyclopedia of Chemical Technology, one part per million of selenium hydride in the human body is fatal. Hence, the selenium was stored in sealed bottles, and was handled with extreme care. Melting was carried out in evacuated quartz tubes in a special furnace set-up described in detail later. This furnace was housed in an exhaust hood with exhaust fan operating when melting was in progress. Specimens were ground and polished under water to prevent the selenium dust from floating in the air. During handling, rubber gloves were worn; nose and mouth were covered by breathing-protection devices.

2.1.2 Melting of Selenium

The selenium was melted in special quartz tubes of the shape shown in Figure 11. These tubes were cleaned with a 10% solution of hydrofluoric acid, washed with distilled water, and then dried in a warm oven. This procedure removed the silicon dioxide particles present in these tubes. A white powdery film of silicon dioxide forms on both the inner and outer walls of the quartz tube during shaping with an

Fig. 11. Shape of quartz tube for melting selenium.

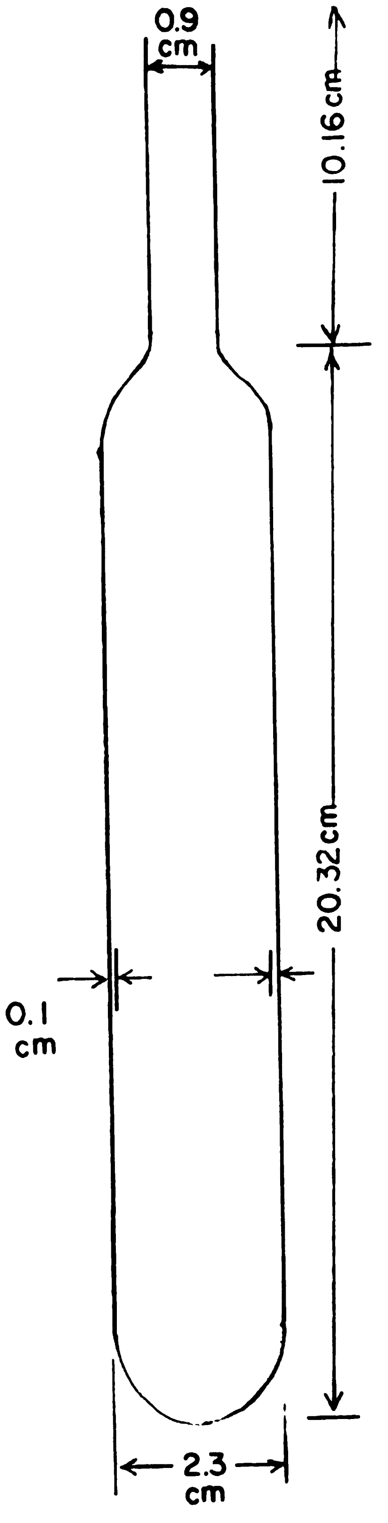
0.9 cm
10.16 cm
20.32 cm
0.1 cm
2.3 cm

oxy-acetylene torch. This film is easily soluble in the dilute hydrofluoric acid.

About 300 grams of selenium was put in each cleaned quartz tube. Approximately two inches of the tube length was left empty to accommodate selenium vapors. The tubes were attached to the evacuating system to achieve a vacuum of 10^{-3} mm Hg, and then sealed. Melting of selenium was carried out under the following schedule. The sealed tubes were rotated for 24 hours at 300°C in the horizontal position in the tube furnace set-up shown in Figure 12. A motor mounted on the frame of the furnace provided the rotary action of the quartz tube. The entire furnace set-up was housed in an exhaust hood and all operations were carried out by remote control. Upon completing rotation of the quartz tube containing selenium for 24 hours at 300°C, the furnace was made vertical. The furnace temperature was raised to 600°C and held for 4 hours in this position. At this temperature the liquid selenium was fairly fluid. The furnace was made horizontal and then vertical a number of times at this raised temperature, in order to drive locked vapors out of the melt. The temperature was taken back to 300°C, and the tube was held in the vertical position for another 20 hours. When the melt cools to 300°C, it becomes more viscous than the melt at 600°C. This lowering of temperature to 300°C helped in reducing the length of pipe that formed in the bulk glass obtained by quenching in ice water. Holding for 20 hours at 300°C helped in achieving an equilibrium structure for the melt before quenching. This step was essential to obtain bulk glass with reproducible structure and properties.

Fig. 12. Furnace set-up for melting selenium.

FURNACE SET-UP

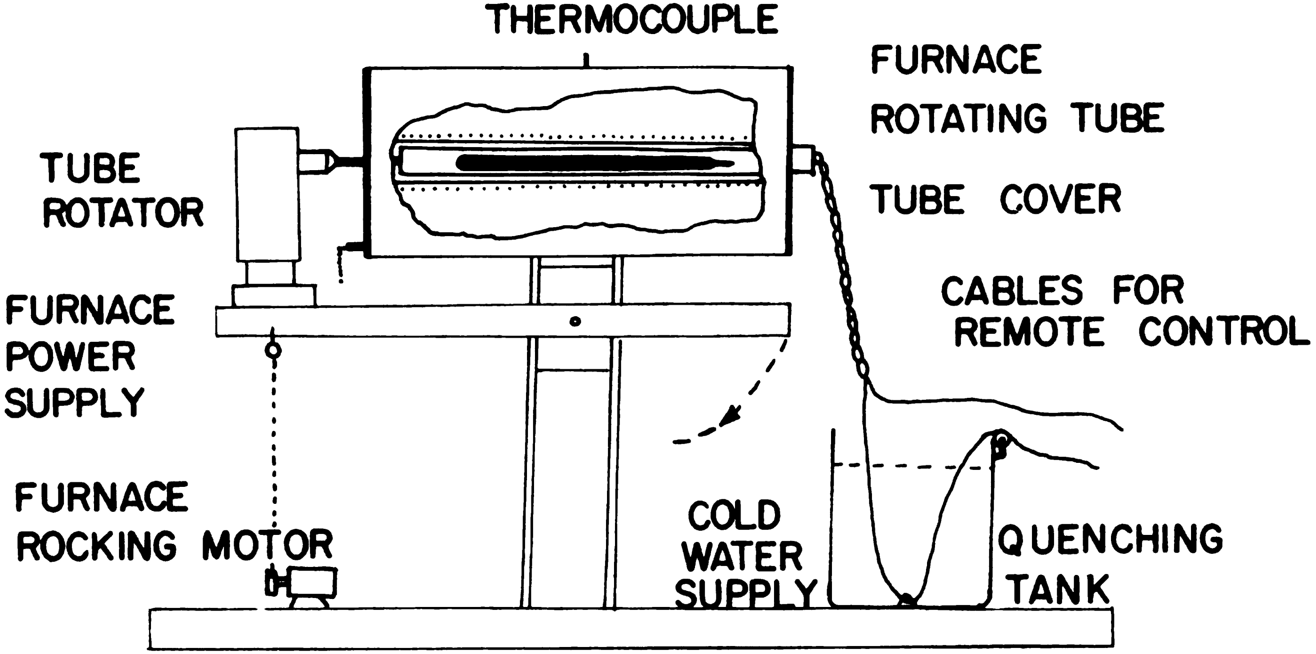

2.1.3 Quenching Technique

The quartz tube containing molten selenium was quenched in ice water. The quartz tube fell into a special holder in the ice-water bath which kept it vertical. The holder helped in allowing the melt to settle down in the tube, and provided a longer initial bulk glass sample. After allowing 5 minutes for the quenched sample completely to reach an equilibrium state, the quartz tubes containing selenium were taken out and stored in the freezer compartment of the refrigerator, where temperatures were far below the selenium glass-transition temperature (31 °C). With the above procedure, three bulk amorphous selenium samples were prepared. These three samples were labeled as melts A, B and C.

2.1.4 Cutting Bulk Amorphous Selenium Samples for Mechanical Testing

The quartz tube containing the bulk amorphous sample was mounted on a brass plate that fits in the vise of a high-precision cutting diamond saw. In the first mounting position, slabs of 0.25" X 6.5" X 0.75" size were produced. In the second mounting position the slabs were cut to the sizes required for mechanical tests and crystallization tests.

The cutting fluid for the sawing was a solution of Teenapol and water mixed in 1:8 ratio. The feed rate of the vise was regulated between 0.03-.04 inch per minute in order to minimize local heating of the specimen. The bulk samples and the cut specimens were studied under a polarized-light microscope to check for possible crystallization of the amorphous selenium. X-ray diffraction was also used to cross-check the results in some of the specimens. The specimens from the three melts (A, B and C) were kept separate throughout the investigation.

2.2 Heat Treatment of Specimens

A separate investigation, termed "crystallization study" was carried out to find the conditions to obtain uniform distribution of various size and volume fraction of crystallites in the amorphous selenium bend-test specimens.

2.2.1 Crystallization Study

The specimens were polished on 240- to 600-grit papers. The polishing papers were immersed in cold water in order to prevent the surface of the specimen from crystallizing during polishing. The final polish was given with 0.3 μ alumina and water suspension on cloth wheels. The specimens were polished to a mirror finish before heat treatment in order to facilitate uniform crystallization. They were wrapped in brass strips to keep the temperature on the faces of the specimens uniform. The heat-treating ovens were maintained at 100°C, 82°C, and 62°C. The accuracy of the temperature of the furnace was ± 2°C. The specimens were heat treated initially for various lengths of time. From the results of these tests, three durations at the above temperatures were selected to produce crystal size varying from 0 to 50.8 μm and volume fractions varying from 0 to 50%. The times selected were:

1) 45 min, 2) 1 hr, and 3) 1½ hr at 100°C.

1) 4 hr, 2) 6 hr, and 3) 8 hr at 82°C.

1) 200 hr, 2) 250 hr, and 3) 311 hr at 62°C.

Another objective behind selecting these three schedules was to see the effect of the two crystalline forms of selenium (the monoclinic and the trigonal) on the mechanical properties of partially crystallized selenium. During the 100°C heat treatment, a large number of trigonal selenium (spherulitic-shape) crystals crystallized out; the crystal size was also very large (50.8μm). A very small number of monoclinic crystals also crystallized out at this heat-treatment temperature. During the 62°C heat treatment, a large number of monoclinic selenium and a small number of trigonal selenium crystallized from the glassy matrix. The heat treatment at 82°C captures an intermediate condition. Various heat-treatment times were selected to grow different size and volume fractions of crystallites.

2.2.2 Heat Treatment of Mechanical Test Specimens

The mechanical test specimens (0.25 x 0.20 x 1.5") were heat treated in a manner similar to that of the crystallization-study specimens, to obtain the preselected volume fraction, size, and distribution of crystals. Every specimen was first ground on 240- to 600-grit papers. The papers were immersed in cold water, to prevent crystallization during polishing, and to catch the harmful selenium dust produced during grinding. The specimen surface could easily be mirror-polished by finishing on cloth wheels carrying 0.3μ alumina powder mixed with cold water. All sides of the specimens were checked for any crystallization by observation under polarized light. Brass strips were placed on each side of the specimen and tied by wire.

Three temperatures, 100°, 82°, and 62°C were maintained in heat-treating ovens. Groups of nine specimens, three specimens from each melt, were tied together. Three such groups were kept on brass slabs, very close to the thermometer registering the temperature. The group of nine specimens containing three specimens from each melt was taken out and quenched in ice water after the required heat-treatment time.

The heat-treated specimens were ground to remove about 0.02 inch from each surface to remove surface undulations and to eliminate effects of surface crystallization. The final polish was carried out very carefully to remove small scratches and fine pits. These specimens were studied with polarized-light microscopy to find the size, shape, and volume fractions of both the monoclinic and trigonal forms of selenium crystallized out of the amorphous matrix. The size of crystallites produced after specific heat-treatment schedule did not depend on the particular melt (A, B, or C). As a result, the specimens from the three melts were taken together to study the mechanical properties.

2.3 Quantitative Metallographic Analysis of Specimens

The microstructure obtained on the surface of specimens after heat treatment was analyzed by polarized-light microscopy. First, the crystalline forms of selenium were recognized, and then by a point-count method the volume fractions of these crystalline forms were measured. The size of the crystallites and their distribution was determined directly from the polarized-light photomicrographs.

2.3.1 Volume Fraction of Crystallites

A point-count method directly on the polarized-light microscope was acceptable for determining volume fraction of crystalline particles. In the point-count method of determining volume fraction, a grid having sixteen points on a reticule was used. The sixteen grid points were superimposed over the surface microstructure, and the number of grid points that fell on the crystalline phase were counted. Then,

$$\text{the volume fraction of the crystalline phase} = \frac{\text{number of grid points that fell on the crystalline phase}}{\text{total number of grid points}}$$

To minimize the errors, the volume fraction was determined after equal displacements of the grid points on the same side of the specimen. This process was repeated ten times. The volume fraction of the top and bottom surfaces of the specimens was determined by the above method, and average volume fraction was calculated from image observation.

The volume fractions of both monoclinic and trigonal forms of selenium were determined.

2.4 Mechanical Testing of Specimens

There are several methods of determining mechanical strength of brittle materials. The double-cantilever method is generally used to determine the fracture surface energy. In the present investigation, fracture surface energy was determined experimentally for the amorphous selenium and partially crystallized selenium by the method of Davidge and Tappin[62], as described in Section 2.4.3. Elastic modulus was determined from the load-deflection curve of three-point bend test, as shown in Section 2.4.2. The flaw size (C) was determined by analyzing the fractured surface of the specimens. According to Griffith's equation

$$\sigma_f = (\pi E\gamma/2C)^{\frac{1}{2}}$$

the fracture stress (σ_f) was determined by substituting the values for elastic modulus (E), fracture surface energy (γ), and flaw size (C), of amorphous selenium and partially crystallized selenium specimens. A more direct method of determining strength of glass-crystal composite material is the three-point or the four-point bend test.

In this work, the room-temperature (25°C) flexure strengths of partially crystallized selenium specimens were obtained by loading the specimens to failure, in a three-point bending device. Approximately 27 specimens were tested to obtain the data point for each crystal size and volume fraction. The flexure strength was calculated from the expression, $\sigma = Mc/I$, where σ is the flexure strength (calculated at outer fiber stress), M is the maximum bending moment, c is the distance from the surface to the neutral axis, and I is the moment of inertia of the cross section about the neutral axis. The four-point bending test could not be used in this investigation, because with hand polishing it was very difficult to get the opposite sides sufficiently parallel. In the attempts that were made to use the four-point bending test, it was noted that it was extremely difficult to have all the four knife edges in contact with the specimen at the beginning of test. Therefore, throughout this study, the flexure strength was determined by the three-point bend test.

2.4.1 Experimental Method to Determine Flexure Strength of Amorphous Selenium and Partially Crystallized Selenium

In a standard three-point bend-test fixture, the distance between the outer knife edges was set at 1.0 inch for the first set of tests. The broken pieces served as specimens for two additional tests at 0.5-inch span. Hence every specimen gave three results. The data obtained from specimens that broke off at points other than the center of the span were discarded. The knife edges were given a smooth radius of curvature of about 1/32 inch in order to prevent formation of micro-cracks which would initiate fracture at the contact points of the knife edges with the specimen. The tests were carried out on in Instron testing machine. The cross-head speed was 0.005 cm/min. The specimen always failed in 15 to 30 seconds. This time range was deliberately chosen to determine the short-time flexure strength of partially crystallized selenium specimens. The broken pieces of the specimens were held in a small catchment made of aluminum foil, and were carefully stored in a vacuum desiccator kept in a refrigerator, for fractograph studies.

2.4.2 Experimental Method to Determine Elastic Modulus of Amorphous and Partially Crystallized Selenium

Bars were deformed in three-point bending with 0.5-to-1.0-inch spans as described in the previous section. The fracture load and deflection and the specimen stiffness are defined in Figure 13, which shows a typical curve. Elastic moduli (E) of amorphous and partially crystallized selenium were determined from the stiffness, K, of the bars from the formula

$$E = K\ell^3/4bd^3 \qquad [13]$$

where K is the stiffness of the material, ℓ is the span of the specimen, b is the breadth of the specimen, and d is the depth of the specimen.

2.4.3 Experimental Method for Determining Fracture Surface Energy of Amorphous and Partially Crystallized Selenium

In the present investigation, the effective surface energy (γ_I) was determined by the following method. Three amorphous selenium specimens with c/d = .1875, .1067, .3333, and five of different volume fraction of crystallites with c/d = .2365, .2136, .2143, .3679, and .3670, were selected. Values of σ_F, the fracture stress, c, the notch depths, and E, the elastic modulus as determined from the notched-bar three-point bend test, were substituted in Equation 28 (Appendix A) to obtain the effective fracture surface energy (γ_I).

Fig. 13. Load-deflection curve for a typical brittle material (Davidge and Tappin[62]).

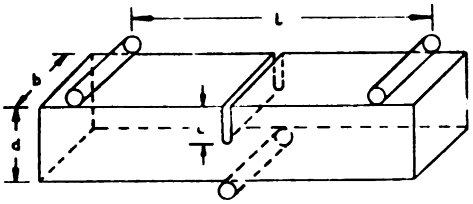
l
b
d
c

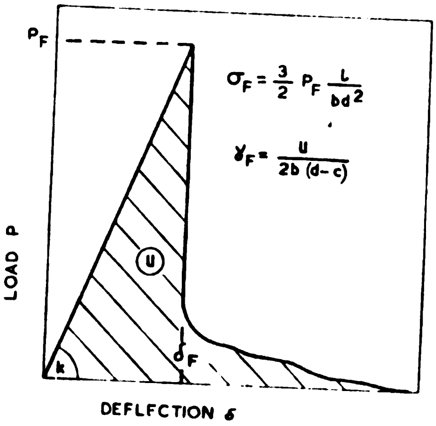
P_F
$\sigma_F = \frac{3}{2} P_F \frac{l}{bd^2}$
$\gamma_F = \frac{U}{2b(d-c)}$
U
k
δ_F
LOAD P
DEFLFCTION δ

2.5 Fractograph Studies

The fractured specimens were studied with a scanning-electron-microscope fractograph, by the method described in Section 2.5.1. To compute the breaking stress, the mirror radius was measured on each amorphous and partially crystallized specimen. The details of this method are described in Section 2.5.2.

2.5.1 Preparation of SEM Fractographs

One representative specimen for each temperature and time of heat treatment was mounted on the scanning-electron-microscope specimen holder with the fracture surface on top. The fractured surface was coated with carbon and then with Au-Pd alloy in an evacuated chamber. The specimens were continuously rotated so that a uniform layer of the coating was applied on the fractured surface. Generally a $100\mathrm{A}^{\mathrm{o}}$ thick layer was deposited to increase the secondary emissions from the surface of the specimens.

The fractographs were prepared under the following scheme. A lower (50X) magnification picture was taken to show the entire fracture surface. Then three fractographs were made at higher magnification to reveal the finer details of the regions of the same fracture surface. These areas were: i) origin of fracture, ii) mirror region, iii) rough region, and iv) the hackled region.

2.5.2 Measurement of Mirror Radius from the Fracture Surface of Amorphous and Partially Crystallized Selenium Specimens

After the flexure tests, the fractured specimens were mounted on the vertical stage of an optical microscope. The location of each fracture origin was determined. Two fracture fronts, more or less distinct, were observable on the mirror surface. The inner fracture front corresponded to the appearance of a stippled roughness on the surface. The outer fracture front represented the change-over from smooth-mirror region to a rough and shattered region showing deep furrows and highly irregular surface features. The method suggested by Shand[55] was to measure the mirror radius of the specimens from the origin to the inner fracture front. Measurements of mirrors were made with a 50-power microscope fitted with a calibrated reticule.

III. RESULTS

During the present experimental work, the mechanical-test specimens were heat-treated to preselected times and temperatures to obtain different volume fractions and sizes of crystallites in the amorphous matrix. The first section of this chapter contains general observations on the heat-treated specimens. The second section presents microstructural studies which are divided into two sub-sections, namely, qualitative and quantitative analysis. The third section contains the results of the bend tests. The fourth section presents SEM fractographs of the fractured surfaces.

3.1 General Observations

The specimens that were heat-treated at 100°C developed large, deep surface undulations and exhibited a high degree of softening during heat treatment. The specimen shapes were maintained by externally wrapping the specimens with strips. The specimen heat-treated at 62°C showed very few wrinkles on the surfaces. This tendency to form wrinkles during heat treatment can be explained on the basis of the difference in densities of the crystalline selenium (4.82 gm/cm^3 at 25°C) and the amorphous selenium (4.26 gm/cm^3 at 25°C). With heat treatment, the amorphous selenium transforms to the higher-density crystalline form and, as such, the specimens shrink. The undulation on the surface of specimens cannot be caused by difference in thermal-expansion coefficients (α) of the amorphous and crystalline forms of selenium, because the difference is extremely small ($\alpha_{\text{amorphous Se}} = 3.73 \times 10^{-5}$ cm/cm per $^{\circ}$C , $\alpha_{\text{crystalline Se}} = 3.79 \times 10^{-5}$cm/cm per $^{\circ}$C). Since the volume fraction of crystalline material formed in specimens that were heat-treated at 62°C was very small, the degree of shrinkage observed in the specimens was extremely small.

It was essential that the microstructure obtained for the same heat-treatment schedule in each melt should be the same. This reproducibility of microstructure is achieved if:

1) the initial bulk amorphous samples (melt A, B, and C) before heat treatment had similar frozen-equilibrium structure. The bulk glass preparation variables control this equilibrium structure. The temperature from which the bulk glass was quenched and the time allowed at this temperature for the liquid selenium to reach an equilibrium structure, were kept constant throughout this work. In this investigation, exactly the same preparation variables were maintained for these three melts. Each melt was quenched in an ice-water bath, after holding for twenty hours at 300°C
2) further, the cutting and heat-treatment processes should not introduce any variation in the microstructure.

The final check of the reproducibility of the microstructures is given in Figures 14 and 15, wherein the microstructure achieved after heat treatment in each melt is shown for every specimen. Two sides of the specimens were photographed. As can be seen, the microstructure is fairly reproducible and the crystallites are uniformly distributed on the two surfaces examined.

3.2 Microstructure Studies

3.2.1 Qualitative Analysis

The surface microstructure of specimens having the preselected heat-treatment schedule were observed by polarized-light microscopy. The microstructures of specimens heat-treated at 100°C for 45 min, 1 hr, and 1½ hr are shown in Figure 16. The monoclinic and the trigonal forms of selenium are seen in the microstructure (X - monoclinic, Y - trigonal). In Figure 17, the microstructure of specimens heat-treated at 82°C for 4 hours, 6 hours, and 8 hours are shown. In Figure 18, the microstructures of specimens heat-treated at 62°C for 200 hours, 250 hours, and 311 hours are shown. The details of microstructure show that above 70°C, that is, at 100°C and 82°C, there are a large number of trigonal crystals of selenium and a small number of monoclinic crystals present. The trigonal selenium appears as spherical bodies ("spherulites" shown by Y in Figure 16). The dark lines in the shape of spirals inside the spherulites have been structurally explained previously in Section 1.2. The monoclinic form of selenium appears as small white spots (shown by X in Figure 16) under the polarized light. Monoclinic selenium is a very unstable crystalline form of selenium; it transforms to trigonal selenium when heat-treated at 70°C. The monoclinic selenium can be clearly seen in the micrograph shown in Figure 18. At heat-treatment temperatures below 70°C, namely, 62°C, a large number of monoclinic crystals appear, as can be seen from Figure 18. In this figure there are a large number of spherulitic selenium crystals that have nucleated (approx. $100.57/\text{mm}^2$). This nucleation happens only after a prolonged heat treatment. The growth rate of the spherulitic crystals at 62°C heat treatment is extremely small (approx. 0.157 μm/hr). From the higher-temperature heat-treatment microstructure, the high growth rate (approx. 48.78 μm/hr) and small number of spherulites (approx. 40.23/mm^2) can be observed.

As seen from the surface microstructures shown in Figures 16, 17, and 18, there was no change in size and distribution of monoclinic selenium that could be observed during various heat-treatment schedules. However, the size and volume fractions of the spherulitic selenium changed considerably (starting from the lowest volume fraction 0 to 50.0%) during the heat-treatment schedules employed. The uniform distribution of crystallites can be observed from these microstructures. The sizes of crystallites were measured directly from the polarized-light micrographs. The sizes of the spherulites in any one specimen did not vary drastically. Therefore, the size of crystallites were obtained from an average value of the measured crystal sizes.

3.2.2 Quantitative Analysis

The size and distribution of crystallites were determined by polarized-light microscopy. The volume fraction of the crystallites was determined by a point-count method directly with the polarized-light microscope.

The volume fractions determined by this method are tabulated in Table 1. The size of the crystallites were measured from micrographs and are given in Table 2. The size of spherulitic selenium varies from 12.75 to 50.8μm. The smallest-size crystals exist in large number in specimens heat-treated at 62°C. The largest-size crystals exist in small numbers in specimens heat-treated at 100°C.

From Table 1, it can be seen that a very small volume fraction of monoclinic crystals exist in these specimens. These do not change appreciably with heat treatment (the volume fraction varies from 0.8 to 2.3%).

3.3 Bent-Test Results

The flexure strength and modulus of elasticity of the specimens was determined by the experimental method described in Sections 2.4.1 and 2.4.2.

3.3.1 Flexure Strength of Amorphous and Partially Crystallized Selenium

In Table 3 the flexure strength of each specimen has been presented on an individual basis. An average of the flexure strength readings was taken for the final analysis. Flexure-strength results of heat-treated specimens as shown in Table 3 for melt A, B, and C were plotted separately to check if they strongly depend on the particular melt. Figure 19 shows that the difference in melts does not change the trend of the plot. In Table 4, a comparison of the flexure strength determined with the 0.5- to 1.0-inch span in three-point bend test is shown. The results do not show any difference caused by the change of specimen lengths. In Figures 20, 21 and 22, the flexure strength of partially crystallized selenium is plotted as a function of volume fraction of spherulitic selenium for the specimens heat-treated at 62°, 82°, and 100°C. From Figure 20 it is observed that the flexure strength decreases drastically with increase of volume fraction at the heat-treatment temperature of 62°C. As can be seen from Figure 22, the flexure strength of specimens heat-treated at 100°C does not decrease as drastically as that for those heat-treated at 62°C. The decrease of strength at 82°C, as shown in

Figure 21, is intermediate between that of specimens treated at 62° and 100°C. Table 5 shows flexure strength and volume fraction of crystallites for constant size of crystallites. These results are plotted in Figures 23, 24, and 25. For the six sizes of crystals plotted, the flexure strength decreases with increase of volume fraction of crystallites. For the large size of crystals with $d_s = 25.4\mu m$, the flexure strengths tend to remain constant when volume fraction of crystallites increases from 2 to 20% as shown in Figure 25. The flexure strength decreases drastically for smaller size of crystallites ($d_s = 12.75$ and $15.78\mu m$), as can be seen in Figure 23. The decrease of flexure strength with increasing volume fraction of a medium-size crystal ($d_s = 22.22\mu m$) is intermediate between the large- and small-size crystals, as shown in Figure 24.

Table 6 shows flexure strength and size of crystallites for constant volume fraction of crystallites. These results are plotted in Figures 26, 27, and 28. As can be seen from these figures, the flexure strength decreases with increase of crystal size, for these five volume fractions of crystallites plotted. The flexure strength tends to decrease drastically with increase of size of crystals varying from 6 to 17μm for constant volume fractions $V_s = 2.09$ and 3.73%. For volume fractions $V_s = 8.13\%$ and 14.16%, the flexure strength plotted as a function of increasing size of crystals shows a minimum value of flexure strength corresponding to 18 and 26μm size of crystals, respectively.

3.3.2 Elastic Modulus of Amorphous and Partially Crystallized Selenium

The elastic moduli were determined from the load-deflection curves by the experimental method described in Section 2.4.2. Table 7 shows the elastic modulus (E) for each specimen. These results show that the elastic modulus increases with increase of volume fraction of crystallites. Table 8 shows the elastic modulus and volume fraction of crystallites for constant size of crystallites. The results are plotted in Figure 29 for crystal sizes of 12.75, 15.78, 19.06, 22.22, 25.4 and 50.8μm. For the smaller size of crystals (12.75, 15.78, 19.06μm), the elastic modulus increases sharply with increase of volume fraction of crystallites from 0 to 10%. The larger size of crystals (22.22, 25.4, and 50.8μm) shows a non-linear and a less drastic increase in elastic modulus than the previous volume fraction of crystallites in the range of 0 to 50%.

3.3.3 Fracture Surface Energy of Amorphous and Partially Crystallized Selenium

In Appendix A it is shown that fracture surface energy for amorphous and partially crystallized selenium can be determined with notched bars broken in three-point bending, according to the following expression:

$$\gamma_G = (1 - \nu^2)\pi \sigma_F{}^2 c/2E$$

where $\sigma_F = 3P_F L/2bd^2$ is the fracture stress, c is the notch depth, E is the modulus of elasticity, and ν is Poisson's ratio. Table 8 shows the fracture surface energy (γ) for amorphous specimens having notch depth c varying from .0175 to .037 inches (c/d = .1067 and .3333), and for partially crystallized selenium with volume fractions varying from 30 to 50% having notch depth c varying from .022 to .040 inches (c/d = .2136 to .3679). The fracture surface energy of amorphous selenium (γ = 1.62889 ergs/cm^2) decreases by a very small amount (γ = 1.49738 ergs/cm^2) with the addition of crystalline phase of selenium having a volume fraction approximately 50.0%. The fracture surface energy of glassy or crystalline selenium was therefore taken as $\gamma = 1.56312$ ergs/cm^2 for analyzing the present work

3.4 Fractograph Studies

3.4.1 Observations on SEM Fractographs

In Figures 30 to 44, the scanning electron microscope fractographs of amorphous specimen are compared for various specimens heat-treated at 62°, 82°, and 100°C for different lengths of time. In Figure 30, the fractured surface of the amorphous specimen is shown. The fracture originates from microcracks in the glassy matrix and propagates with no preferred direction, as is clearly seen from the higher-magnification photographs shown in Figure 30(B).

The SEM fractograph shown in Figure 31 shows the fracture surface of partially crystallized selenium obtained by heat treating at 62°C for 200 hr. This is a classic SEM fractograph showing the crack nucleated below the surface of the specimens. The three regions of fracture are clearly visible in these fractographs:

a) the origin of fracture, i.e., the fissure at which crack propagation started;

b) the smooth surface known as mirror area; and

c) a frosty band that forms the boundary of the mirror area which usually becomes more hackled with increasing distance from the origin of fracture.

In Figure 32 the SEM fractographs of partially crystallized selenium obtained by heat treating at 62°C for 250 hr are shown. The three regions of fracture (origin, mirror, and coarse regions) can be seen in Figure 32(A). Fracture originating from a spherulite near the surface of the specimen can be seen in Figure 32B. The hackle region is shown at 500X magnification in Figure 32C.

The fractographs of specimens heat-treated for 311 hours at 62°C are shown in Figure 33. With increase in volume fraction of crystallites, the fracture strength decreased and, as can be observed in the fractographs, the mirror region has increased. The coarse region of fracture exists only in small areas.

The SEM fractographs of specimens heat-treated at 100°C for 45 minutes are shown in Figure 34. The volume fraction of crystallites was about 7.0% and the flexure strength obtained for this specimen was 300 kg/cm^2. Again, the mirror region extends over a wide area; the coarse region of fracture exists only in small areas. As seen at higher magnification, say 1000x, the fracture originates at a spherulite. The spherulite in a coarse region momentarily holds the fracture from propagation. This delay results in a tail of mirror area at the spherulite. The spherulite in the final hackle regions of fracture is shown at 1000x.

With increased volume fraction of crystallites, the fracture tends to extend the mirror region, as can be seen in the fractograph prepared for specimens heat-treated at 100°C for one hour, shown in Figure 35. The origin of the fracture in this specimen was also at a spherulite.

Figure 36 shows the fractographs for the specimen heat-treated at 100°C for 1½ hours. The volume fraction of crystallites was about 50% and the strength had the lowest value, about 200 kg/cm^2. The mirror region has increased in size, compared with the previous specimens. Because of high volume fraction of crystallites, the fracture tends to have mixed mirror and coarse regions of fracture as seen at 500x magnification.

Figure 37 shows fractographs of specimens heat-treated at 82°C for 4 hours. The specimen edge is visible at (A) in the micrographs, the fracture originates at a crystallite as shown in Figure 37(B). The hackle region and the river patterns are clearly visible at the 500x magnification in Figure 37(D).

The fractographs for specimens heat-treated at 82°C for 6 hours are shown in Figure 38. The three regions of fracture are clearly visible in Figure 38(A). The origin of fracture is shown at higher magnification in Figure 38(B). The rough and hackle regions are seen in Figure 38(C) and (D) respectively.

Finally, the last fractographs in Figure 39 show the micrographs of specimens heat-treated at 82°C for 8 hours. With increase in volume fraction of spherulites, the fracture shows a large mirror area as seen in Figure 39(B). The rough region is clearly seen in Figure 39(C), the hackle region can be seen in Figure 39(D).

Figure 40 shows the finer details of fracture in and around a single spherulite. As can be seen from the fractograph, the fracture path is somewhere in the periphery of the spherulite. The core of the spherulite is intact, the glass-crystal interface showing no separation. This observation strongly supports the fact that the weakest region in the spherulite is the peripheral region of the spherulite.

In Figure 41(A) the path of fracture can be clearly seen to be through the peripheral region, at half the diameter of the spherulite. The size of spherulite shown in this figure is 22.22μm (medium size). The fractograph of Figure 41(B) shows the origin of fracture at two spherulites, which are in contact. It can also be noted that the spherulitic core is compact. The fracture path is again half way between the center and circumference of the spherulite.

The fractograph given in Figure 42(A) pictures the entire mirror region. The origin of fracture, on the surface of the specimen, was a spherulite (indicated by X). The picture shows only the pocket left by the missing spherulite. The spherulites indicated by Y show the highly compact cores whose diameters are approximately half the diameter of spherulites. In Figure 42(B) the river pattern in the hackle region can be seen. The core of the spherulite (approximately half the diameter of spherulite) can be clearly seen in Figure 43(A). The fracture path is along the weak peripheral region of the spherulite as illustrated in Figure 43(B). A classical picture showing two spherulites in the path of fracture is presented in Figure 43(C). The cleaved lamellas in the peripheral region of spherulite can be clearly seen in this figure. The core of the spherulite, as shown by X, is dense and compact.

In Figure 44(A), the path of fracture is very close to the periphery of the spherulite (small size $d_s = 15.87\mu m$). The core of the spherulite appears very dense. In Figure 44(B) the pocket left by the spherulite on the other half of the specimen is shown. This clearly indicates that the fracture in small-size crystals traverses very close to the glass-crystal interface. In Figure 44(C) cleaved lamellas in the peripheral region of a spherulite are shown. The core of the spherulite is approximately half the diameter of the spherulite (medium size $d_s = 22.22\mu m$).

TABLE 1

Volume Fraction of Crystallized Selenium in Heat-Treated Specimens

		Melt A % Volume Fraction of Crystals		Melt B % Volume Fraction of Crystals		Melt C % Volume Fraction of Crystals	
		Monoclinic	Spherulitic	Monoclinic	Spherulitic	Monoclinic	Spherulitic
100°C 45 min	S-1	X	6.25	1.1	2.67	1.2	5.93
	S-2	X	5.9375	1.4	3.125	1.6	5.31
	S-3	2.0	6.875	1.5	2.8375	1.1	6.88
1 hr	S-4	X	25.31	1.0	12.81	1.0	14.06
	S-5	1.3	23.44	X	X	0.9	14.66
	S-6	0.9	18.13	0.7	15.93	0.6	16.25
1½ hr	S-7	1.0	45.00	0.7	24.06	0.3	48.44
	S-8	X	X	X	X	X	X
	S-9	X	X	1.3	33.75	1.0	40.63
82°C 4 hr	S-1	1.0	2.81	0.9	4.83	0.8	33.75
	S-2	1.4	2.19	1.2	6.56	1.4	6.875
	S-3	0.8	3.86	1.3	3.44	1.3	6.32
6 hr	S-4	1.2	5.0	1.4	10.0	1.0	11.88
	S-5	0.9	6.25	0.9	5.11	1.0	13.61
	S-6	1.1	5.04	X	X	1.1	10.31
8 hr	S-7	1.2	10.63	1.1	14.38	X	X
	S-8	1.2	12.19	1.0	12.19	0.9	15.94
	S-9	1.4	11.88	1.0	12.19	1.1	18.44
62°C 200 hr	S-1	1.2	0.2	1.0	0.2	1.0	1.2
	S-2	X	X	0.7	X	X	X
	S-3	1.2	X	0.8	X	X	X
250 hr	S-4	1.1	0.7	2.4	0.9	0.9	2.6
	S-5	1.8	0.6	2.2	0.5	1.4	2.4
	S-6	1.3	0.5	1.8	0.5	1.1	2.2
311 hr	S-7	1.5	1.5	2.3	0.7	1.0	5.25
	S-8	1.4	3.5	X	3.3	0.6	X
	S-9	X	2.2	X	X	0.8	5.6

X - Indicates Lack of Data Owing to Experimental Problems

TABLE 2

Size of Crystallites in the Heat-Treated Selenium Specimens

			Average Size of Spherulites of Selenium Melt A (μm)	Average Size of Spherulites of Selenium Melt B (μm)	Average Size of Spherulites of Selenium Melt C (μm)
100°C	45 min	S-1	15.87	12.75	15.87
		S-2	12.75	12.75	15.87
		S-3	19.05	12.75	15.87
	1 hr	S-4	31.75	22.22	22.22
		S-5	25.14	22.22	22.22
		S-6	31.75	19.05	22.22
	1½ hr	S-7	50.80	38.10	50.80
		S-8	X	50.80	50.82
		S-9	X	44.45	50.82
82°C	4 hr	S-1	19.05	19.05	19.05
		S-2	19.05	19.05	19.05
		S-3	19.05	19.05	19.05
	6 hr	S-4	22.22	25.40	22.22
		S-5	22.22	25.40	22.22
		S-6	22.22	25.40	22.22
	8 hr	S-7	25.40	31.75	25.40
		S-8	25.40	31.75	25.40
		S-9	25.40	31.75	25.40
62°C	200 hr	S-1	12.75	6.35	12.75
		S-2	12.75	9.52	X
		S-3	12.75	9.52	12.75
	250 hr	S-4	15.80	15.87	15.80
		S-5	15.80	15.87	15.80
		S-6	15.80	15.87	15.80
	311 hr	S-7	25.40	25.40	25.40
		S-8	25.40	25.40	25.40
		S-9	25.40	25.40	25.40

TABLE 3

Flexure Strength of Amorphous and Partially Crystallized Selenium for Melts A, B, and C

			MELT A		MELT B		MELT C	
			Volume Fraction V_f(%)	Flexure Strength σ_f(kg/cm^2)	Volume Fraction V_f(%)	Flexure Strength σ_f(kg/cm^2)	Volume Fraction V_f(%)	Flexure Strength σ_f(kg/cm^2)
100°C	45 min	S-1	8.25	244.31	3.77	349.08	7.14	267.53
		S-2	7.94	332.01	4.53	273.18	6.91	334.19
		S-3	8.88	295.62	3.34	241.72	7.98	242.07
	1 hr	S-4	26.31	210.03	13.81	254.49	15.06	278.12
		S-5	24.74	284.26	15.22	324.85	15.56	299.71
		S-6	19.03	180.36	16.63	317.88	16.85	198.34
	1½ hr	S-7	46.00	227.13	24.76	230.94	48.74	X
		S-8	X	X	29.91	223.59	45.19	232.26
		S-9	X	X	35.05	238.65	41.63	186.20
82°C	4 hr	S-1	3.81	455.78	5.73	219.94	4.55	371.14
		S-2	3.59	251.57	7.76	394.47	8.28	350.96
		S-3	4.66	362.83	4.74	329.91	7.62	308.90
	6 hr	S-4	6.20	360.40	11.4	272.00	12.88	244.96
		S-5	7.15	275.08	6.01	346.61	14.61	279.96
		S-6	7.04	313.87	8.70	363.90	11.41	308.48
	8 hr	S-7	11.83	253.59	15.48	331.64	18.19	151.22
		S-8	13.39	279.57	13.19	334.30	16.84	328.27
		S-9	13.28	185.31	13.19	233.50	19.54	269.89
62°C	200 hr	S-1	1.4	X	1.2	412.16	2.2	438.61
		S-2	1.4	292.33	0.9	342.26	2.17	380.58
		S-3	1.4	388.36	0.8	344.51	2.15	298.12
	250 hr	S-4	1.8	219.29	3.3	328.27	3.5	257.49
		S-5	2.4	389.46	2.7	444.60	3.8	313.13
		S-6	1.8	278.78	2.3	356.68	3.3	312.82
	311 hr	S-7	3.0	227.81	3.0	204.10	6.25	231.32
		S-8	4.9	189.98	4.1	305.10	6.48	248.79
		S-9	3.2	201.74	3.5	X	6.7	237.11
Amorphous Selenium		S-1	-	X	-	520.35	-	523.84
		S-2	-	X	-	361.58	-	428.29
		S-3	-	X	-	374.06	-	548.56

TABLE 4

A Comparison of the Flexure Strength of Partially Crystallized Selenium Determined by 1-inch Span and ½-inch Span in Three-Point Bend Test

σ_f vs V_f		1-inch Span					
		MELT A		MELT B		MELT C	
		Volume Fraction V_f(%)	Flexure Strength σ_f(kg/cm^2)	Volume Fraction V_f(%)	Flexure Strength σ_f(kg/cm^2)	Volume Fraction V_f(%)	Flexure Strength σ_f(kg/cm^2)
100°C 45 min	S-1	X	X	3.77	327.05	7.14	246.11
	S-2	X	X	4.53	240.34	6.91	202.74
	S-3	X	X	3.34	189.66	7.98	X
				3.88	252.35	7.34	224.43
1 hr	S-4	X	X	13.81	168.01	15.06	343.07
	S-5	X	X	X	269.08	14.56	348.95
	S-6	X	X	16.63	329.75	16.85	233.85
				15.22	255.61	15.82	308.62
1½ hr	S-7	X	X	24.76	215.32	48.74	X
	S-8	X	X	X	253.95	X	X
	S-9	X	X	35.05	231.08	41.63	X
				29.91	233.45	45.19	X
82°C 4 hr	S-1	X	X	5.73	252.65	4.55	240.74
	S-2	X	X	7.73	411.37	8.28	238.19
	S-3	X	X	4.74	347.24	7.62	291.83
				6.08	337.09	6.82	256.92
6 hr	S-4	6.2	430.87	11.40	243.69	12.88	242.39
	S-5	7.15	193.47	6.01	333.45	14.61	267.20
	S-6	7.04	224.13	X	341.42	11.41	252.85
		6.80	282.82	8.07	306.19	12.97	254.14
8 hr	S-7	11.83	270.28	15.48	X	X	151.22
	S-8	13.39	242.03	13.19	301.59	16.84	326.15
	S-9	13.28	174.96	13.19	302.28	19.54	246.55
		12.83	229.09	13.40	301.94	18.19	241.30
62°C 200 hr	S-1	3.00	174.11	3.00	185.55	6.25	243.44
	S-2	4.09	162.46	4.01	X	X	281.02
	S-3	3.02	185.17	X	X	6.07	292.25
		3.07	173.91	3.05	185.55	6.48	272.24

TABLE 4 (Continued)

62°C 250 hr	S-4	1.08	320.12	3.03	375.39	3.05	366.21
	S-5	2.04	403.86	2.07	432.24	3.08	244.31
	S-6	1.08	321.23	2.03	301.91	3.03	312.28
		2.00	348.40	2.77	369.85	3.53	307.60
311 hr	S-7	X	X	1.02	390.86	2.02	439.50
	S-8	X	X	0.09	286.11	X	X
	S-9	X	X	0.08	332.37	2.15	236.84
				0.97	336.45	2.18	338.17
					½-inch Span		
100°C 45 min	S-1	8.25	244.31	3.77	360.10	7.14	278.24
	S-2	7.94	332.01	4.53	289.61	6.91	399.92
	S-3	8.88	295.62	3.34	267.75	7.98	242.07
		8.36	290.65	3.88	305.82	7.34	306.74
1 hr	S-4	26.31	210.03	13.81	297.70	15.06	245.64
	S-5	24.74	284.26	X	352.74	15.56	275.09
	S-6	19.03	185.23	16.63	306.01	16.85	X
		23.36	224.89	15.22	318.82	15.82	260.37
1½ hr	S-7	46.00	227.13	24.76	238.75	48.74	X
	S-8	X	X	X	193.22	X	232.26
	S-9	X	X	35.05	242.44	41.63	186.21
		46.00	227.13	29.91	233.88	45.19	209.24
82°C 4 hr	S-1	3.81	455.79	5.73	187.23	4.55	501.54
	S-2	3.59	351.53	7.76	386.04	8.28	407.35
	S-3	4.66	362.83	4.74	321.24	7.62	317.43
		4.02	390.05	6.08	298.17	6.82	408.77
6 hr	S-4	6.2	325.17	11.04	286.16	12.88	246.24
	S-5	7.15	315.91	6.01	360.60	14.61	292.72
	S-6	7.04	358.74		386.38	11.41	336.30
		6.80	333.27	8.07	344.38	12.97	291.75
8 hr	S-7	11.83	245.26	15.48	331.64	X	X
	S-8	13.39	298.35	13.19	350.66	16.84	329.33
	S-9	13.28	190.49	13.19	199.11	19.54	281.57
		12.83	244.70	13.95	293.80	18.19	305.45
62°C 200 hr	S-1	3.0	254.66	3.00	213.38	6.25	225.25
	S-2	4.09	203.78	4.01	305.10	X	232.67
	S-3	3.02	209.89	X	X	6.07	181.97
		3.07	222.78	3.5	259.24	6.48	213.30

TABLE 4 (Continued)

62°C 250 hr	S-4	1.08	283.10	3.03	304.72	3.05	203.13
	S-5	2.04	382.28	2.07	450.79	3.08	347.54
	S-6	1.08	257.56	2.03	384.07	3.03	313.08
		2.00	307.65	2.77	379.86	3.53	287.92
311 hr	S-7	1.04	X	1.02	422.82	2.02	438.17
	S-8	X	292.33	0.09	370.34	X	380.58
	S-9	1.04	388.36	0.08	350.58	2.15	328.76
		1.04	340.34	0.97	381.25	2.17	382.50

TABLE 5

Flexure Strength and Elastic Modulus of Partially Crystallized Selenium Versus Volume Fraction of Crystallites for Constant Size of Crystallites

σ_f vs V_f			CONSTANT d_s			
				Flexure Strength σ_f(kg/cm^2)	Volume Fraction V_f(%)	Elastic Modulus E(10^5 kg/cm^2)
d_s = 12.75 μm						
MELT A	100°C	45 min	S-2	332.01	7.94	5.048
	62°C	200 hr	S-1	X	1.04	X
			S-2	292.32	1.04	3.076
			S-3	388.36	1.04	3.156
MELT B	100°C	45 min	S-1	360.10	3.77	3.357
			S-2	289.61	4.53	2.445
			S-3	267.75	3.34	2.849
MELT C	62°C	200 hr	S-1	438.17	2.02	2.764
			S-3	328.76	2.15	1.737
d_s = 15.87 μm						
MELT A	100°C	45 min	S-1	244.31	8.25	X
	62°C	250 hr	S-4	283.10	1.80	1.950
			S-5	382.10	2.04	3.148
			S-6	257.56	1.08	2.695
MELT C	100°C	45 min	S-1	278.24	7.14	5.8307
			S-2	399.92	6.91	5.558
			S-3	242.07	7.98	4.074
	62°C	250 hr	S-4	203.13	3.05	4.827
			S-5	347.54	3.08	4.075
			S-6	313.08	3.03	3.880
d_s = 19.05 μm						
MELT A	100°C	45 min	S-3	295.62	8.88	6.117
	82°C	4 hr	S-1	455.79	3.81	1.867
			S-2	351.53	3.59	4.176
			S-3	362.83	4.66	2.676

TABLE 5 (Continued)

MELT B	100°C	1 hr	S-6	306.01	16.63	2.373
	82°C	4 hr	S-1	187.23	5.73	2.091
			S-2	386.04	7.76	1.574
			S-3	321.24	4.74	3.627
MELT C	82°C	4 hr	S-1	501.54	4.55	3.034
			S-2	407.35	8.28	3.729
			S-3	317.43	7.62	3.551
d_s = 22.22 μm						
MELT A	82°C	6 hr	S-4	325.17	6.2	2.126
			S-5	315.91	7.15	2.765
			S-6	358.74	7.04	3.367
MELT B	100°C	1 hr	S-4	297.70	13.81	2.373
			S-5	352.74	15.20	3.909
MELT C	100°C	1 hr	S-4	254.64	15.06	4.567
			S-5	275.09	15.06	2.3036
	82°C	6 hr	S-4	246.24	12.88	3.218
			S-5	292.72	14.61	4.472
			S-6	336.30	11.41	3.434
d_s = 25.14 μm						
MELT A	100°C	1 hr	S-5	284.26	24.74	4.301
	82°C	8 hr	S-7	245.26	11.83	2.228
			S-8	298.35	13.39	2.862
			S-9	190.49	13.28	2.749
	62°C	311 hr	S-7	254.66	3.00	3.598
			S-8	203.78	4.9	3.513
			S-9	209.89	3.2	3.636
MELT B	82°C	6 hr	S-4	286.16	11.4	4.799
			S-5	360.60	6.01	3.642
			S-6	386.38	X	4.206
	62°C	311 hr	S-7	213.38	3.0	1.489
			S-8	305.10	4.1	2.310

TABLE 5 (Continued)

d_s = 31.75 μm						
MELT A	100°C	1 hr	S-4	210.03	26.31	3.196
			S-6	180.37	19.03	2.916
MELT B	82°C	8 hr	S-7	331.64	15.48	4.759
			S-8	350.66	13.19	3.80
			S-9	199.11	13.19	2.795
d_s = 50.8 μm						
MELT A	100°C	1½ hr	S-7	227.13	46.00	4.507
MELT B	100°C	1½ hr	S-8	193.22	24.76	5.568
			S-9	242.44	35.05	3.321
MELT C	100°C	1½ hr	S-8	232.26	48.74	4.847
			S-9	186.21	41.63	4.371

TABLE 6

Flexure Strength and Elastic Modulus of Partially Crystallized Selenium Versus Size of Crystallites for Constant Volume Fraction of Crystallites of Selenium

σ_f vs d_s CONSTANT V_s

				Flexure Strength σ_f (kg/cm^2)	Diameter of Spherulite d_s (μm)	Elastic Modulus E(10^5 kg/cm^2)	Flaw Size C(μm)	Ratio C /d_s
V_s = 2.09%								
MELT A	62°C	200 hr	S-1	X	12.75	X	X	X
			S-2	292.33	12.75	3.139	37.310	2.93
			S-3	388.36	12.75	3.221	21.685	1.70
	62°C	250 hr	S-4	283.10	15.80	1.99	42.035	2.66
			S-5	382.28	15.80	3.213	21.506	1.36
			S-6	257.56	15.80	2.750	35.940	2.27
MELT B	62°C	250 hr	S-4	304.72	15.80	3.375	31.826	2.01
			S-5	450.79	15.80	3.281	16.855	1.06
			S-6	384.07	15.80	3.278	26.166	1.65
MELT C	62°C	200 hr	S-7	438.17	12.75	2.821	14.891	1.17
			S-8	380.58	12.75	2.899	20.329	1.57
			S-9	328.76	12.75	1.773	20.256	1.59
V_s = 3.73%								
MELT A	62°C	311 hr	S-1	254.66	25.40	3.671	71.890	2.83
			S-2	203.78	25.40	3.585	100.890	3.97
			S-3	209.87	25.40	3.710	92.600	3.65
MELT A	82°C	4 hr	S-1	455.79	19.05	1.905	9.314	.49
			S-2	351.53	19.05	4.262	68.395	3.59
			S-3	362.83	19.05	2.731	21.069	1.11
MELT B	62°C	311 hr	S-1	213.38	25.40	X	37.047	1.46
			S-2	305.10	25.40	1.519	25.722	1.01
			S-3		25.40	2.358	X	X

TABLE 6 (Continued)

MELT B	100°C	45 hr	S-1	360.10	12.75	3.426	28.555	2.24
			S-2	289.61	12.75	2.494	33.955	2.66
			S-3	267.75	12.75	2.907	50.545	1.71
MELT C	62°C	250 hr	S-4	203.13	15.80	4.925	75.078	4.78
			S-5	347.54	15.80	4.158	43.094	2.73
			S-6	313.08	15.80	3.959	41.094	2.60
V_s = 6.55%								
MELT A	82°C	6 hr	S-4	325.17	22.22	2.169	16.964	.76
			S-5	315.91	22.22	2.821	37.872	1.70
			S-6	358.74	22.22	3.436	35.424	1.61
MELT B	82°C	4 hr	S-1	187.23	19.05	2.134	44.806	2.35
			S-2	386.04	19.05	1.606	10.82	.57
			S-3	321.24	19.05	3.701	34.537	1.81
MELT C	82°C	4 hr	S-1	501.54	19.05	3.096	22.829	1.20
			S-2	407.35	19.05	3.805	31.376	1.65
			S-3	317.43	19.05	3.623	38.569	2.02
MELT C	62°C	311 hr	S-1	225.25	25.4	5.440	103.289	4.07
			S-2	232.67	25.4	3.576	58.698	2.31
			S-3	181.97	25.4	3.466	62.606	2.46
V_s = 8.13%								
MELT A	100°C	45 hr	S-1	244.31	15.87	X	X	X
			S-2	332.01	12.75	5.151	47.461	3.72
			S-3	295.62	19.05	6.242	72.552	3.81
MELT B	82°C	6 hr	S-4	286.16	25.4	4.897	67.234	2.65
			S-5	360.60	25.4	3.716	31.423	1.24
			S-6	386.38	25.4	4.292	32.917	1.30
MELT C	100°C	45 hr	S-1	278.24	15.87	5.949	84.441	5.32
			S-2	399.92	15.87	5.672	51.578	3.25
			S-3	242.07	15.87	4.157	72.061	4.54

TABLE 6 (Continued)

V_s = 14.16%

MELT A	82°C	8 hr	S-7	245.26	25.4	2.274	35.907	1.41
			S-8	298.35	25.4	2.920	37.954	1.49
			S-9	190.49	25.4	2.806	82.982	3.27
MELT B	100°C	1 hr	S-4	297.70	22.22	2.422	37.979	1.71
			S-5	352.74	22.22	3.988	38.390	1.73
			S-6	306.01	22.22	3.505	35.232	1.85
MELT B	82°C	8 hr	S-7	331.64	31.75	4.857	44.849	1.41
			S-8	350.66	31.75	3.877	35.240	1.11
			S-9	199.11	31.75	2.852	53.133	1.67
MELT C	100°C	1 hr	S-4	245.67	22.22	4.660	61.193	2.75
			S-5	275.09	22.22	2.351	26.580	1.20
			S-6	X	22.22	2.238	84.402	3.80
MELT C	82°C	6 hr	S-4	246.24	22.22	3.283	55.587	2.50
			S-5	292.72	22.22	4.563	59.143	2.66
			S-6	336.30	22.22	3.503	37.402	1.68

TABLE 7

Elastic Modulus of Amorphous and Partially Crystallized Selenium

			MELT A MODULUS OF ELASTICITY (10^5 kg/cm^2)	MELT B MODULUS OF ELASTICITY (10^5 kg/cm^2)	MELT C MODULUS OF ELASTICITY (10^5 kg/cm^2)
100°C	45 min	S-1	X	3.4257	5.9497
		S-2	5.1515	2.4945	5.6716
		S-3	6.242	2.9073	4.1567
	1 hr	S-4	3.2613	2.4216	4.6603
		S-5	4.3889	3.9884	2.3506
		S-6	2.9753	3.5054	3.2682
	1½ hr	S-7	4.5987	3.8702	X
		S-8	X	5.6817	4.9459
		S-9	X	3.3885	4.4604
82°C	4 hr	S-1	1.9047	2.1338	3.0961
		S-2	4.2615	1.6064	3.8047
		S-3	2.7309	3.7007	3.6235
	6 hr	S-4	2.1691	4.8968	3.2836
		S-5	2.8215	3.7165	4.5632
		S-6	3.4362	4.2921	3.5026
	8 hr	S-7	2.2737	4.8566	1.7228
		S-8	2.9204	3.8776	4.0853
		S-9	2.8055	2.8525	4.1530
62°C	200 hr	S-1	X	3.2149	2.8209
		S-2	3.1386	4.2930	2.8994
		S-3	3.2205	3.0685	1.7773
	250 hr	S-4	1.9901	3.3747	4.9255
		S-5	3.2126	3.2808	4.1579
		S-6	2.7502	3.2780	3.9589
	311 hr	S-7	3.6712	1.5191	5.4403
		S-8	3.5852	2.3576	3.5764
		S-9	3.7099	X	3.46559
AMORPHOUS SELENIUM			0.8370	0.9000	0.9890

TABLE 8

Fracture Surface Energy
for Amorphous and Partially Crystallized Selenium

HEAT TREATMENT	FLEXURE STRENGTH (kg/cm^2)	MODULUS OF ELASTICITY (10^5 kg/cm^2)	FRACTURE SURFACE ENERGY (ergs/cm^2)
AMORPHOUS SELENIUM			
MELT C			
S-1	77.1312	4.0728	1.5902
S-2	78.7537	2.8977	1.3593
MELT A			
S-3	78.4311	4.2639	1.9370
MELT A			
100°C 45 min			
S-2	78.3416	6.0414	1.2903
S-3	106.5953	7.28611	1.2450
100°C 1½ hr			
S-6	131.2962	8.2533	1.8191
S-7	77.0220	6.1389	1.3676
S-8	78.5270	5.0721	1.7648

Fig. 14. Reproducibility of surface microstructure of specimens heat treated at 100°C.

100°C 45 min.

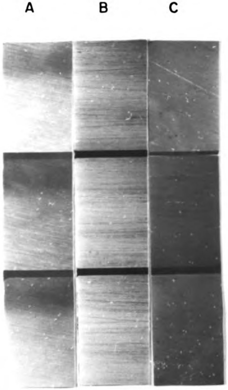

100°C 1 HR.

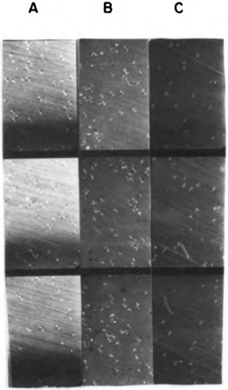

100°C 1½ HR

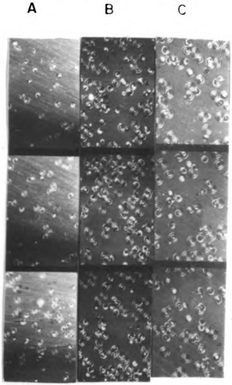

Fig. 15. Reproducibility of surface microstructure of specimens heat treated at 82° C.

82°C 4 HRS.

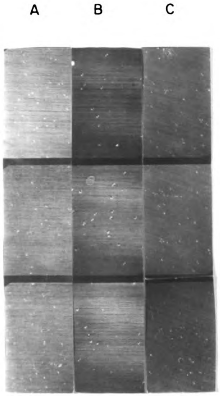

82° C 6 HRS.

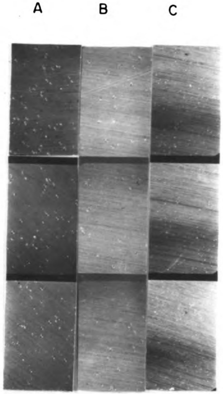

82°C 8 HRS.

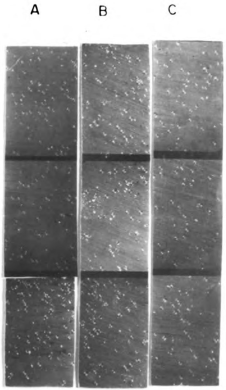

Fig. 16. Microstructures of specimens heat treated at 100°C. Polarized light micrographs of partially crystallized selenium obtained by: (A) Heat treating at 100°C for 45 min
(B) Heat treating at 100°C for 1 hr , and
(C) Heat treating at 100°C for 1 1/2 hr.

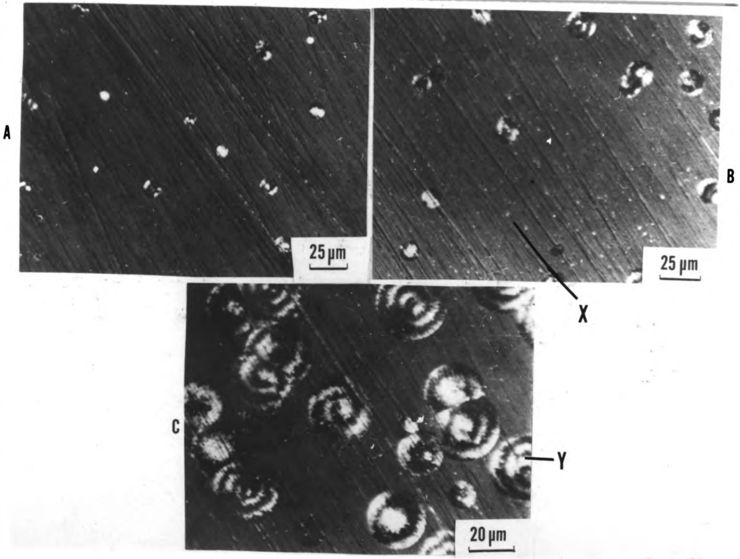
A
25 µm
B
25 µm
X
C
Y
20 µm

Fig. 17. Microstructures of specimens heat treated at 82°C. Polarized light micrographs of partially crystallized selenium obtained by: (A) Heat treating at 82°C for 4 hr ,
(B) Heat treating at 82°C for 6 hr , and
(C) Heat treating at 82°C for 8 hr.

A

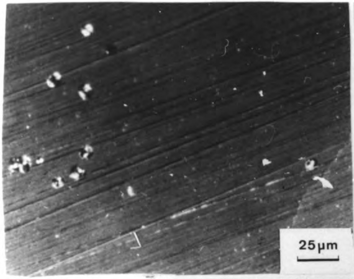

B

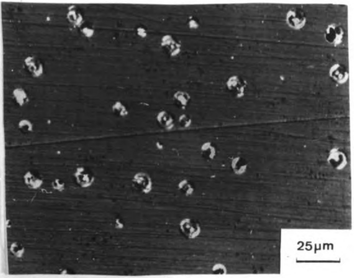

C

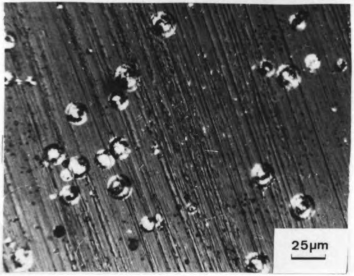

Fig. 18. Microstructures of specimens heat treated at 62°C. Polarized light micrographs of partially crystallized selenium obtained by:
(A) Heat treating at 62°C for 200 hr ,
(B) Heat treating at 62°C for 250 hr , and
(C) Heat treating at 62°C for 311 hr.

A

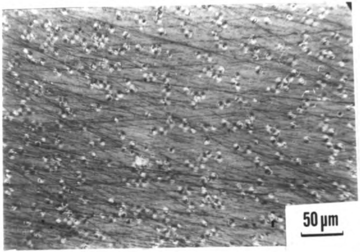

B

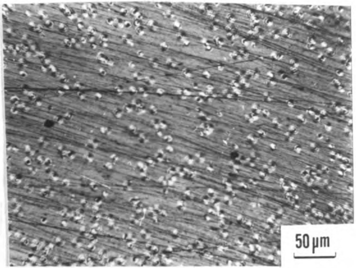

C

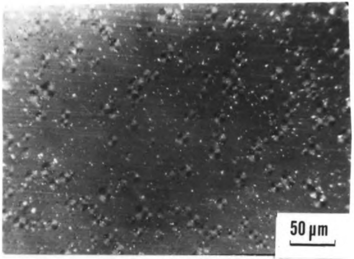

Fig. 19. Plot of flexure strength as a function of volume fraction for melts A, B and C.

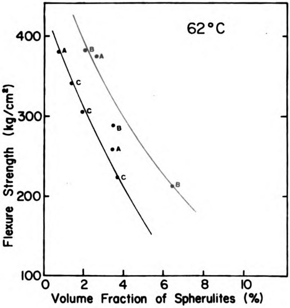
62°C
Flexure Strength (kg/cm²)
400
300
200
100
0
2
4
6
8
10
Volume Fraction of Spherulites (%)
A
B
A
C
C
B
A
C
B

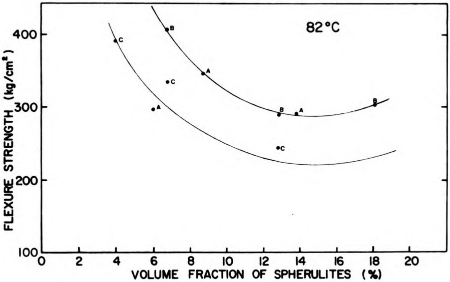
82°C
FLEXURE STRENGTH (kg/cm²)
400
300
200
100
0
2
4
6
8
10
12
14
16
18
20
VOLUME FRACTION OF SPHERULITES (%)
B
C
A
C
A
B
A
B
C

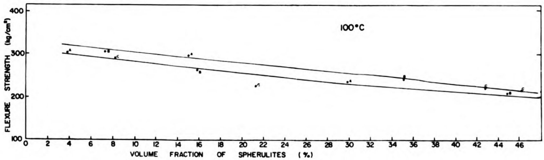
100°C
FLEXURE STRENGTH (kg/cm²)
400
300
200
100
0
2
4
6
8
10
12
14
16
18
20
22
24
26
28
30
32
34
36
38
40
42
44
46
VOLUME FRACTION OF SPHERULITES (%)

Fig. 20. Plot of flexure strength as a function of volume fraction for specimens heat treated at 62°C.

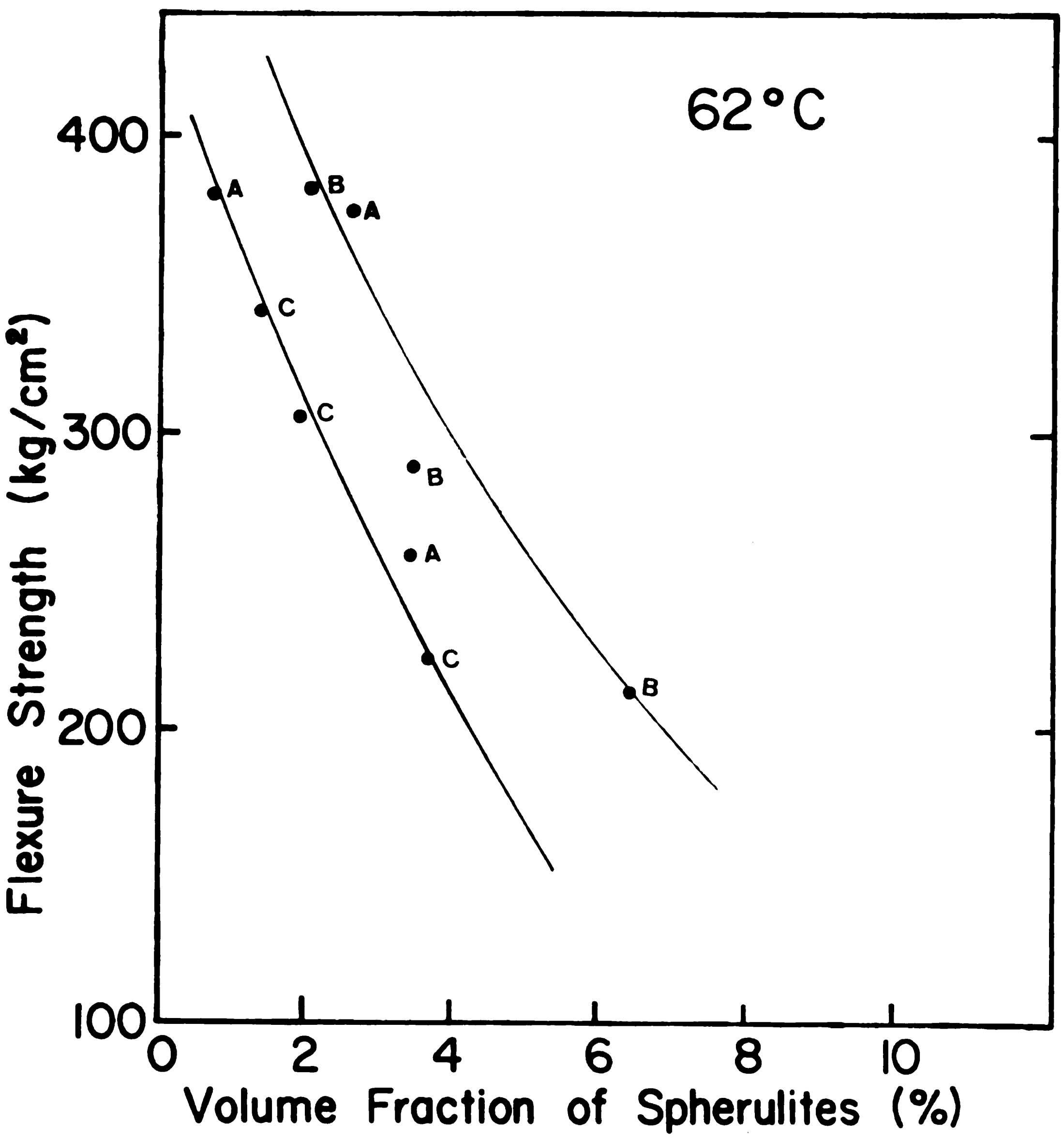
62°C
Flexure Strength (kg/cm²)
Volume Fraction of Spherulites (%)
100
200
300
400
0
2
4
6
8
10
A
B
A
C
C
B
A
C
B

Fig. 21. Plot of flexure strength as a function of volume fraction for specimens heat treated at 82^{o}C.

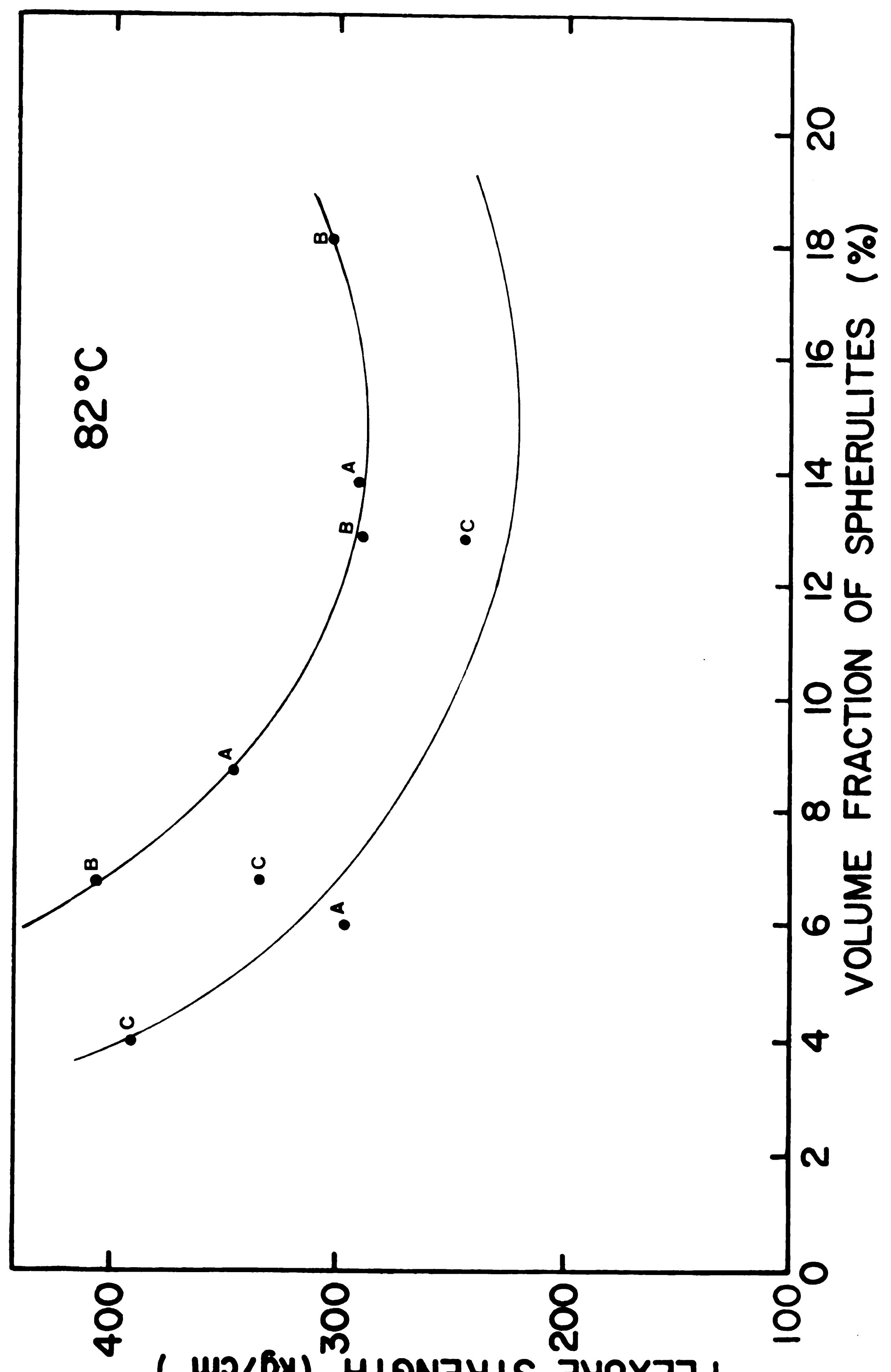
82°C
FLEXURE STRENGTH (kg/cm²)
100
200
300
400
VOLUME FRACTION OF SPHERULITES (%)
0
2
4
6
8
10
12
14
16
18
20
A
B
C

Fig. 22. Plot of flexure strength as a function of volume fraction for specimens heat treated at 100°C.

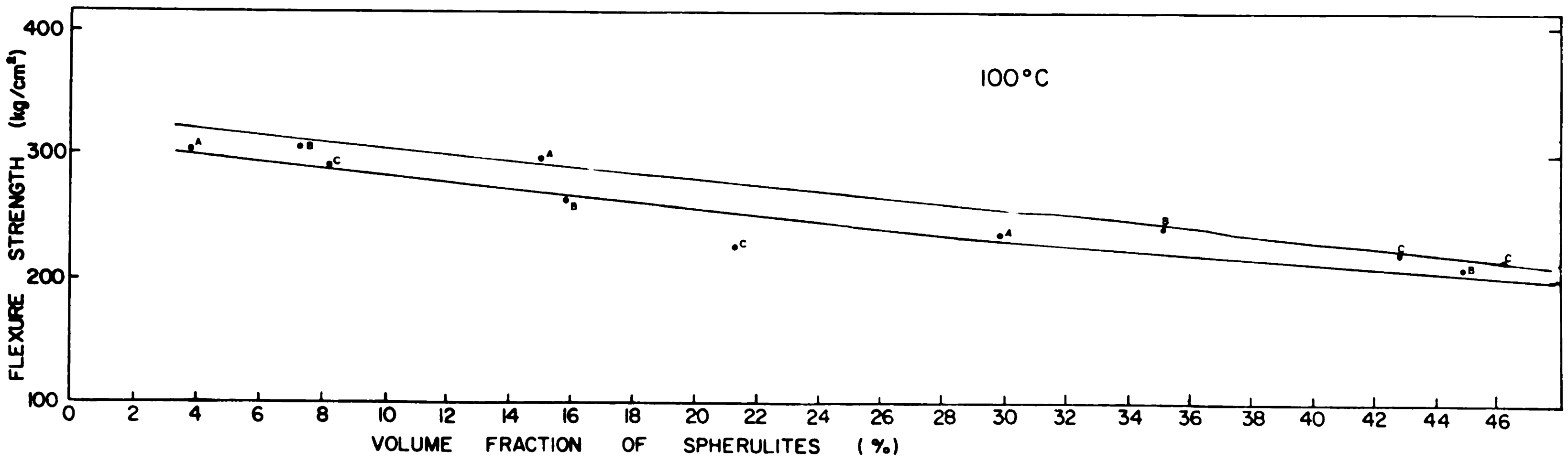
100°C
FLEXURE STRENGTH (kg/cm²)
400
300
200
100
VOLUME FRACTION OF SPHERULITES (%)
0
2
4
6
8
10
12
14
16
18
20
22
24
26
28
30
32
34
36
38
40
42
44
46
A
B
C

Fig. 23. Plot of flexure strength as a function of volume fraction for constant-size crystallites (d_s = 12.75 and 15.78 μm).

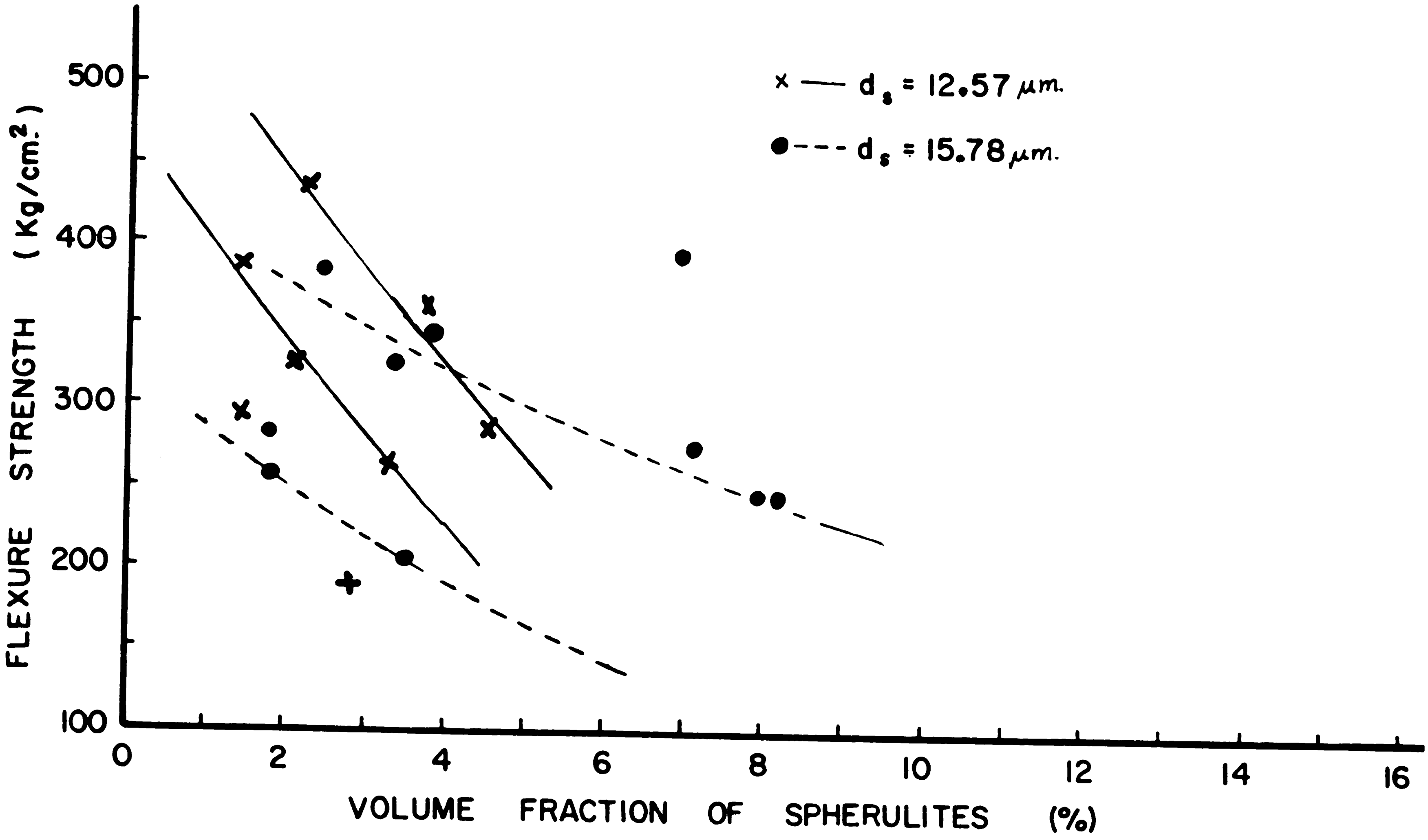

× —— d_s = 12.57 μm.
● - - - d_s = 15.78 μm.
FLEXURE STRENGTH (Kg/cm.²)
500
400
300
200
100
0
2
4
6
8
10
12
14
16
VOLUME FRACTION OF SPHERULITES (%)

Fig. 24. Plot of flexure strength as a function of volume fraction for constant-size crystallites (d_s = 19.06 and 22.22 μm).

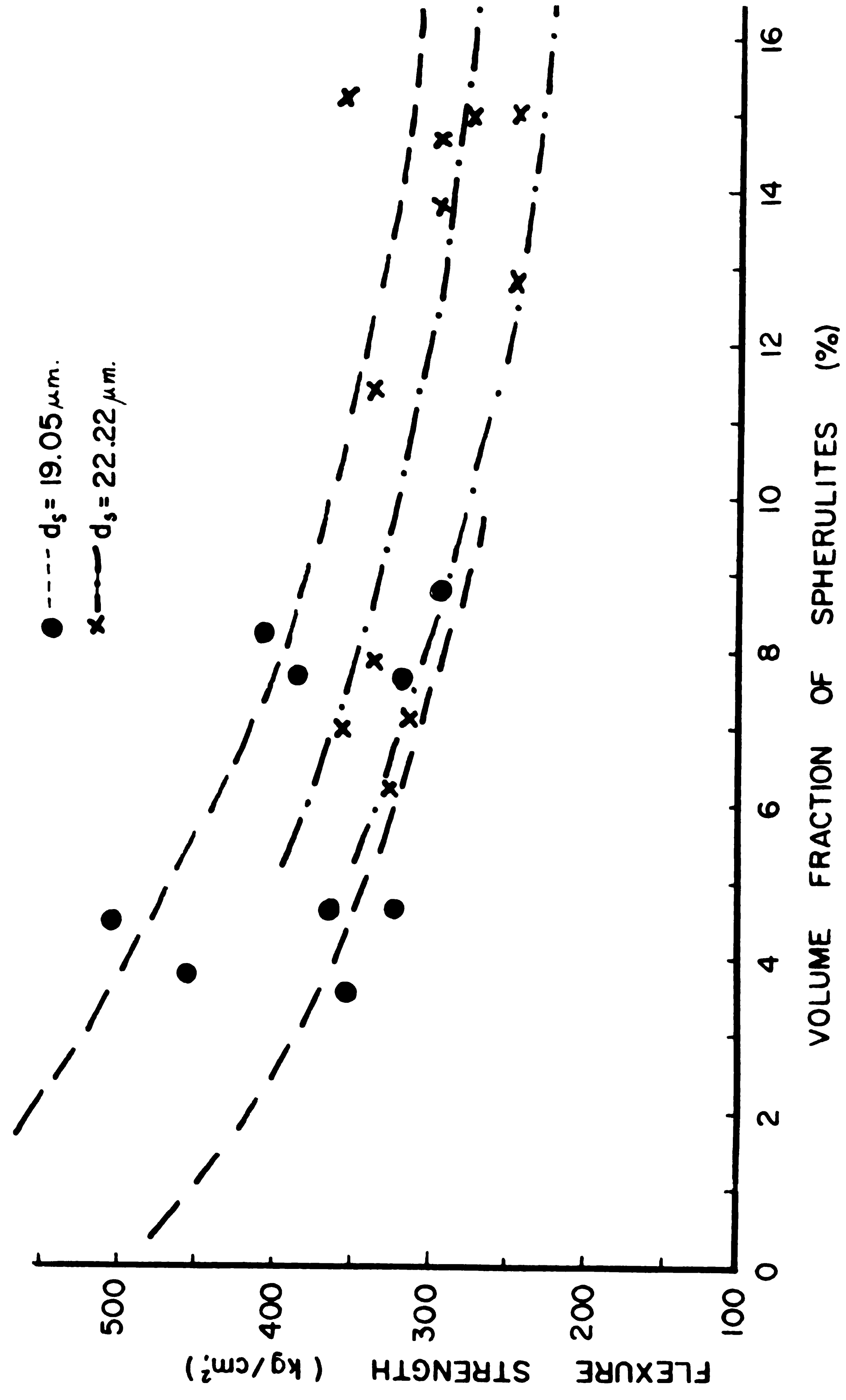
FLEXURE STRENGTH (kg/cm^2)
100
200
300
400
500
VOLUME FRACTION OF SPHERULITES (%)
0
2
4
6
8
10
12
14
16
● ---- d_s = 19.05 μm.
x—·—·— d_s = 22.22 μm.

Fig. 25. Plot of flexure strength as a function of volume fraction for constant-size crystallites (d_s = 25.14 and 50.80 μm).

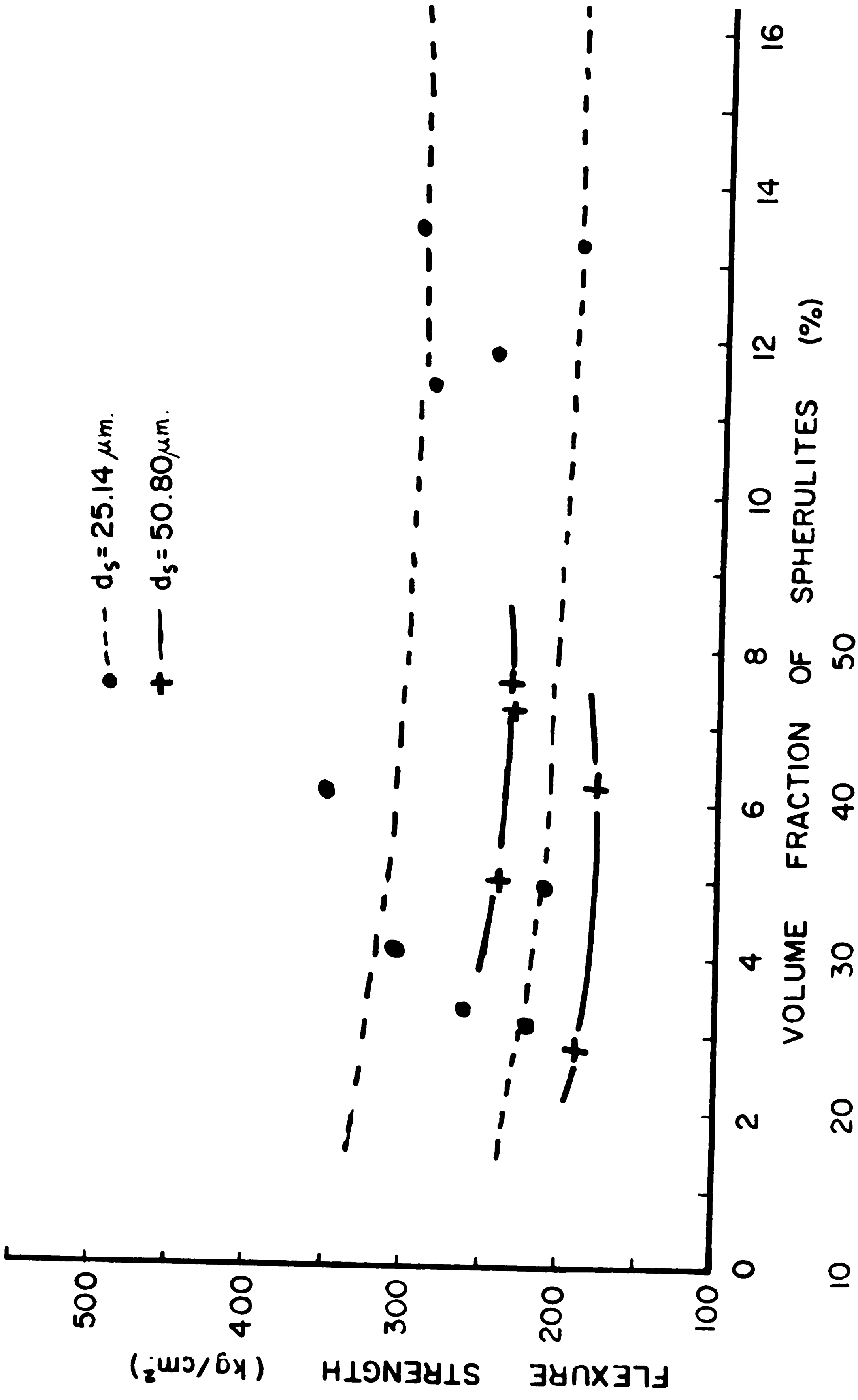

FLEXURE STRENGTH (kg/cm²)
100
200
300
400
500
0
2
4
6
8
10
12
14
16
10
20
30
40
50
VOLUME FRACTION OF SPHERULITES (%)
● - - - d_s = 25.14 μm.
+ —— d_s = 50.80 μm.

Fig. 26. Plot of flexure strength as a function of size of crystallites for constant volume fraction of crystallites (V_s = 2.09 and 3.73 %).

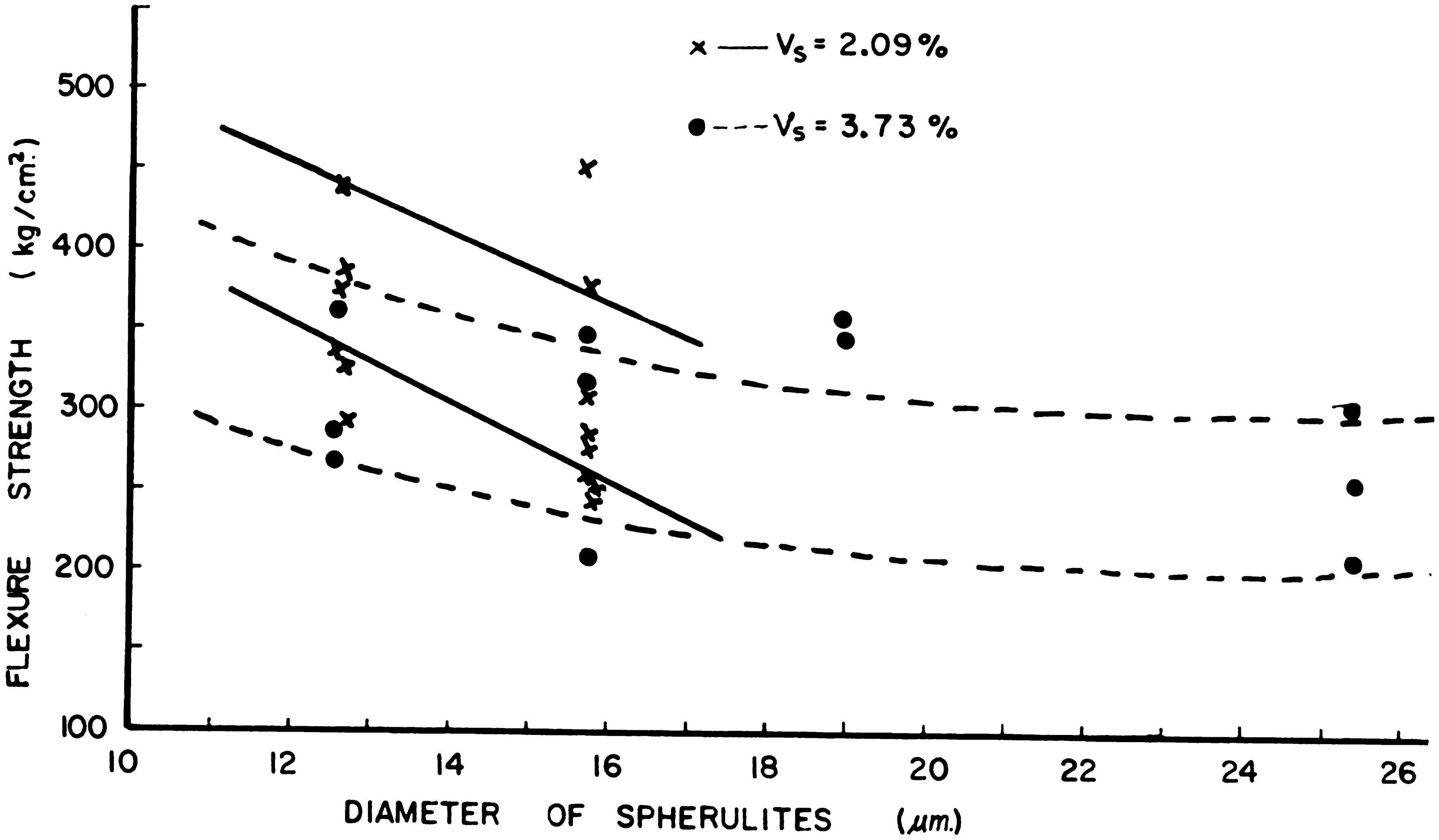
x —— V_s = 2.09%
● - - - V_s = 3.73%
FLEXURE STRENGTH (kg/cm²)
500
400
300
200
100
10
12
14
16
18
20
22
24
26
DIAMETER OF SPHERULITES (μm.)

Fig. 27. Plot of flexure strength as a function of size of crystallites for constant volume fraction of crystallites (V_s = 6.55 and 8.15 %).

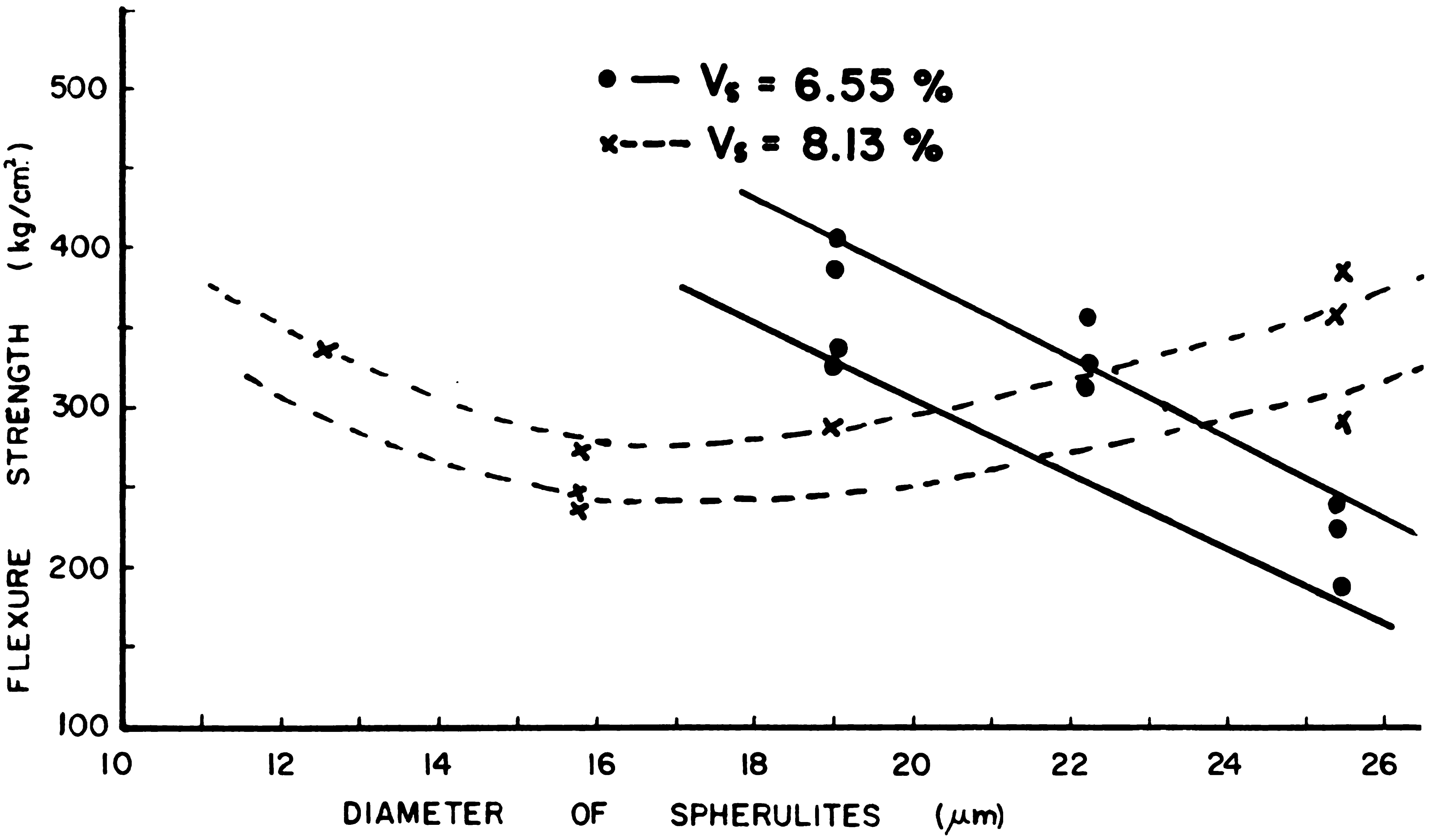
● —— V_s = 6.55 %
x- - - - V_s = 8.13 %
FLEXURE STRENGTH (kg/cm².)
100
200
300
400
500
10
12
14
16
18
20
22
24
26
DIAMETER OF SPHERULITES (μm)

Fig. 28. Plot of flexure strength as a function of size of crystallites for constant volume fraction of crystallites (V_s = 14.16 %).

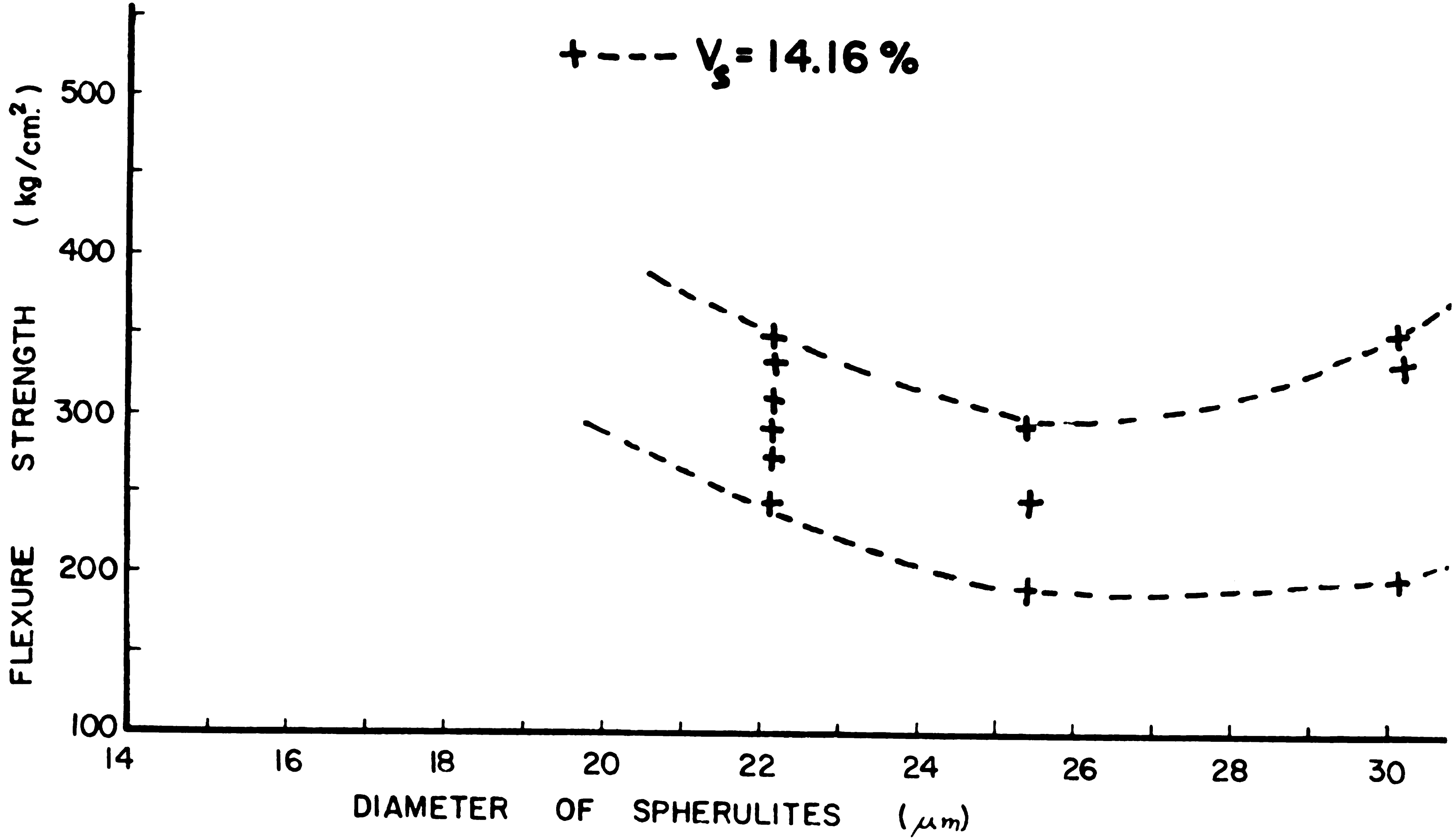
+ --- V_s = 14.16 %
FLEXURE STRENGTH (kg/cm.^{2})
500
400
300
200
100
14
16
18
20
22
24
26
28
30
DIAMETER OF SPHERULITES (μm)

Fig. 29. Plot of elastic modulus of partially crystallized selenium as a function of volume fraction of crystallites for constant-size crystallites (d_s = 12.75, 15.78, 19.05, 22.22, 25.14 and 50.80 μm).

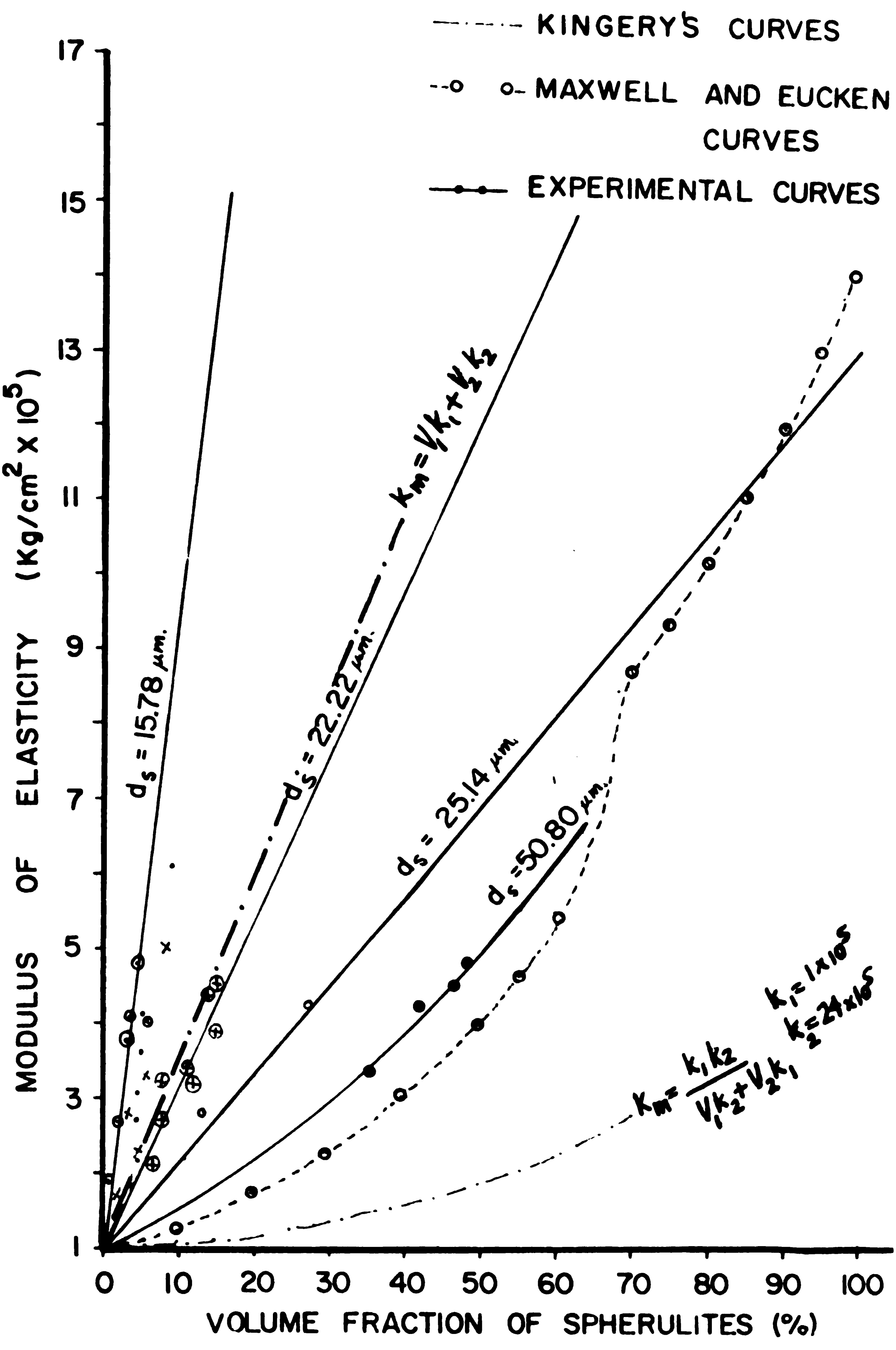
KINGERY'S CURVES
MAXWELL AND EUCKEN CURVES
EXPERIMENTAL CURVES
MODULUS OF ELASTICITY (Kg/cm^2 x 10^5)
17
15
13
11
9
7
5
3
1
VOLUME FRACTION OF SPHERULITES (%)
0
10
20
30
40
50
60
70
80
90
100
$d_s = 15.78\ \mu m.$
$d_s = 22.22\ \mu m.$
$K_m = V_1k_1 + V_2k_2$
$d_s = 25.14\ \mu m$
$d_s = 50.80\ \mu m.$
$K_m = \frac{k_1k_2}{V_1k_2 + V_2k_1}$
$k_1 = 1 \times 10^5$
$k_2 = 24 \times 10^5$

Fig. 30. SEM fractographs of amorphous selenium.
(A) Total field of fracture (30x).
(B) The fracture propagates with no preferred direction shown at location X.
(C) The fracture consists of coarse and mirror regions shown at location Y.

A

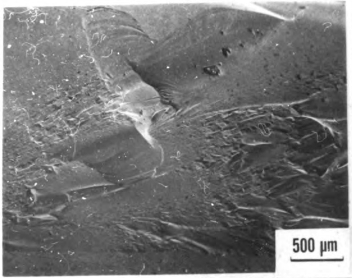

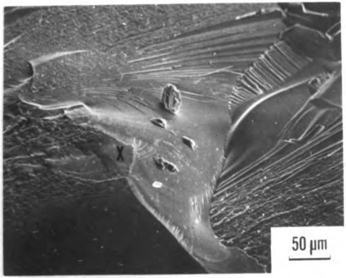

B

C

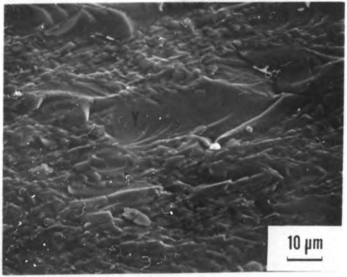

Fig. 31. SEM fractographs of partially crystallized selenium obtained by heat treating at 62^{o}C for 200 hr
(A) Total field of fracture (30x).
(B) Origin of fracture (200x).
(C) Spherulites in hackle region of fracture (500x).

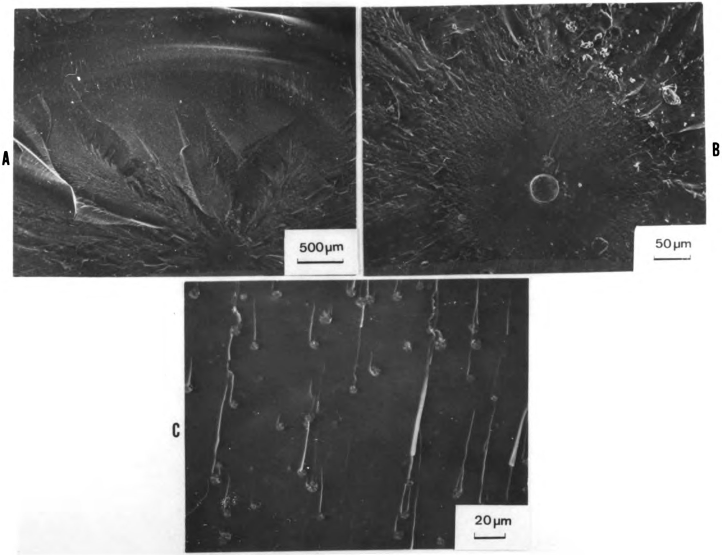
A
500µm
B
50µm
C
20µm

Fig. 32. SEM fractographs of partially crystallized selenium obtained by heat treating at 62°C for 250 hr
(A) Total field of fracture (30x).
(B) Origin of fracture (200x).
(C) Spherulites in hackle region of fracture (500x).

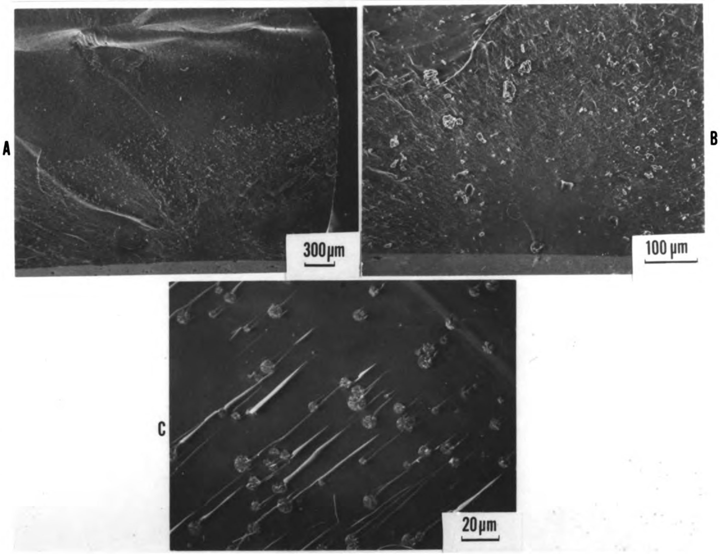
A
300µm
B
100 µm
C
20µm

Fig. 33. SEM fractographs of partially crystallized selenium obtained by heat treating at 62°C for 311 hr
(A) Total field of fracture (50x).
(B) Origin of fracture (500x).
(C) A spherulite in hackle region of fracture (2000x).

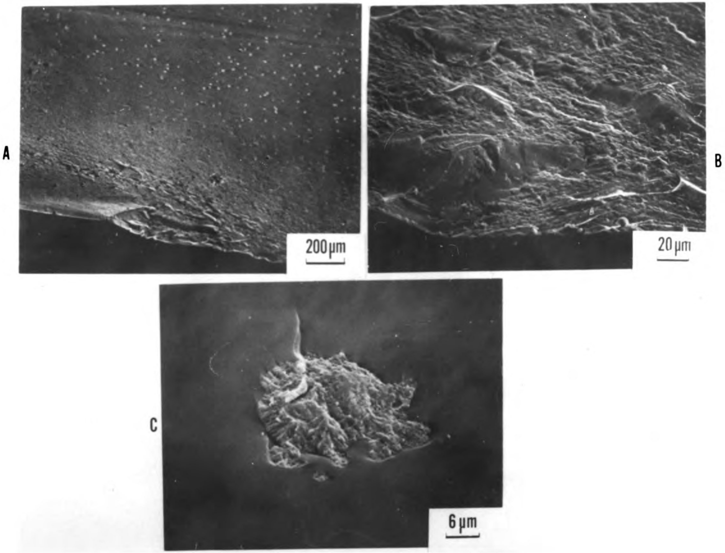
A
200 µm
B
20 µm
C
6 µm

Fig. 34. SEM fractographs of partially crystallized selenium obtained by heat treating at $100^{\circ}C$ for 45 min
(A) Total field of fracture (50x).
(B) Origin of fracture (1000x).
(C) A spherulite in the mirror region (1000x).
(D) A spherulite in the coarse region (1000x).

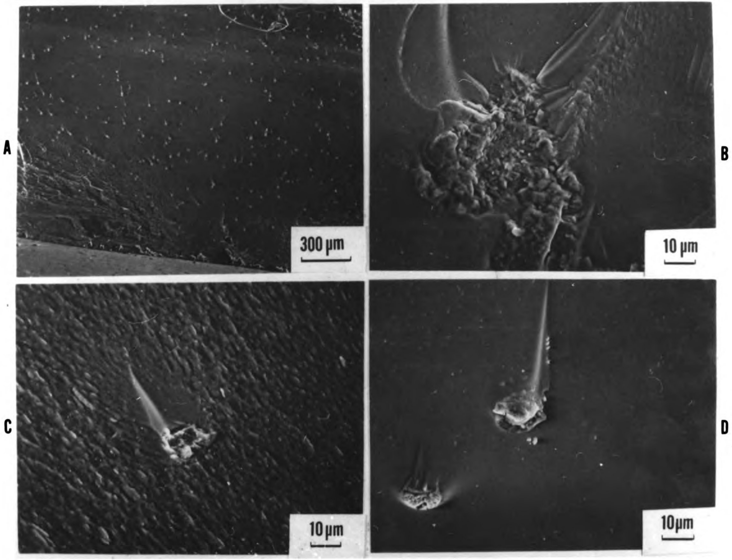
A
300 µm
B
10 µm
C
10µm
D
10µm

Fig. 35. SEM fractographs of partially crystallized selenium obtained by heat treating at 100°C for 1 hr
(A) Total field of fracture (50x).
(B) Origin of fracture (1000x).
(C) A spherulite in the mirror region (1000x).
(D) A spherulite in the coarse region (1000x).

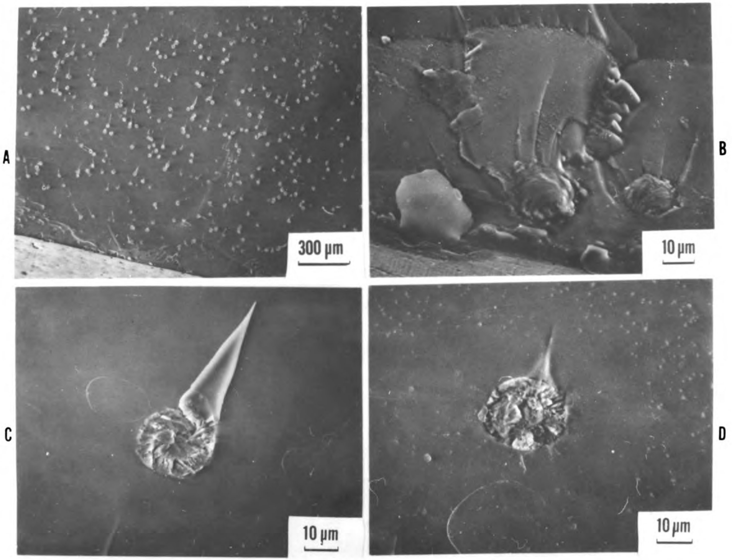
A
300 μm
B
10 μm
C
10 μm
D
10 μm

Fig. 36. SEM fractographs of partially crystallized selenium obtained by heat treating at 100°C for 1½ hr
(A) Total field of fracture (30x).
(B) Origin of fracture (500x).
(C) Spherulites in the mirror and coarse region (500x).
(D) Spherulites in the hackle region (500x).

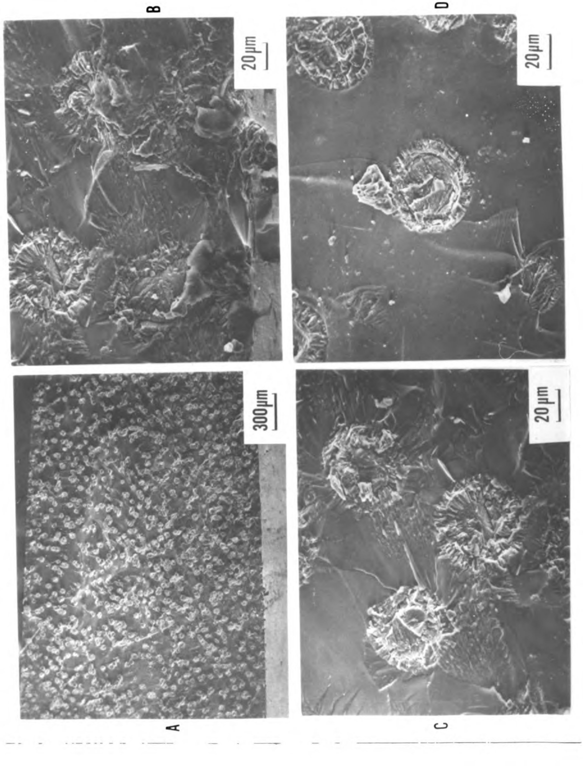
A
300µm
B
20µm
C
20µm
D
20µm

Fig. 37. SEM fractographs of partially crystallized selenium obtained by heat treating at 82°C for 4 hr
(A) Total field of fracture (50x).
(B) Origin of fracture (500x).
(C) A spherulite in coarse region of fracture (1000x).
(D) Spherulites in hackle region of fracture (500x).

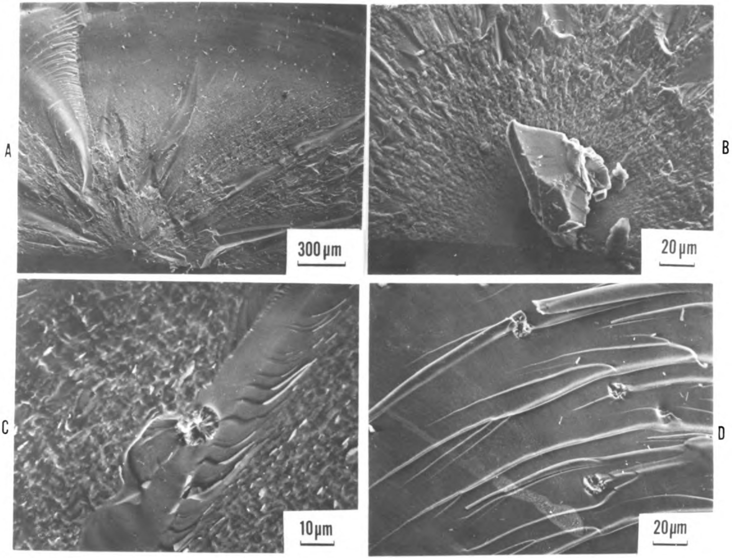
A
300 µm
B
20 µm
C
10µm
D
20µm

Fig. 38. SEM fractographs of partially crystallized selenium obtained by heat treating at 82°C for 6 hr
(A) Total field of fracture (50x).
(B) Origin of fracture (2000x).
(C) Spherulites in coarse region (1000x).
(D) Spherulites in hackle region (1000x).

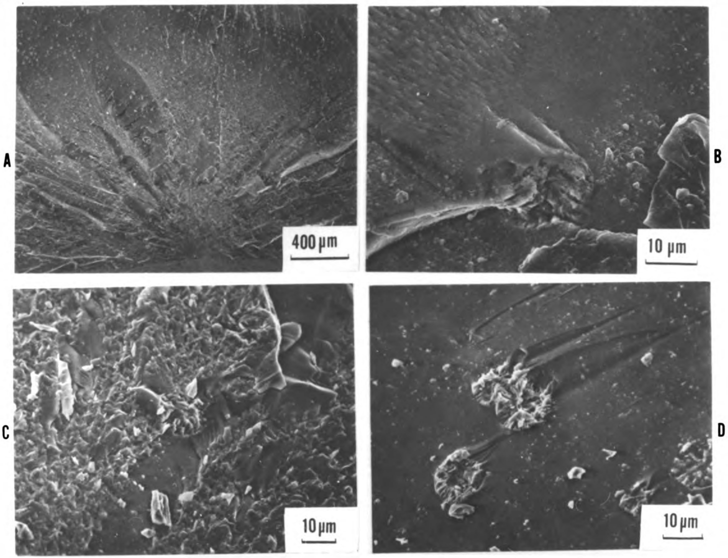
A
400 µm
B
10 µm
C
10µm
D
10µm

Fig. 39. SEM fractographs of partially crystallized selenium obtained by heat treating at $82^{o}C$ for 8 hr
(A) Total field of fracture (30x).
(B) Origin of fracture (500x).
(C) Spherulites in coarse region of fracture (500x).
(D) Spherulites in hackle region of fracture (500x).

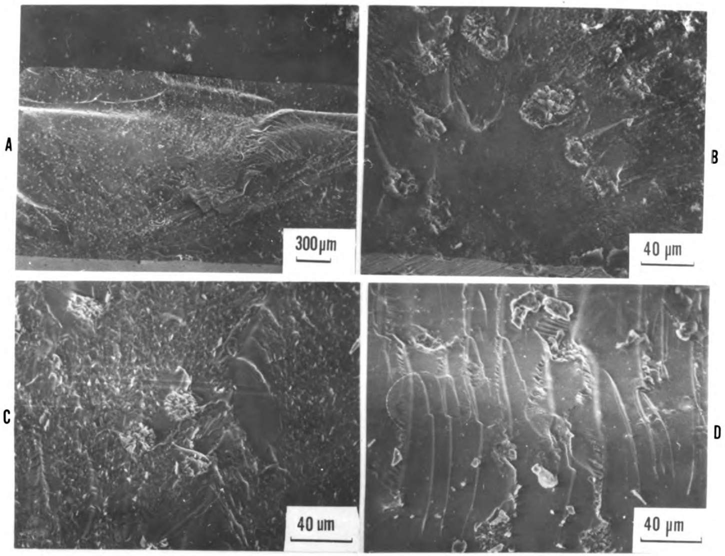
A
300µm
B
40 µm
C
40 um
D
40 µm

Fig. 40. SEM fractograph showing the details of fracture surface in and around a spherulite (2000x).


10 µm

Fig. 41. SEM fractographs showing

(A) A spherulite in the mirror region of fracture for specimen heat treated at 82°C for 6 hr (2000x).

(B) Spherulites present at the origin of fracture for specimen heat treated at 82°C for 6 hr (2000x).

A

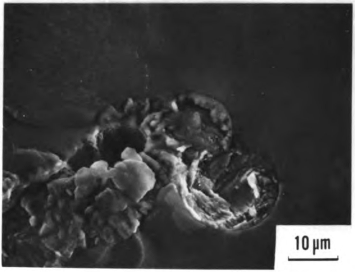

B

Fig. 42. SEM fractographs showing
(A) The origin of fracture for specimen heat treated at 82^oC for 8 hr (500x).
(B) The hackle region of fracture for specimen heat treated at 82^oC for 8 hr (1000x).

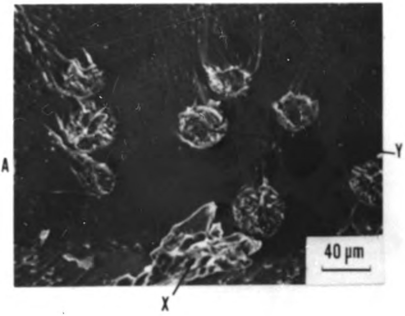
A
Y
40 µm
X

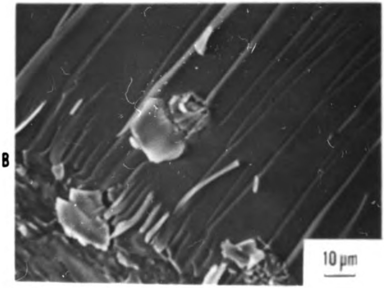
B
10 µm

Fig. 43. SEM fractographs showing
(A) A spherulite in the mirror region of fracture for specimen heat treated at 82°C for 8 hr (1500x).
(B) A spherulite in the coarse region of fracture for specimen heat treated at 82°C for 8 hr (1500x).
(C) Two spherulites in the mirror region of fracture for specimen heat treated at 82°C for 8 hr (1500x).

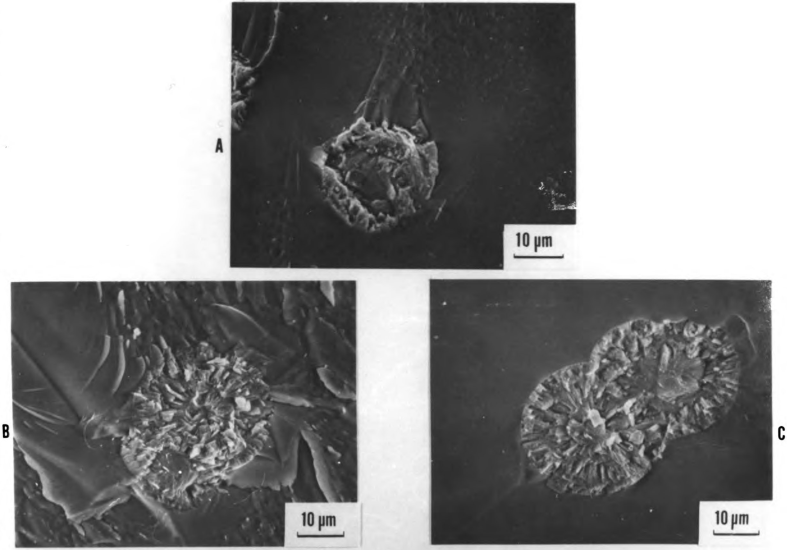
A
10 µm
B
10 µm
C
10 µm

Fig. 44. SEM fractographs showing

(A) A spherulite in the mirror region of fracture for specimen heat treated at 100°C for 45 min (2000x).

(B) A pocket left by spherulite in the mirror region of fracture for specimen heat treated at 100°C for 45 min (2000x).

(C) A spherulite in the mirror region of fracture for specimen heat treated at 100°C for 1 hr (2000x).

A

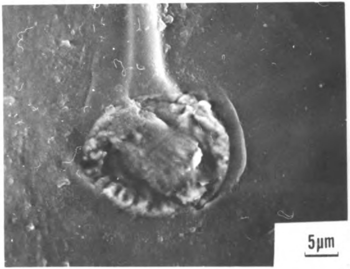

B

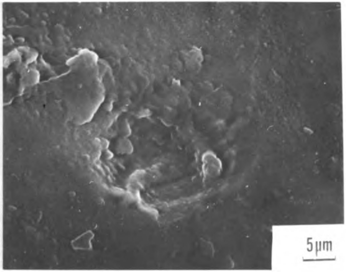

C

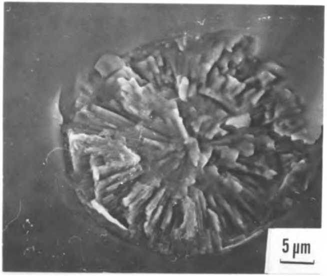

IV. DISCUSSION

As discussed in Section 1.3, the objectives of this research were to evaluate the flexure strength and elastic properties of partially crystallized selenium as a function of:

i) the elastic properties,
ii) the thermal-expansion coefficients,
iii) the size, shape, and distribution, and
iv) the volume fraction

of the component phases.

The results of the flexure strength and the elastic properties of partially crystallized selenium were presented in Section 3.3. In this chapter, Section 4.1 discusses the microstructure features observed in the heat-treated specimens. The theoretical predictions of the elastic properties are discussed in Section 4.2. The factors that control the flexure strength are examined in Section 4.3. In Section 4.4, the fractographs are analyzed, and the flexure strength as determined by the mirror radius is compared with the experimental results. The last section, 4.5, compares the flexure strength and elastic properties of partially crystallized selenium obtained in this work with the flexure strength and elastic properties of certain well-known glass-ceramics and glass-crystal composites.

4.1 Microstructure of Partially Crystallized Selenium

The photomicrographs of heat-treated samples were shown in Figures 16, 17, and 18 in Chapter II. The size, shape, and distribution of crystallites can be discussed on the basis of these photographs. The effect of internal stresses (due to differences of thermal-expansion coefficient between glassy phase and crystalline phase), the stress concentration (due to differences in elastic properties), and the crystal-glass bonding (due to difference in wettability of the glass and the crystalline phase) on the flexure strength and fracture of the partially crystallized selenium can also be analyzed.

The flexure strength and elastic properties are dependent on the microstructure of partially crystallized selenium. The microstructure is defined by the size, shape, and distribution of the crystalline phase in the glassy matrix. From Figures 16, 17, and 18, the shape of the spherulites is invariably spherical in every specimen. Hence shape of the crystallites is not a variable in the present work. The spherical shape of the crystalline phase helps considerably for making valid comparisons with the theoretical studies where the shape of the crystalline phase is generally assumed to be spherical. The distribution of the crystalline phase, as can be seen in detail in Figures 16, 17, and 18, can be considered uniform for specimens heat-treated at both 62°C and 82°C. Clustering of spherulites occurs only for the large-size crystals (approximately 30 to 50μm). These large-size crystals were present in specimens heat-treated at 100°C. Higher growth rate and lower number of crystallites per sq. mm. at this temperature contributes to such clustering. The heat-treatment schedules were selected to obtain widely scattered crystalline phases and to have very few clusterings.

Frey and Mackenzie[63] have found that the flexure strength and the elastic modulus of glass-Al_2O_3 and glass-ZrO_2 composites decrease drastically if internal stresses due to the difference in thermal expansion of the glass and crystalline phase were sufficient in magnitude to cause cracking of the glassy matrix during the preparation of the specimens. Binns[64] reported that glass-Al_2O_3 composites with angular Al_2O_3 grains cracked on cooling in cases where the thermal-expansion coefficient of the glass was higher than that of Al_2O_3. These cracks have originated from the internal stresses generated in the composite as it cooled from its fabrication temperature. High tangential stresses at the glass-Al_2O_3 interface are considered to be responsible for these cracks in the matrix. If the crystalline phase has a higher thermal expansion coefficient than the glassy phase, however, the cracks should originate around the crystalline phase at the glass-crystal interface. High radial stresses at the glass-Al_2O_3 interface are considered to be responsible for these circumferential cracks in the glass. The microstructures of partially crystallized selenium shown in Figures 16, 17, and 18, do not display any evidence of cracks in the glassy region or at the glass-crystal interface. This result can be explained by determining the radial and tangential stresses due to the difference in thermal-expansion coefficients of glassy and crystalline selenium. These stresses, according to Selsing's[65] equation, for the case of a spherical shape inclusion, are given by:

$$\sigma_r = -2\,\sigma_t = \frac{-(\alpha_m - \alpha_p)}{\dfrac{1 + \nu_m}{2\,E_m} + \dfrac{1 - 2\nu_p}{E_p}} \left(\frac{R^3}{r^3}\right)$$

where α_m = Thermal expansion coefficient of matrix;

α_p = Thermal expansion coefficient of crystalline phase;

ν_m = Poisson's ratio of crystalline phase;

E_m = Elastic modulus of matrix;

E_p = Elastic modulus of crystalline phase;

R = Radius of crystals

r = Radial distance from center of crystal to a point in glass matrix;

σ_r = Radial stress; and

σ_t = Tangential stress.

If the thermal expansion coefficient (α_p) of the trigonal selenium in this equation is taken to be the thermal-expansion coefficient of spherulites, then α_p $(37.79 \times 10^{-6}$ cm/cm/^{o}C) is slightly greater than α_m $(37.73 \times 10^{-6}$ cm/cm/^{o}C). In this case, a very small tensile radial stress would exist at the glass-crystal interface, and if failure occurs, the crack will have to propagate circumferentially around the spherulite. In microscopic studies there was no evidence of any circumferential cracks around the spherulites. The magnitude of internal stresses was not high enough to produce premature cracks in the specimen, as can be verified from the microstructures given. If the spherulites are considered to be made up of lamellas of trigonal selenium arranged annularly, as suggested by Fitton and Griffiths[13], then by the expected value of thermal-expansion coefficient of spherulite shown in Section 4.3.1, the magnitude of internal stress in the radial direction should have increased. This increase again would result in a circumferential crack at the glass-crystal interface. The microstructures do not show the existence of any cracks in the glassy matrix or in the glass-crystal interface. It can be concluded that premature cracks caused by internal stresses do not exist in partially crystallized selenium.

Evidence of good interfacial bonding is shown in Figure 45 by the adherence of the glassy selenium layer onto the spherulites of selenium. The fractured surface of the specimens, when observed under the microscope, do not show any evidence of separation of spherulites from the glassy matrix. All these facts suggest that the crystalline phase could be the weakest area in partially crystallized selenium.

4.2 Elastic Properties of Partially Crystallized Selenium

The elastic properties of partially crystallized selenium could be calculated from the elastic properties of its components by using models (Hashin's[36], Paul's[40], Maxwell and Eucken's[66], Hashin and Strikhman's[37] and Kingery's[66]). The elastic moduli of heterogeneous materials were theoretically determined by Hashin[36], (1962) with a concentric-sphere model. The upper and lower bounds for the elastic moduli of two-phase composite materials were obtained by an approximate method based on variational theories in elasticity. Hashin[36] determined these bounds for the effective elastic moduli of the two-phase composite by considering the change in strain energy in a loaded homogeneous body due to the insertion of nonhomogeneities. It is assumed that

(a) the particles are spherical, and

(b) the action of the whole heterogeneous material on any one inclusion is transmitted through a spherical shell lying in the matrix.

For those composite materials consisting of a matrix in which perfectly spherical inclusions are embedded, the analysis does not involve

Fig. 45. Polarized-light micrograph of spherulites of selenium illustrating the absence of separation at the glass-crystal interface.

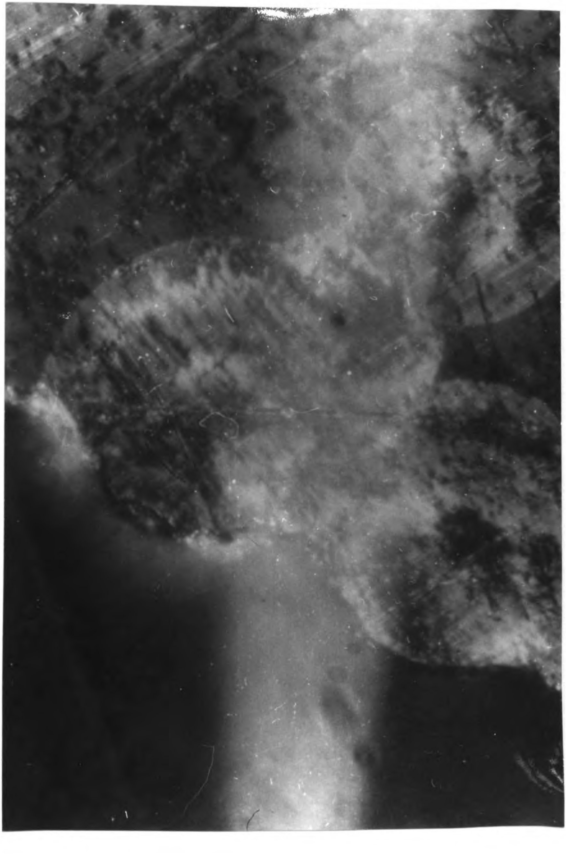

any approximations. The upper bound of the bulk modulus of a two-phase composite, k_1, is given by the expression

$$k_1 = \frac{K_m}{1 + \dfrac{(K_m - K_p)(4G_m + 3K_m)c}{K_m(4G_m + 3K_p) - 4G_m(K_m - K_p)c}}$$

and the lower bound of the bulk modulus of a two-phase composite, k_2, is given by

$$k_2 = K_m + (K_p - K_m)\frac{(4G_m + 3K_m)c}{4G_m + 3K_p + 3(K_m - K_p)c}$$

where c is the volume concentration of inclusions,

K_m is the bulk modulus of matrix,

K_p is the bulk modulus of inclusion, and

G_m is the bulk shear modulus of matrix.

With the results obtained for the bulk modulus, Young's modulus for the composite can be calculated from the expressions:

$$E = 3(1-2\nu)K \quad ; \quad G_m = \frac{E_m}{2(\nu_m + 1)}$$

where K is the bulk modulus,

E is the Young's modulus, and

ν is Poisson's ratio $\begin{cases} \approx 0.3 & \text{(assumed for amorphous phase)} \\ \approx 0.25 & \text{(assumed for crystalline phase).} \end{cases}$

The treatment becomes exact if the distributed phase occurs as perfect spheres.

Paul[40] (1960) has also determined the bounds of Young's modulus of two-phase composites by the variational theories of the theory of elasticity. He assumes that the stresses are the same, and are both tensile or compressive in matrix and particles. Both the matrix (material 1) and the dispersed particle (material 2) are assumed to be linearly elastic and isotropic. The upper and lower bounds of elastic modulus of two-phase composite are given by the following expression.

$$\frac{1}{\frac{f}{LE_1} + \frac{(1-f)}{M\,E_2}} \leq E \leq LE_1 f + ME_2(1-f)$$

where $L = \dfrac{1 - \nu_1 + 2m(m - 2\nu_1)}{1 - \nu_1 - 2\nu_1 2}$,

$M = \dfrac{1 - \nu_2 + 2m(m - 2\nu_2)}{1 - \nu_2 - 2\nu_2^2}$,

$m = \dfrac{\nu_1(1 + \nu_2)(1 - 2\nu_2)fE_1 + \nu_2(1 + \nu_2)(1 - 2\nu_1)(1 - f)E_2}{(1 + \nu_2)(1 - 2\nu_2)E_1 f + (1 + \nu_1)(1 - 2\nu_1)(1 - f)E_2}$,

ν_1 is Poisson's ratio of the matrix,

ν_2 is Poisson's ratio of the inclusion,

f is the volume fraction of inclusion,

E_1 is the elastic modulus of the matrix, and

E_2 is the elastic modulus of the inclusion.

These upper and lower bounds are generally too far apart to give a good estimate of the effective Young's modulus.

With Young's modulus of glassy selenium taken as $E_g = 1 \times 10^5$ kg/cm^2 and that of crystallized selenium as $E_c = 14 \times 10^5$kg/cm^2 (determined from Section 3.3.2), the upper and lower bounds of elastic modulus of the composite as suggested by the model of Hashin and of Paul were calculated. These values are presented in Table 9. In Figure 46 the calculated values of elastic modulus are plotted as a function of volume

TABLE 9

Elastic Modulus Calculated by the Relations of Hashin's[36], Paul's[40], Kingery's[66] and Maxwell and Eucken's[66] Relations

VOLUME	HASHIN (10^5 kg/cm^2)		PAUL (10^5 kg/cm^2)		KINGERY (10^5 kg/cm^2)		MAXWELL & EUCKEN (10^5 kg/cm^2)	
FRACTION	UPPER	LOWER	UPPER	LOWER	UPPER	LOWER	UPPER	LOWER
0	1.0000	1.0000	1.0000	1.0000	1.0000	1.0000	1.0000	1.0000
10	1.1726	1.1526	2.30	1.10	3.30	1.106		1.333
20	1.4532	1.3371	3.65	1.25	5.55	1.237		1.75
30	1.9889	1.5646	5.00	1.50	7.85	1.40		2.286
40	3.4179	1.8521	6.25	1.65	10.10	1.85		3.00
50	19.1828	2.2271	7.50	2.00	12.40	1.92		4.00
60			8.80	2.30			7.20	5.50
70			10.16	2.876			8.526	8.00
80			11.811	3.914			10.178	
90			10.162	6.109			11.998	
100			14.00	14.00	24.00	24.00	14.00	14.00

Fig. 46. Plot of calculated values of elastic modulus (according to the expressions of Paul[40] and Hashin[36]) as a function of volume fraction of crystallites.

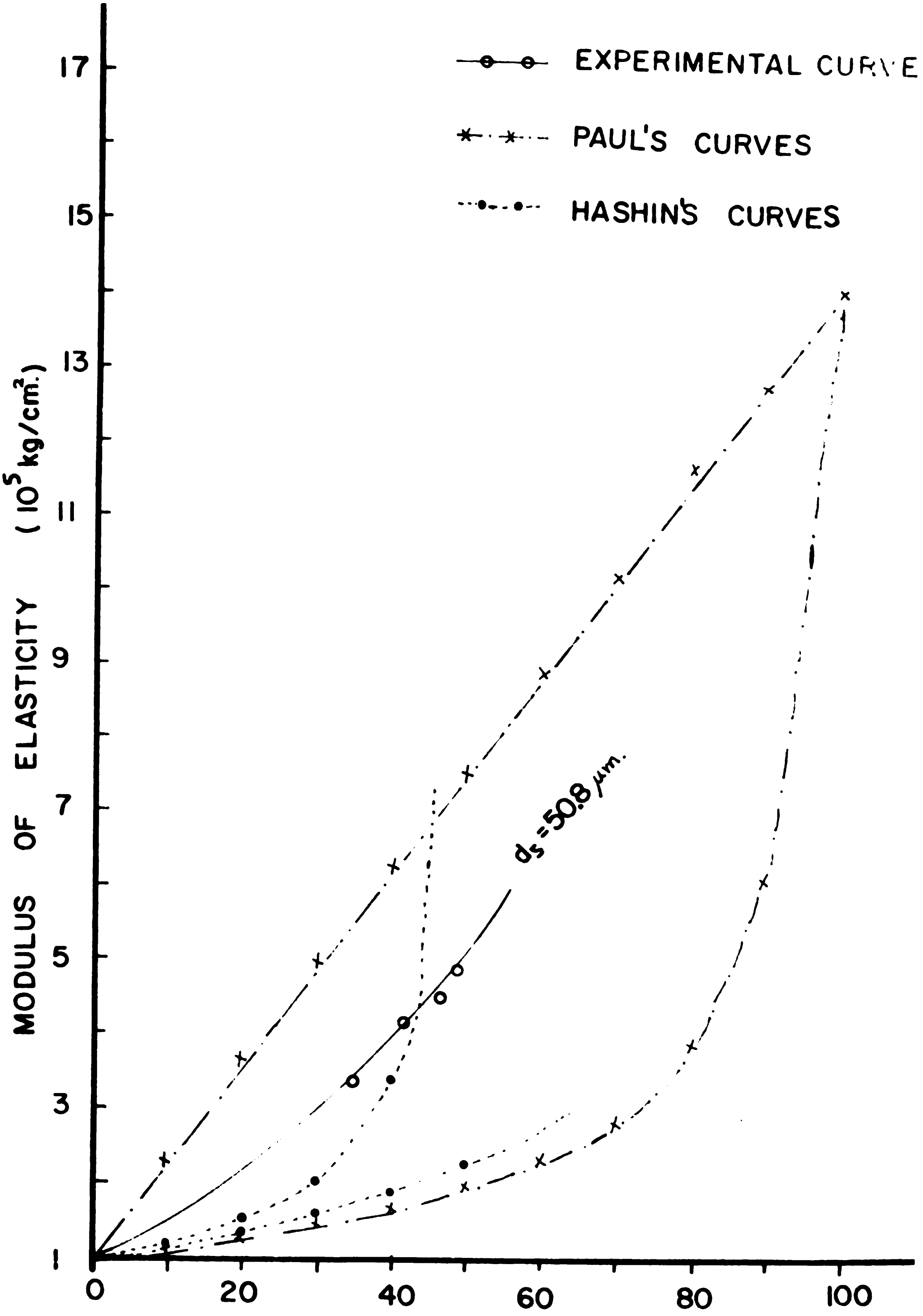

EXPERIMENTAL CURVE
PAUL'S CURVES
HASHIN'S CURVES
$d_s = 50.8\ \mu m.$
MODULUS OF ELASTICITY (10^5 kg/cm^2.)
1
3
5
7
9
11
13
15
17
0
20
40
60
80
100
VOLUME FRACTION OF SPHERULITES (%)

fraction of crystallites. The experimentally determined values of elastic modulus of partially crystallized selenium containing 50μm spherulites are also plotted in the same figure. As can be seen from the figure, Paul's curve deviates drastically from the experimental values. Hasselman and Fulrath,[41,42] working with D-glass-Tungsten spheres and D-glass-Al_2O_3, also came to the same conclusion. All previous investigations (Frey and Mackenzie,[63] Hasselman and Fulrath[45]) have found values obtained by Hashin's expression to be close to the experimental values. But in the present work the experimental values obtained are higher than both the upper- and lower-bound curves of Hashin's expressions. A possible reason for such a deviation may be the value assumed for Poisson's ratio (0.3). The value of the elastic modulus of spherulite (14×10^5 kg/cm^2) also introduces an error. The elastic modulus of spherulite, as obtained by extrapolation of the experimental curves in Figure 29, is an approximate value.

4.3 Mechanical Properties of Partially Crystallized Selenium

Flexure strength of partially crystallized selenium is affected by many factors, as shown in the beginning of this chapter. Of the factors considered earlier in the section, the shape and distribution of the crystalline phase are not important in the present case. The role of the other parameters is discussed in this section.

4.3.1 Effect of Thermal Expansion Differences

As shown in Figure 23, the flexure strength of partially crystallized selenium having small size crystals (d_s = 12.75 μm) decreases drastically with increasing volume fraction of crystallites. Decrease of flexure strength of partially crystallized selenium having large-size crystals (d_s = 50.80μm), however, was not so drastic. The decrease of flexure strength of partially crystallized selenium containing crystal sizes between 12.75 and 50.80μm were intermediate between these two extremes, as shown in Figure 24.

One possible explanation of the decrease of flexure strength with the introduction of spherulites of selenium in the glassy matrix is that the crystals are stressed in tension radially, and in compression tangentially, owing to a difference between the thermal-expansion coefficients of spherulitic selenium and glassy selenium. Selsing's[65] equation given in Section 4.1 shows that such stresses were extremely small. This hypothesis was also supported by the fact that there were no premature cracks observable in the microstructure of partially crystallized selenium (as shown in Figures 16, 17, and 18).

The coefficient of thermal expansion along the spiral should be relatively high compared with the coefficient of thermal expansion along the C-direction in the lamellas. This finding can be attributed to the van der Waals bond that holds these lamella together in the ring. A similar feature can be observed in graphite. The coefficient of thermal expansion along the direction parallel to the C-axis is 27 times the value along the direction perpendicular to the C-axis[67]. This highly anisotropic behavior of graphite was attributed to the van der Waals bonding that occurs between the layers. Similar studies on spherulitic selenium are not available in literature. If one assumes the behavior of selenium to be similar to that of layer-structured graphite, it is reasonable to expect a higher coefficient of thermal expansion along the spiral compared with that of C-direction in trigonal selenium. This difference will result in a tensile stress perpendicular to the lamella. On application of external load, these lamellas tend to cleave owing to the existing internal stresses, as can be seen in the micrographs 40, 41A, and 44C.

Another factor worth considering is the temperature of heat treatment. The thermal-expansion coefficient would not cause large internal stress build-up in the material, because the heat-treatment temperatures are low (62°, 82°, and 100°C). It can be concluded, therefore, that the internal stresses are not high enough to cause microcracking in the absence of external loading.

4.3.2 Effect of Difference in Elastic Moduli

When an external force is applied to the specimen, the difference in elastic properties of spherulitic selenium and glassy selenium in a partially crystallized specimen will cause stress-concentration effects to occur near the spherulites. Hasselman and Fulrath[41,42] have investigated this case with glass-Al_2O_3 and glass-Tungsten composites. Theoretically, the analysis could be made according to the stress concentration around a circular inclusion in a two-dimensional plate as determined by Goodier. The maximum stress-concentration factor is 1.4. It is important to note here that the peripheral region of spherulites of selenium is also in the region of stress concentration. The experimental results in Section 3.4.1 show that the glass-crystal interface and the glassy matrix in partially crystallized selenium were stronger than the spherulite.

The elastic moduli of glassy selenium and partially crystallized selenium were determined according to the experimental method shown in Section 2.4.2. The stiffness (K) of the specimens was determined from the load-deflection curves of unnotched specimens deformed in three-point bending. Figure 29 shows the plot of elastic modulus of partially crystallized selenium with increasing volume fractions (for different sizes of spherulites). The plot indicates that the slope of the curve decreases with increasing size of the crystals. For crystal size 12.75 to 19.05μm, the change in slope is not appreciable. The small change in slope of curves could be attributed to the errors in measuring very small volume fractions of crystallites. For large-size crystals (50.8μm) the curve for elastic modulus versus volume fraction is not linear. These results could be explained on the basis of internal structure of spherulites.

A spherulite, when observed at high magnification, shows two distinct areas: the central region, which may be called the core of the spherulite; and the outer region of the spherulite. In small-size spherulites (12.75, 15.78, and 19.05μm) it can be observed from Figures 41B, 44A, and 44B that the core sizes are as large as the diameter of the spherulites. The large core is due to the fact that the lamellas of trigonal selenium are arranged as shown in Figure 47. This arrangement results in all the spirals beginning in the center of the core; hence the center tends to have a higher density than the peripheral region. In a small-size crystal, the core size is equal to the diameter of the spherulite, because the size of crystal is such that the lower-density peripheral region is just being formed. The core of the crystal can be expected to have a higher elastic modulus than the peripheral region of the crystal. The small-size crystals (12.75, 15.87 and 19.06μm), when added to the glassy matrix, tend to increase elastic moduli of the composite more than do the larger-size crystals (22.22, 25.40, and 50.80μm). The larger spherulites (50.8μm), as can be seen

Fig. 47. Arrangement of lamellas in the spherulite.

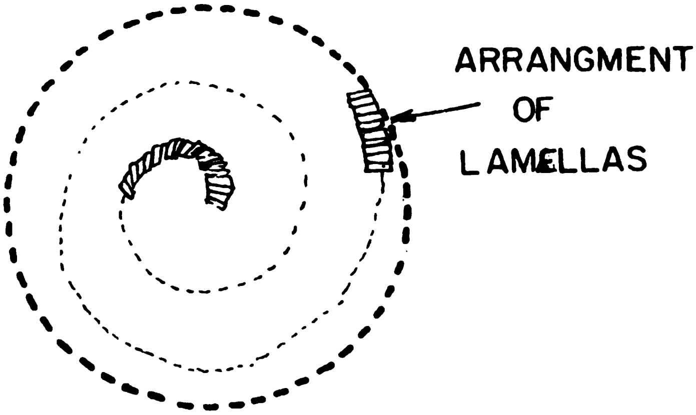
ARRANGMENT
OF
LAMELLAS

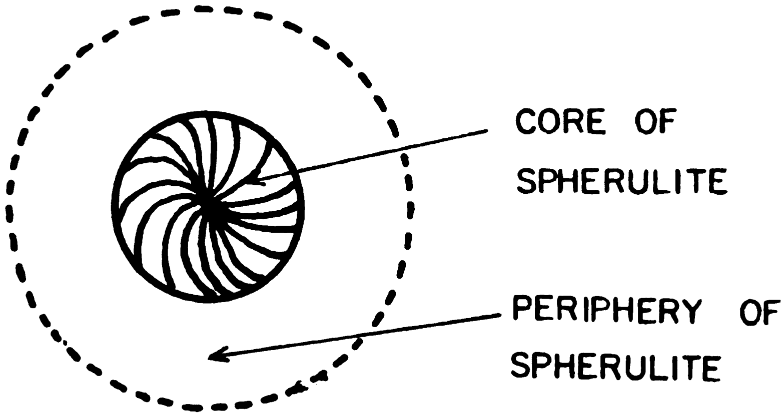
CORE OF
SPHERULITE
PERIPHERY OF
SPHERULITE

in Figures 36C, 43C, and 44C, have core sizes approximately 1/3 the size of the spherulite. Hence a larger volume of the peripheral region exists in the spherulites. Since the peripheral regions have the lowest elastic modulus, the presence of large-size spherulites tends to decrease the elastic modulus of partially crystallized selenium. Another important fact to be noted is that the elastic modulus of a spherulite is higher than the elastic modulus of a single crystal of trigonal selenium in the C-direction. The elastic modulus of the spherulite varies from 14 to 24 x 10^5 kg/cm^2, the smaller ones having higher values. This value of elastic modulus has been determined after extrapolating the experimental curves shown in Figure 29.

The plots of Figure 29 do show that the zero-volume-fraction elastic modulus is 0.7 to 1.0 x 10^5 kg/cm^2. This value equals the elastic modulus of amorphous selenium determined experimentally in this work (shown in Table 7).

The composite property of a two-phase material can be analyzed with the help of ideal models. In the first model[66], slabs of each phase are arranged alternately to form the composite. The elastic modulus of the composite in the direction parallel to the surface of the slabs is given by the expression:

$$E_m = V_g E_g + V_{cry} E_{cry}$$

where E_m = elastic modulus of composite,

E_g = elastic modulus of matrix,

E_{cry} = elastic modulus of crystalline phase,

V_g = volume fraction of matrix, and

V_{cry} = volume fraction of crystalline phase.

The elastic modulus of the composite in a direction perpendicular to the surface of the slabs is given by the following expression:

$$1/E_m = V_g/E_g + V_{cry}/E_{cry} ,$$

or

$$E_m = E_g E_{cry}/V_g E_{cry} + V_{cry} E_g$$

These curves represent the upper and the lower limits of the elastic modulus of the composite.

Another model by Maxwell-Eucken[66] considers spheres of one phase distributed in an isotropic continuous matrix of another phase. The composite elastic modulus is given by:

$$E_m = E_c \frac{1 + 2V_d \dfrac{1 - E_c/E_d}{1 - E_c/E_d}}{1 - V_d \dfrac{1 - E_c/E_d}{E_c/E_d + 1}}$$

where E_m = Elastic modulus of the composite,
E_c = Elastic modulus of the continuous phase,
E_d = Elastic modulus of the discontinuous phase, and
V_d = Volume fraction of the discontinuous phase.

When E_c is much greater than E_d, then

$$E_m \cong E_c \frac{1 - V_d}{1 + \dfrac{V_d}{2}}$$

However, if E_c is much less than E_d, then

$$E_m \cong E_c \frac{1 + 2V_d}{1 - V_d}$$

These expressions have been plotted in Figure 29. Equations 23 and 24 represent upper and lower limits of elastic modulus of the composite. As can be seen from this figure, the upper and lower limits of elastic modulus represented by the Maxwell-Eucken relationship tends to be closer to the experimental results than the upper and lower limits obtained by the slab model.

4.3.3 Effect of size of glassy and crystalline selenium

The partially crystallized selenium studied in this work had volume fractions of spherulitic selenium varying from 0 to 50% and the size of spherulitic selenium varying from 5 to 50.8μm. The morphologies of the crystalline and the glassy phases are of the greatest importance in determining the flexural stress. There are two possible cases:

1) The glass-crystal composite contains the crystalline phase such as the discontinuous phase, and the glassy phase as the continuous phase. Schematically such a composite can be represented by Figure 48(A).

2) The glass-crystal composite contains the crystalline phase as the continuous phase and the glassy phase as the discontinuous phase. Schematically this structure is represented in Figure 48(B).

It is logical to consider that the flexure strength of the composite in case (1) would be largely influenced by the properties of the continuous glassy phase. This condition is generally fulfilled when the volume fraction of the crystalline phase is small (below 10%). The microstructure of partially crystallized selenium with volume fractions of spherulitic selenium V_s = 2.09, 3.77, and 6.55% should be dependent on the glassy phase. In case (2) the microstructure is achieved with larger size and higher volume fraction crystallites. In this condition,

Fig. 48. (A) Schematic representation of discontinuous crystal phase and continuous glass phase.
(B) Schematic representation of continuous crystal phase and discontinuous glass phase.

(A)

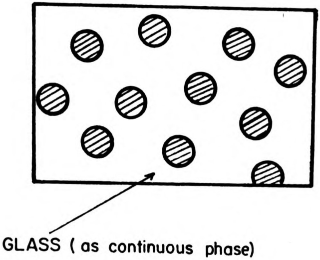

(B)

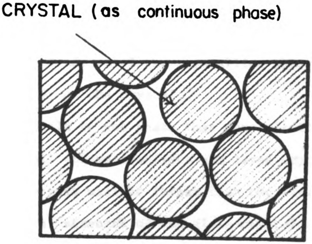

the crystalline phase tends to become the continuous phase. It is logical to assume that the crystalline phase would be the phase controlling the fracture strength of such a glass-crystal composite.

In both these cases, the severity and the distribution of microcracks in the glass or in the crystalline phase would also affect the mechanical strength of the glass-crystal composite. The glass-crystal composite has mechanically hard crystalline dispersions; the fracture will be initiated within the glass matrix. Hasselman and Fulrath[47] have shown that hard crystalline phase tends to restrict the flaw size in the glassy matrix, and that the flexure strength is controlled by the interparticle spacing between the crystals in the glassy matrix. This hypothesis implies that the flaws present in the glass are terminated at the crystal-glass boundaries, whereas the spacing between the crystals or the mean free path in the glass phase will be a critical parameter in determining the mechanical strength. The crack mean free path, p, is given by:

$$p = d(1-V)/V$$

where V is the volume fraction of the crystalline phase, and

d is the diameter of the crystal.

If the glassy matrix would be the phase that controls the flexure strength, then for small volume fractions and large crystal diameters the value of mean free path will be larger than the flaw size, C. Therefore the mechanical strength of the glass-crystal composite will not be strongly influenced by the crystalline distribution. If the volume fraction of the crystalline phase is small, however, the mean free path will be smaller than the flaw size, and then the strength would be influenced by the crystalline dispersion. In this latter case, Hasselman and Fulrath show that the strength is proportional to $p^{-\frac{1}{2}}$, provided that p is replaced by the flaw size C.

In the present work, as can be seen from Section 3.2.2, the volume fraction of spherulitic selenium ranged from 0 to 50%, the crystal size varied from 5 to 50.8μm, and the mean free paths from 59.0 to 743μm. By inserting appropriate values in Griffith's equation, the flaw size of each specimen was calculated with known volume fraction, spherulite size, elastic modulus, and fracture surface energy. Table 10 shows that the flaw size (C = 42.04μm) of partially crystallized selenium having a low volume fraction (V_s = 2.09%) and small crystal size (d_s = 15.8μm), is smaller than the mean free path (p = 743μm). In such a case, the flexure strength should not be affected by increasing the volume fraction of the spherulite. But the results show that the flexure strength decreases drastically with increase of volume fraction of small-size (15.8μm) spherulites. The results suggest that the glassy phase present in the partially crystallized selenium having low volume fraction crystallites does not influence the mechanical strength.

At higher volume fractions (V_s = 46.0%) and with 50.8μm size of spherulites, the mean free path (p = 59.6μm) is smaller than the flaw size (C = 90.5μm). Flexure strength of partially crystallized selenium in Figure 25 shows no significant change. It is therefore possible to conclude that the glassy phase present in partially crystallized selenium does not contain the flaws or the microcracks that result in decrease of its flexure strength.

Another possibility is to consider the weakest area in a glass-crystal composite to be the crystalline phase or the interface between the glass and crystalline phases. Usumi and Sakka[68] have suggested that mechanical strength, σ, of glass-ceramics is dependent on the mean crystal diameter, d, according to the relationship

$$\sigma = kd^{-\frac{1}{2}}$$

where k is a constant, and

d is the diameter of the crystal.

This relation implies that the crack length, C, in Griffith's equation is proportional to or equal to the crystal diameter. Griffith's equation applied to a glass-crystal composite in the work of Usumi and Sakka suggests that the critical flaws are present within the crystalline regions and do not extend into the glassy phase, or that they exist at the crystal-glass interface and are therefore proportional to the circumference of the crystal.

In the present work, the flaw sizes in the partially crystallized selenium having constant volume fractions of spherulites were determined using the following form of Griffith's equation:

$$\sigma_C = (2E_c\gamma_c/\pi C)^{\frac{1}{2}}$$

or

$$C = (2E_c\gamma_c/\sigma_c^{\,2}\pi)$$

where σ_c is the flexure strength of glass-crystal composite,

E_c is the elastic modulus of composite,

γ_c is the fracture surface energy of the composite, and

C is the flaw size.

Elastic modulus (E_c) of the composite was calculated from the load-deflection curve obtained from the three-point bend test. Fracture surface energy (γ_c) was determined with notched specimens in three-point bend tests. The experimental results of flexure strength, elastic modulus, and fracture surface energy for each melt are shown in Tables 5 and 8. The flaw sizes in the partially crystallized selenium samples having various volume fractions of spherulites (V_s = 2.09, 3.37, 6.55, 8.13 and 14.16%) have been determined and tabulated in Table 10. In this table, an attempt is made to see if the diameter of the spherulites is in any way related to the flexure strength. The flaw size in each specimen is divided by the diameter of the spherulites present. It is noted from Table 6 that the flaw size is invariably equal to 1.0 to 3.0 times the diameter of the spherulite.

The weakest area in the spherulites, as shown in Section 4.1, is the peripheral regions of the spherulites. SEM fractograph Figure 40 shows clearly the path of fracture. The interface of the glass and crystalline phase does not show any discontinuities. No visible signs of cracks at the crystal-glass interface are seen anywhere in the fractographs. The core of the spherulites, as seen from Figure 40, is definitely not the weak area of the spherulites. The conclusion then is that the peripheral region of the spherulites contains the weakest area, and the fracture in spherulite traverses through it.

The schematics of the fracture paths shown in Figure 49 in spherulites are based on the fractographs shown in Figures 44A, 41A, and 43C. This schematic diagram shows that in small-size crystals ($d_s < 15.0\mu m$) the fracture path is approximately 1.57 D and in large-size crystals ($d_s < 50.0\mu m$) the fracture path is approximately 1.19 D. The ratio C/d_s of the flaw size and the size of spherulites as obtained in Table 6, suggests that the fracture travels along the periphery of the spherulites, as shown in Figure 49. (D is defined in Figure 49.)

TABLE 10

Flaw Size as Determined by Griffith's Equation for Amorphous and Partially Crystallized Selenium

HEAT TREATMENT					FLAW SIZE (C) (μm)	DIAMETER OF SPHERULITE (μm)	MEAN FREE PATH (p) (μm)
AMORPHOUS SELENIUM					5.00		
V_s = 2.09%							
MELT	A	62°C	200 hr	S-2	37.31	12.75	597.30
				S-3	21.68	12.75	
		62°C	250 hr	S-4	42.04	15.87	743.46
				S-5	21.51	15.87	
				S-6	35.94	15.87	
	B	62°C	250 hr	S-4	31.83	15.87	
				S-5	16.85	15.87	
				S-6	26.17	15.87	
	C	62°C	200 hr	S-1	14.89	12.75	
				S-2	20.33	12.75	
				S-3	20.26	12.75	
V_s = 3.73%							
MELT	A	62°C	311 hr	S-7	71.89	25.4	655.57
	B	62°C	311 hr	S-7	37.05	25.4	
				S-8	25.72	25.4	
	C	62°C	250 hr	S-4	75.46	15.8	407.80
				S-5	43.08	15.8	
				S-6	41.09	15.8	
	A	82°C	4 hr	S-2	68.39	19.05	
				S-3	21.07	19.05	
	B	100°C	45 min	S-1	28.55	12.75	
				S-2	33.95	12.75	
				S-3	50.54	12.75	

TABLE 10 (Continued)

V_s = 6.55%						
MELT A	82°C	6 hr	S-4	16.96	22.22	317.02
			S-5	37.87	22.22	
			S-6	35.42	22.22	
B	82°C	4 hr	S-1	44.806	19.05	271.79
			S-2	10.82	19.05	
			S-3	34.537	19.05	
C	82°C	4 hr	S-1	22.829	19.05	
			S-2	31.37	19.05	
			S-3	38.57	19.05	
C	62°C	311 hr	S-7	103.29	25.40	362.39
			S-8	58.69	25.40	
			S-9	62.61	25.40	
V_s = 8.13%						
MELT A	100°C	45 min	S-1	47.46	15.87	179.33
			S-2	72.55	15.87	
			S-3	75.10	15.87	
B	82°C	6 hr	S-4	67.23	25.40	287.02
			S-5	31.42	25.40	
			S-6	32.92	25.40	
C	100°C	45 min	S-1	84.44	15.87	179.33
			S-2	51.57	15.87	
			S-3	72.06	15.87	
V_s = 14.16%						
MELT A	82°C	8 hr	S-7	35.91	25.40	153.98
			S-8	37.95	25.40	
			S-9	82.98	25.40	
B	100°C	1 hr	S-4	37.98	22.22	134.70
			S-5	38.39	22.22	
			S-6	35.23	22.22	
B	82°C	8 hr	S-7	44.85	31.75	192.47
			S-8	35.24	31.75	
			S-9	53.13	31.75	

TABLE 10 (Continued)

C	100°C	1 hr	S-4	61.19	22.22	134.70
			S-5	26.58	22.22	
			S-6	84.40	22.22	
C	82°C	6 hr	S-4	55.59	22.22	134.70
			S-5	59.14	22.22	
			S-6	37.40	22.22	
V_s = 46.00%						
MELT A	100°C	1½ hr	S-7	90.55	50.80	59.63
B	100°C	1½ hr	S-7	73.72	38.10	115.78
			S-8	115.44	50.80	119.04
			S-9	60.44	44.45	82.37
C	100°C	1½ hr	S-7	93.13	50.80	82.71
			S-9	130.67	50.80	60.99

Fig. 49. Schematic diagram showing path of fracture in a spherulite.

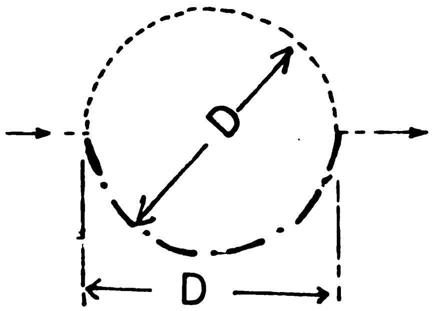

FRACTURE PATH

$= 3.14/2\ D$

$= 1.57\ D$

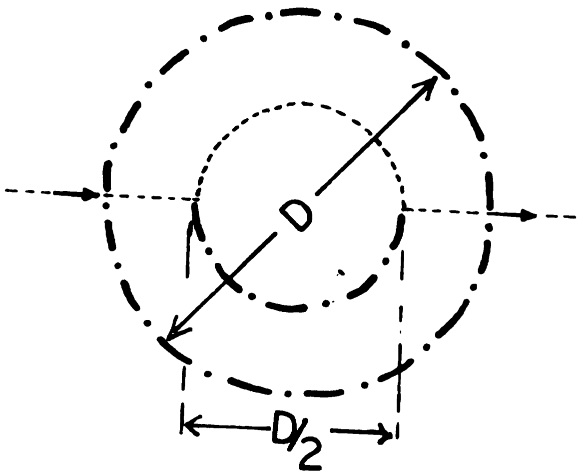

FRACTURE PATH

$= 2D/4 + 3.14D/4$

$= 1.285\ D$

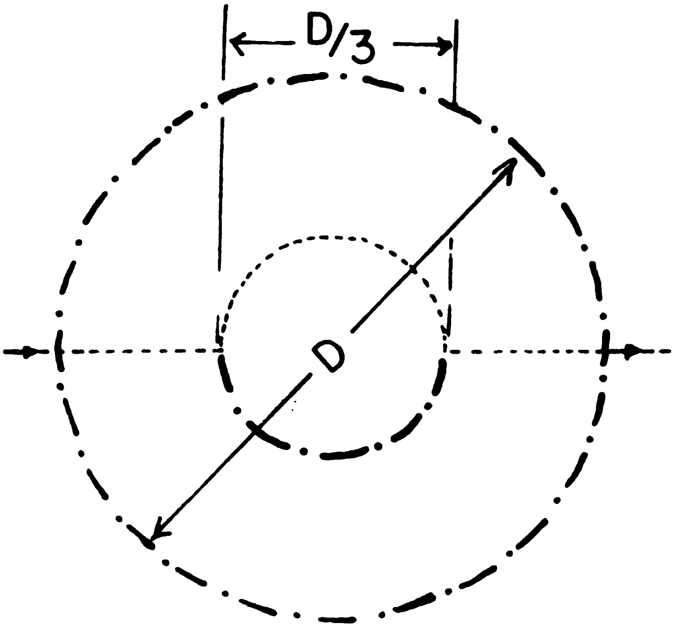

FRACTURE PATH

$= 2D/3 + 3.14D/6$

$= 1.19\ D$

Another possible plot can be made with flexure strength as a function of (diameter of spherulite)$^{-\frac{1}{2}}$. This plot is shown in Figure 50. Table 11 presents the experimental data for this plot.

The growth rate of spherulites were determined in this work as shown in Table 12. As expected, the growth rate for heat treatment at 62°C is very small (approx. 0.157μm/hr) and that at 100°C is very large (approx. 48.78μm/hr). As can be seen from Table 12, the number of spherulites nucleated in unit area is very high at 62°C (approx. 100.57/sq.mm.) and very small at 100°C (approx. 40.23/sq.mm.). Hence if flaws are present, the partially crystallized selenium specimens could be expected to show drastic decrease in strength when heat-treated at 62°C. The decrease of strength would not be drastic when heat-treated at 100°C.

4.3.4 Effect of Volume Fraction of Crystalline Phases on Flexure Strength of Partially Crystallized Selenium

In order to understand the effect of volume fraction of the crystalline phase of selenium, the flexure strength is plotted in Figures 23, 24, and 25 as a function of volume fraction for different sizes of spherulites. The fixed sizes of spherulites are 12.57, 15.78, 19.05, 22.22, 25.40, and 50.80μm. The flexure strength decreases with the increase of volume fraction of spherulites. The decrease in flexure strength for 12.75μm size of spherulites is drastic, compared with the decrease in strength for 25.40μm size of crystals. The flexure strength does not show any decrease for 50.80μm size. The change in flexure strength with increasing volume fraction of crystallites can be studied more clearly by means of the Weibull's[33] plot. Figure 51 shows the frequency of fracture, N_f, as a function of the flexure strength of

TABLE 11

Flexure Strength of Partially Crystallized Selenium Versus (Size of Crystals)$^{-\frac{1}{2}}$

HEAT TREATMENT					FLEXURE STRENGTH (kg/cm^2)	DIAMETER OF SPHERULITE (μm)	(DIAMETER OF SPHERULITE)$^{-\frac{1}{2}}$ (cm)
V_s = 2.09%							
MELT	A	62°C	200 hr	S-1	X	12.75	357.07
				S-2	292.33	12.75	
				S-3	388.36	12.75	
		62°C	250 hr	S-4	283.10	15.87	397.24
				S-5	382.28	15.87	
				S-6	257.56	15.87	
	B	62°C	250 hr	S-4	304.72	15.87	
				S-5	450.79	15.87	
				S-6	384.07	15.87	
	C	62°C	200 hr	S-1	438.17	12.75	357.07
				S-2	380.58	12.75	
				S-3	382.76	12.75	
V_s = 3.73%							
MELT	A	62°C	311 hr	S-7	254.66	25.4	503.98
				S-8	203.78	25.4	
				S-9	209.89	25.4	
	B	62°C	311 hr	S-7	213.38	25.4	
				S-8	305.10	25.4	
				S-9	X	25.4	
	C	62°C	250 hr	S-4	203.13	15.8	397.07
				S-5	347.54	15.8	
				S-6	313.08	15.8	
	A	82°C	4 hr	S-1	455.79	19.05	436.46
				S-2	351.53	19.05	
				S-3	362.83	19.05	
	B	100°C	45 min	S-1	360.10	12.75	357.07
				S-2	289.61	12.75	
				S-3	X	12.75	

TABLE 11 (Continued)

V_s = 6.55%						
MELT A	82°C	6 hr	S-4	325.17	22.22	471.38
			S-5	315.91	22.22	
			S-6	358.74	22.22	
B	82°C	4 hr	S-1	252.65	19.05	436.46
			S-2	386.04	19.05	
			S-3	321.24	19.05	
C	82°C	4 hr	S-1	501.54	19.05	436.46
			S-2	407.35	19.05	
			S-3	317.43	19.05	
C	62°C	311 hr	S-7	225.25	25.4	503.98
			S-8	232.67	25.4	
			S-9	181.97	25.4	
V_s = 8.13%						
MELT A	100°C	45 min	S-1	244.31	15.87	397.24
			S-2	332.01	15.87	
			S-3	295.62	15.87	
B	82°C	6 hr	S-4	286.16	25.4	503.98
			S-5	360.60	25.4	
			S-6	386.38	25.4	
C	100°C	45 min	S-1	278.24	15.87	397.24
			S-2	399.92	15.87	
			S-3	242.07	15.87	

Fig. 50. Plot of flexure strength of partially crystallized selenium versus (size of crystallites)$^{-\frac{1}{2}}$.

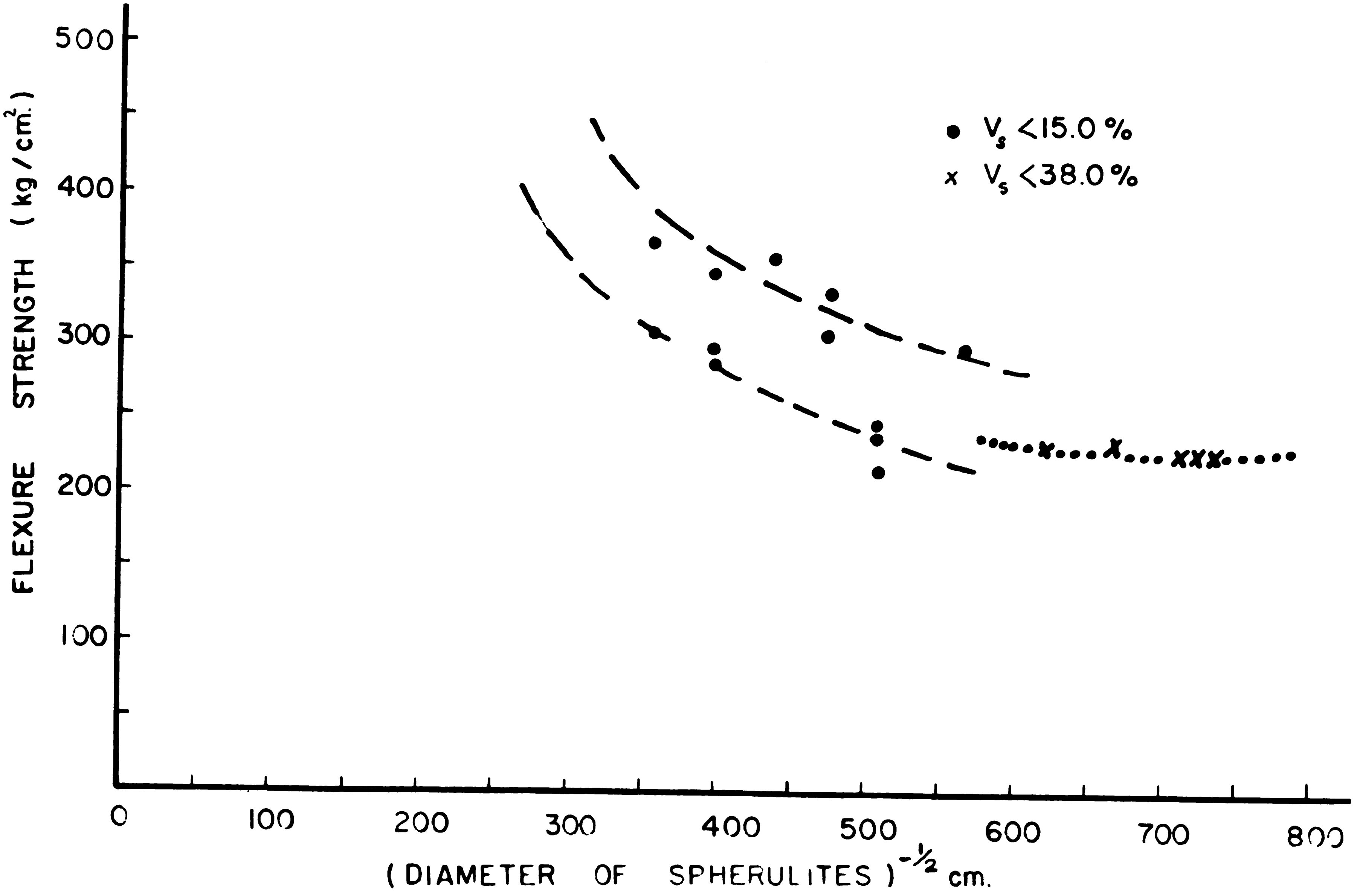
● $V_s < 15.0\%$
x $V_s < 38.0\%$
FLEXURE STRENGTH (kg/cm^2.)
500
400
300
200
100
0
100
200
300
400
500
600
700
800
(DIAMETER OF SPHERULITES)$^{-1/2}$ cm.

TABLE 12

Growth Rate and Number per sq. mm. of Spherulitic Selenium at 100°C, 82°C, and 62°C.

(A) GROWTH RATE OF SPHERULITES

Temperature	Melt	Size after Different Heat Treatment Times			Average Growth Rate for Each Melt (μm/hr)	Growth Rate at Each Temp. (μm/hr)
		45 min	1 hr	1½ hr		
100°C	A	15.89	29.55	50.80	42.50	48.78
	B	12.75	21.16	44.45	46.64	
	C	15.87	22.22	50.82	57.20	
		4 hr	6 hr	8 hr		
82°C	A	19.05	22.22	25.4	1.59	2.118
	B	19.05	25.40	31.75	3.175	
	C	19.05	22.22	25.40	1.59	
		200 hr	250 hr	311 hr		
62°C	A	12.75	15.80	25.4	.1574	.1570
	B	8.46	15.87	25.4	.1562	
	C	12.75	15.80	25.4	.1574	

TABLE 12 (Continued)

(B) NUMBER OF SPHERULITES PER SQ. MM. IN MELT A

Temperature	Number of Spherulites per sq. mm. after Different Heat-Treated Times		
	45 min	1 hr	1½ hr
100°C	17.24	22.99	40.23
	4 hr	6 hr	8 hr
82°C	20.11	28.74	48.85
	200 hr	250 hr	311 hr
62°C	66.09	77.59	100.57

of the amorphous and partially crystallized selenium specimens. The amorphous selenium specimens show a higher value for the most probable flexure strength (approx. 450 kg/cm^2), and a large scatter in the results as shown by the larger half band width of the peak (250 kg/cm^2). With increasing size of spherulites the flexure strength decreases, reaching the lowest value for 50.80μm size of spherulites. In Figure 51 it is also seen that the most probable flexure strength of 0.00 size of spherulites agrees with the most probable flexure strength evaluated from Weibull's curve for amorphous selenium. Another important fact can be obtained by plotting the half band width of the Weibull's curves as a function of various sizes of spherulites. In Figure 52 such a plot is shown. The trend of the curve shows that half band width decreases with increasing size of crystallites in partially crystallized selenium specimens.

Another approach would be to see how the flexure strength changes with increasing size of spherulites for different volume fraction of spherulites. In Figures 32, 33, and 34 the flexure strength is plotted as a function of size of spherulites for 2.09, 3.73, 6.55, 8.13, and 14.16 volume percent of spherulites. As can be seen from the figure, the flexure strength decreases for volume fractions 2.09, 3.73, and 6.55, with increase of size of spherulites of selenium. Weibull's curve has been plotted for this case also, and is shown in Figure 53. The most probable flexure strength is also plotted. The flexure strength decreases with increase of volume fractions. The most probable flexure strength, as predicted from the intersection of the curve with 0.00 volume fraction of crystallites, agrees with the most probable flexure strength determined from Weibull's curve for amorphous selenium. The

Fig. 51. Plot of frequency of fracture as a function of flexure strength of amorphous and partially crystallized selenium (for constant size of spherulites).

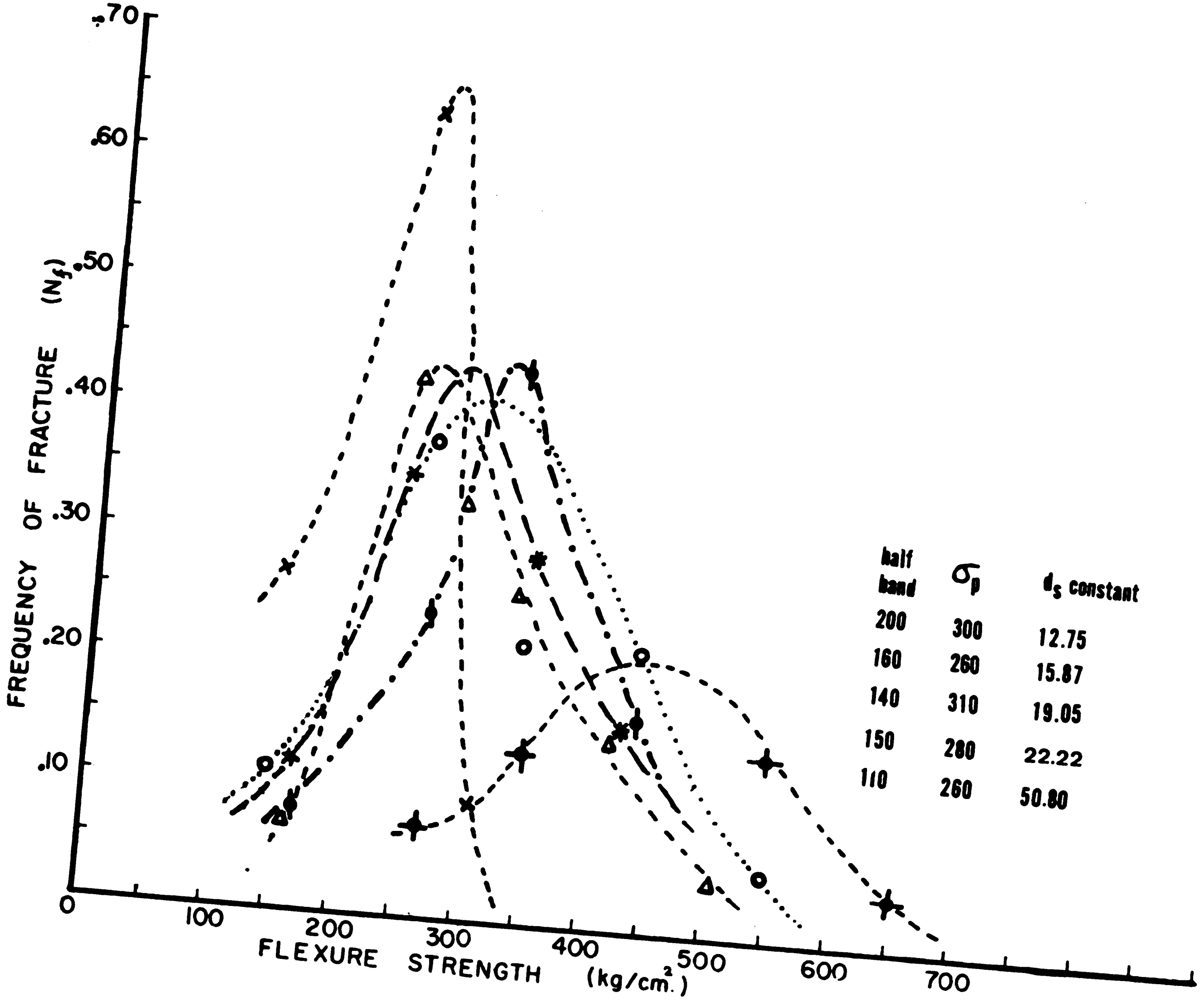
.70
.60
.50
.40
.30
.20
.10
0
FREQUENCY OF FRACTURE (N_f)
100
200
300
400
500
600
700
FLEXURE STRENGTH (kg/cm.²)
half band
200
160
140
150
110
σ_p
300
260
310
280
260
d_s constant
12.75
15.87
19.05
22.22
50.80

Fig. 52. Plot of half band width of Weibull's curves of Figure 51, as a function of size of spherulites.

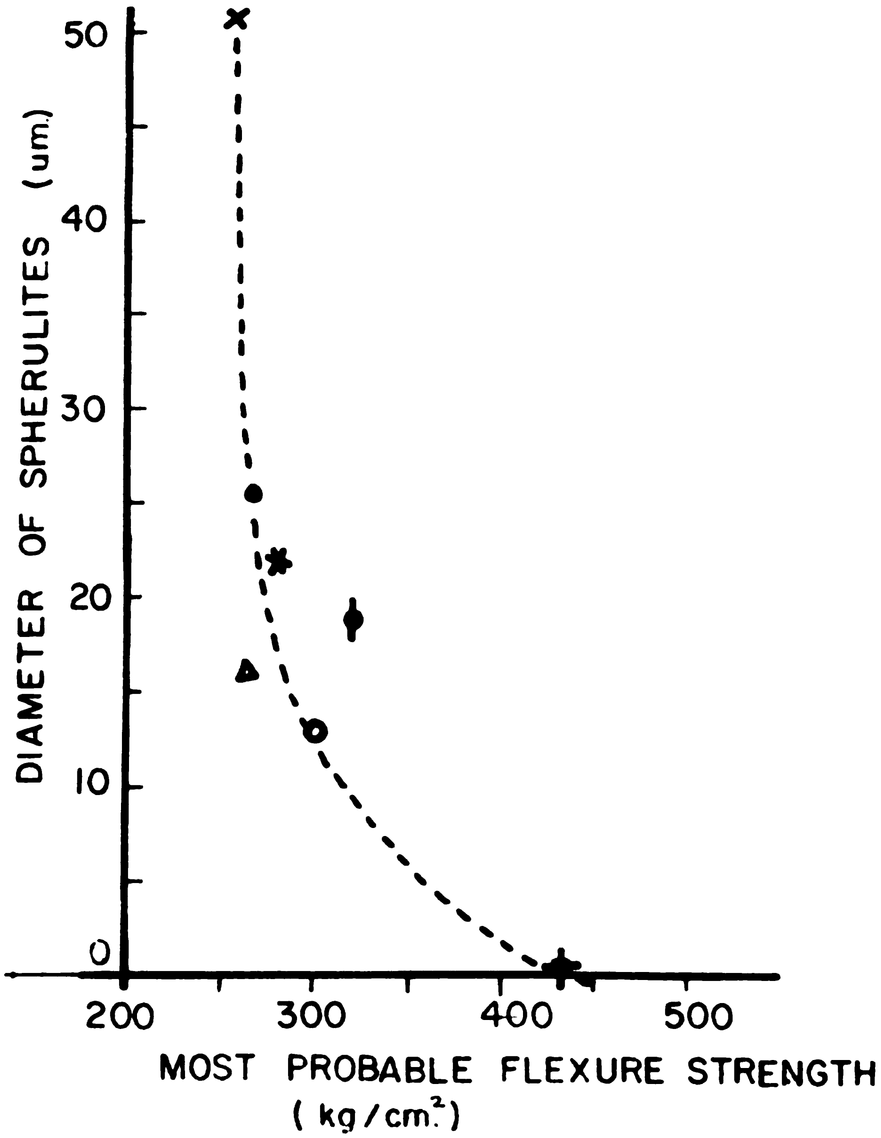
DIAMETER OF SPHERULITES (um.)
50
40
30
20
10
0
200
300
400
500
MOST PROBABLE FLEXURE STRENGTH
(kg/cm^2)

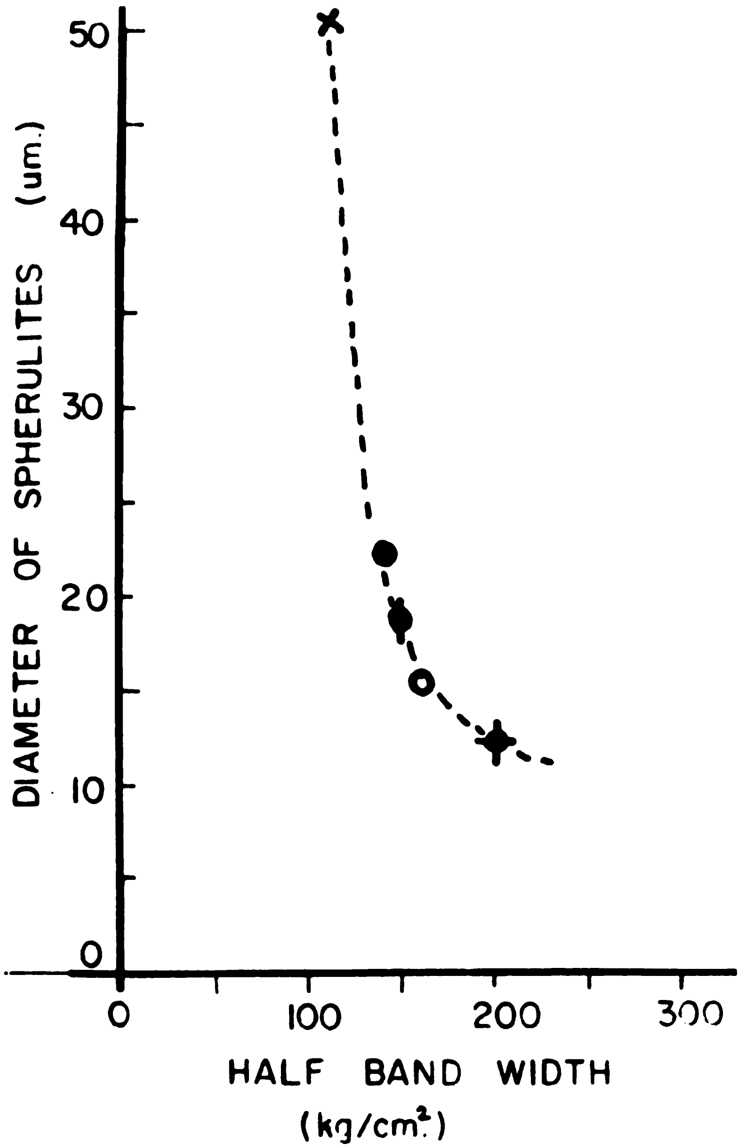
DIAMETER OF SPHERULITES (um.)
50
40
30
20
10
0
0
100
200
300
HALF BAND WIDTH
(kg/cm^2)

Fig. 53. Plot of frequency of fracture as a function of flexure strength of amorphous and partially crystallized selenium (for constant volume fraction of spherulites).

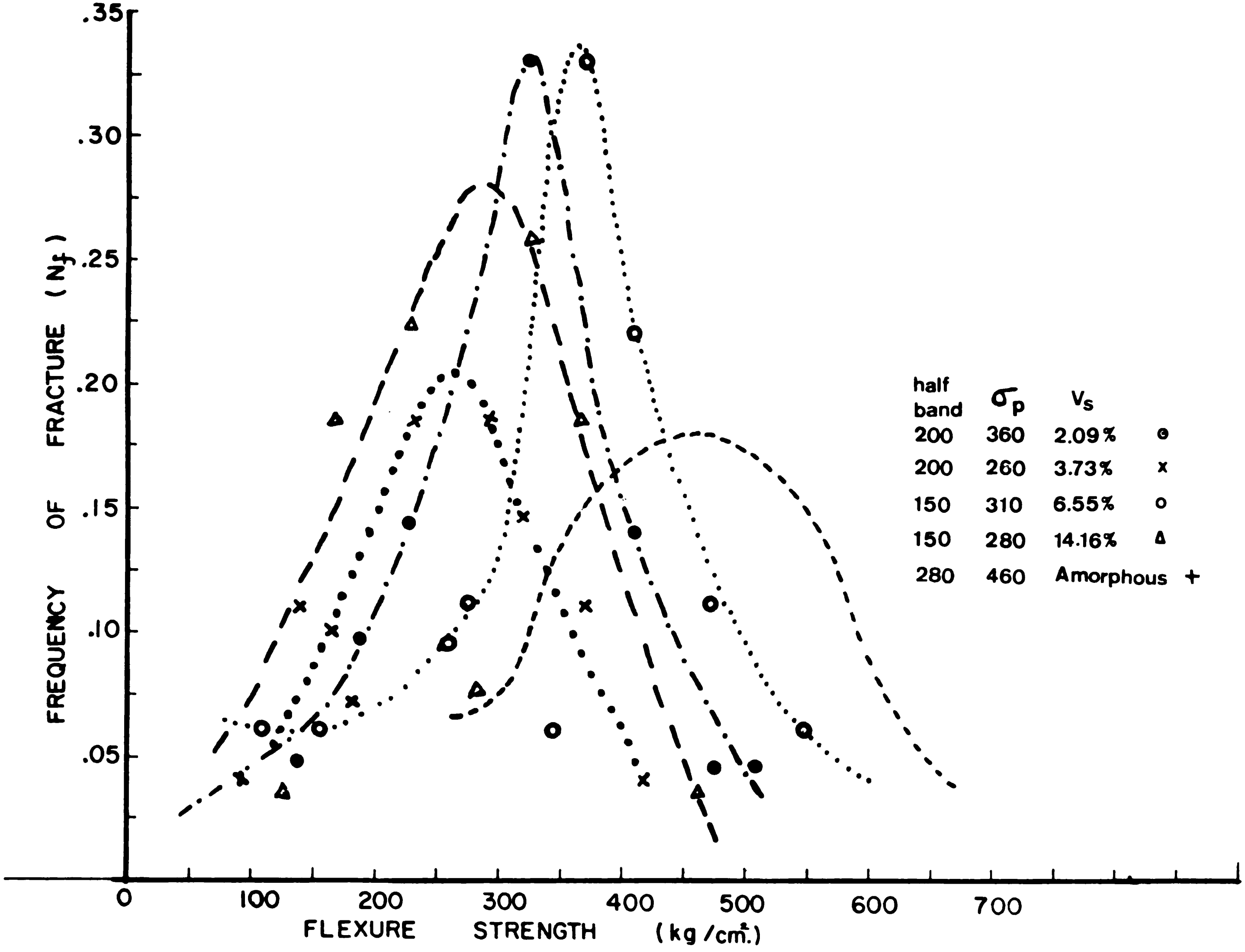
.35
.30
.25
.20
.15
.10
.05
FREQUENCY OF FRACTURE (N_f)
0
100
200
300
400
500
600
700
FLEXURE STRENGTH (kg/cm²)
half band
σ_p
V_s
200 360 2.09% ⊙
200 260 3.73% x
150 310 6.55% o
150 280 14.16% Δ
280 460 Amorphous +

Fig. 54. Plot of half band width of Weibull's curves of Figure 53, as a function of volume fraction of spherulites.

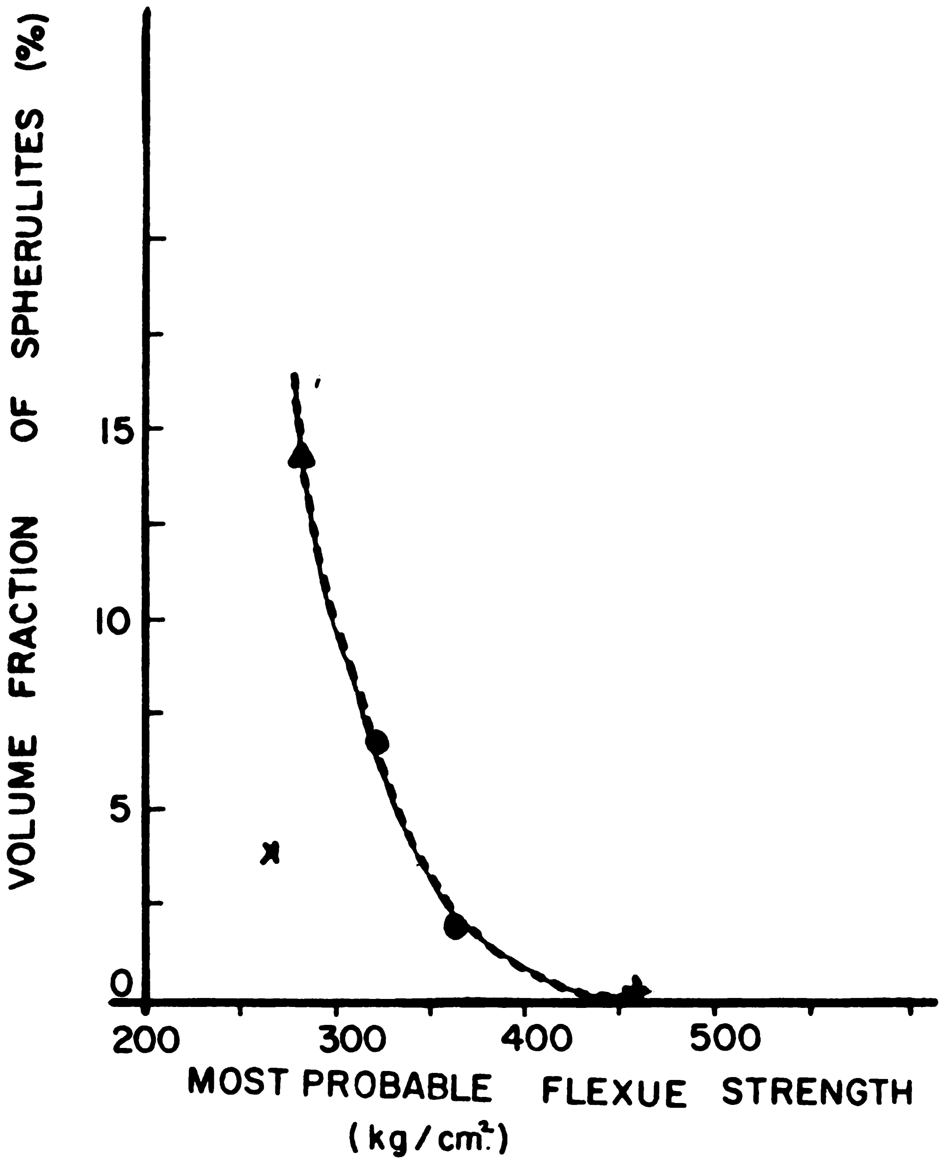
VOLUME FRACTION OF SPHERULITES (%)
15
10
5
0
200
300
400
500
MOST PROBABLE FLEXUE STRENGTH
(kg/cm^2)

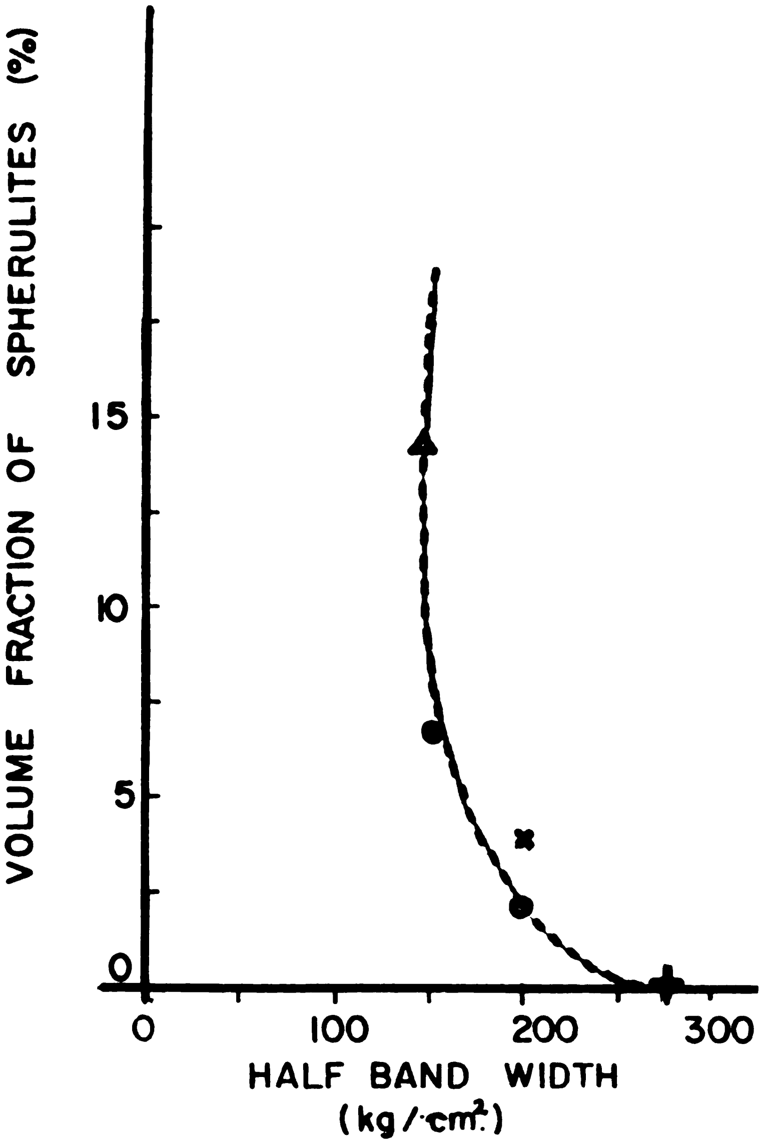
VOLUME FRACTION OF SPHERULITES (%)
15
10
5
0
0
100
200
300
HALF BAND WIDTH
(kg/cm^2)

half band width of each Weibull's curve is plotted as a function of increasing volume fraction of spherulites. It is seen from Figure 54 that the half band width or scatter of flexure strength decreases. It is possible to consider the half band width of the Weibull's curve to be an indication of the homogeneity (m) of the specimens.

4.4 Fracture Analysis of Partially Crystallized Selenium

In this section, an attempt is made to determine the flexure strength of partially crystallized selenium from the dimensions of the mirror area of fracture by Shand's approach[55].

4.4.1 Flexure Strength of Amorphous Selenium as Determined from the Dimensions of Fracture Mirrors

In Section 2.5.2 the theoretical basis of this work has already been stated. Experimental tests by Shand[55], Smekal[58] and Terao[59] have shown that a relation exists between the dimensions of the mirrored section of a glass fracture and the nominal stress causing the fracture. In Shand's work, for a fracture crack with a depth or radius r in a section of a circular rod of diameter D (see sketch, Figure 8), the stress concentration at the crack tip may be written as

$$k = f(D,r)/(\rho)^{\frac{1}{2}} \qquad [24]$$

The nominal breaking stress is the critical stress of the glass divided by the stress-concentration factor of a crack with dimensions of the mirror surface. The nominal breaking stress can be written as follows:

$$\sigma_a = \sigma_m/k = \sigma_m(\rho)^{\frac{1}{2}}/f(D,r) \qquad [25]$$

where σ_a = nominal breaking stress,

σ_m = critical breaking stress,

ρ = crack-tip radius,

k = stress-concentration factor, and

$f(D,r)$ = function determined by the dimensions of fracture.

This stress-concentration factor is determined by the size and geometrical form of the exposed surface of the fracture crack and also by certain characteristic deformations which occur at the crack tip, i.e., at the boundary where separation of the material takes place. It is assumed that these deformations can be represented by a crack-tip radius ρ, which is treated as an unknown. Griffith[21] adopted this assumption, which was later justified by Elliott[23]. Orowan[18,69] has shown that the critical dimensions of the fracture increase when deformations at the crack-tip involve plastic flaw. In the case of glassy materials, the effect of plastic flaw on the mirror radius can be considered negligible, whereas in the glass-crystalline composites the effect could affect the mirror radius considerably.

Shand[55] has used Nueber's method for computing the function f(D,r). For the present case, k_a and k_b are the stress-concentration factors, as shown in Figure 55, for two opposing notches in a strip of finite width; the resultant stress factor 'k' has been expressed by Shand as follows:

$$\frac{1}{k^2} = \frac{1}{k_a^2} + \frac{1}{k_b^2}$$

or

$$k = \frac{k_a k_b}{\sqrt{k_a^2 + k_b^2}} \qquad [26]$$

Fig. 55. Stress-concentration factor k_a and k_b. All loads applied in tension (Shand[55]).

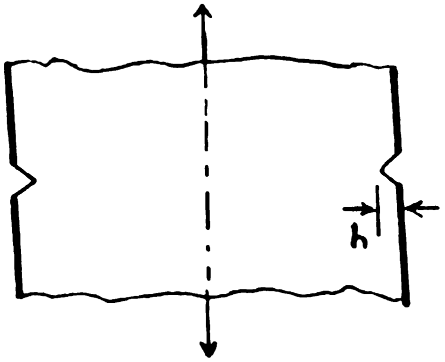

$$k_a(\rho)^{1/2} = 1.27(r)^{1/2}$$

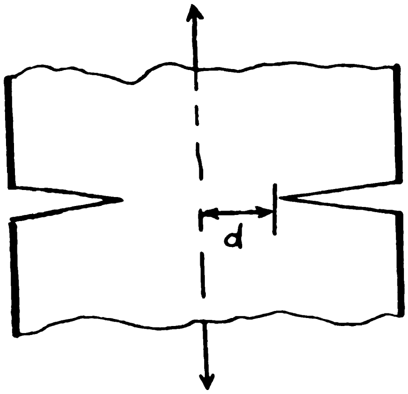

$$k_b(\rho)^{1/2} = (D-r)^{1/2}$$

k_a --- is the stress-concentration factor for two opposing notches in two edges of a wide plate under tension.

k_b --- is the stress-concentration factor for two opposing notches in a wide plate extending to a depth which leaves only a narrow section between them.

For two opposing notches in a strip of finite width, the resultant stress factor, k, is given by:

$$k = \frac{k_a\, k_b}{\sqrt{k_a^2 + k_b^2}}$$

He took

$$\left.\begin{aligned} k_a\sqrt{\rho} &= 1.27\sqrt{r} \\ k_b\sqrt{\rho} &= \sqrt{D-r} \end{aligned}\right\} \qquad [27]$$

Substituting Equation 27 in Equation 26,

$$k(\rho)^{\frac{1}{2}} = f(D,r) = \frac{1.27\sqrt{r}\sqrt{D-r}}{1.27^2 r + \sqrt{(D-r)}} \quad .$$

Values of $f(D,r)$ computed by Shand for a rod 0.457 in. in diameter are shown as a function of crack depth or mirror radius in Figure 59. $\sigma_m(\rho)^{\frac{1}{2}}$ of Equation 25 can be determined from experimental data.

$$\sigma_m(\rho)^{\frac{1}{2}} = \sigma_a f(D,r) \quad .$$

σ_m and $(\rho)^{\frac{1}{2}}$ cannot be measured experimentally.

The values of $f(D,r)$ were determined from mirror radius (r), and the depth of the specimen (D) for one melt by Equation 9. The value of $f(D,r)$ for this melt has been plotted as a function of mirror radius in Figure 56. The mirror radius (r) evaluated for the remaining melts, and the $f(D,r)$ value found from Figure 56 and substituted in Equations 9 and 10, would give the breaking stress of the specimen. The stress determined by this method for each specimen is plotted as a function of mirror radius (r) as shown in Figure 57.

For any given mirror radius, a corresponding value of $f(D,r)$ can be determined from Figure 56. The nominal breaking stress or flexure strength of the glass can then be determined from Equation 25.

Flexure strength of glassy selenium was determined with bar specimens, as reported in Section 3.3.1. The results are summarized in Table 6.

Fig. 56. Plot of the function f(D,r) versus mirror radius for amorphous and partially crystallized selenium.

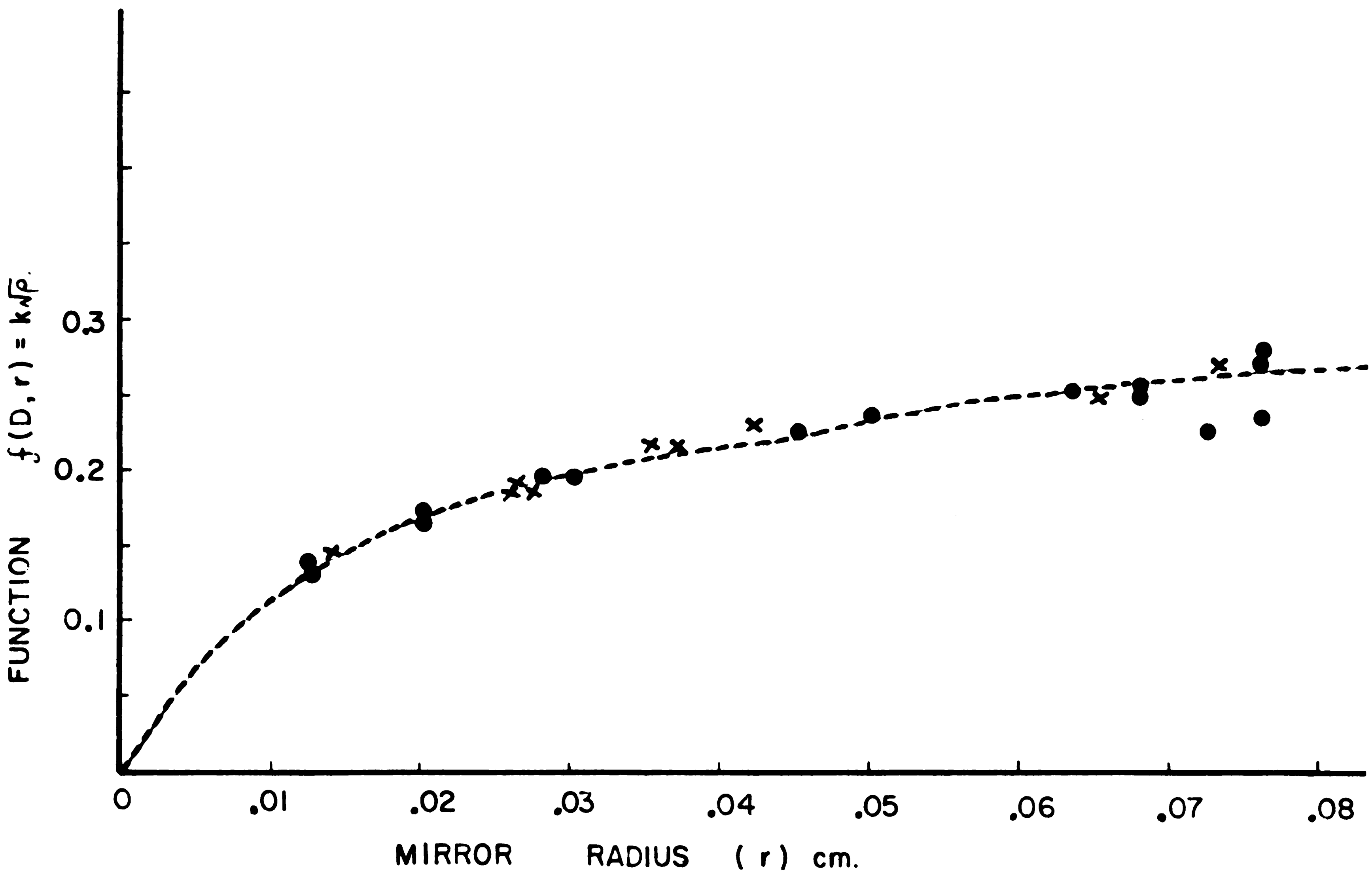
FUNCTION $f(D, r) = k\sqrt{\rho}$
0.3
0.2
0.1
0
.01
.02
.03
.04
.05
.06
.07
.08
MIRROR RADIUS (r) cm.

Fig. 57. Plot of the breaking stress as a function of mirror radius for amorphous selenium.

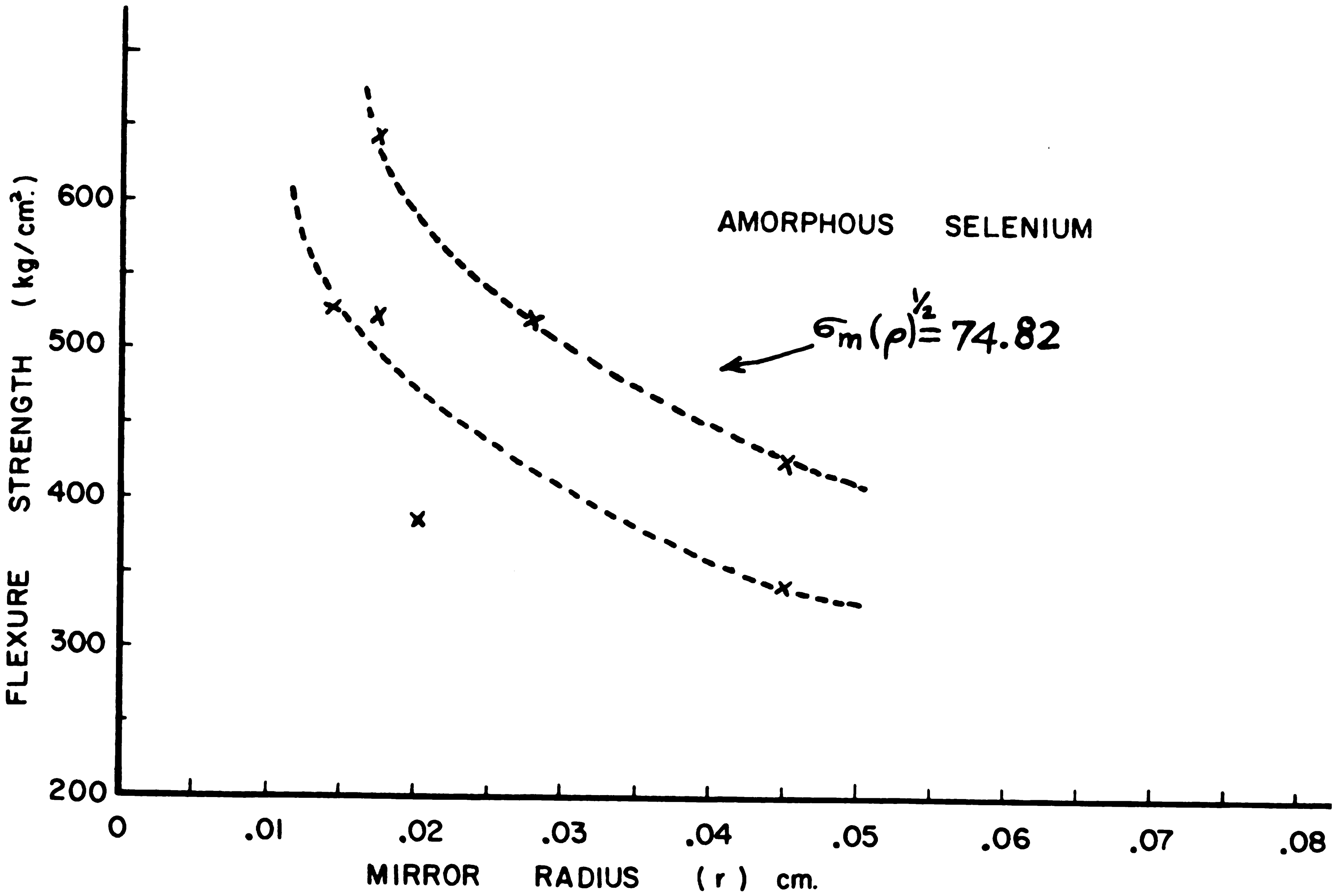
AMORPHOUS SELENIUM
$\sigma_m(\rho)^{1/2} = 74.82$
FLEXURE STRENGTH (kg/cm².)
200
300
400
500
600
0
.01
.02
.03
.04
.05
.06
.07
.08
MIRROR RADIUS (r) cm.

The function f(D,r) was calculated from mirror radius 'r' and the depth of the bar as 'D'. The plot of function f(D,r) versus mirror radius 'r' is shown in Figure 56. Shand's plot for f(D,r) for borosilicate glass (Corning No. 7740) is shown in Figure 59 to demonstrate that the two curves are similar.

The flexure strength is plotted as a function of mirror radius in Figure 57. As expected, the value of $\sigma_m(\rho)^{\frac{1}{2}} = 75.00$ is a constant for all specimens, as seen from Table 13. The breaking strength has a maximum value 600 kg/cm^2 for a mirror radius 0.015 cm. The breaking strength decreases non-linearly, and tends to become constant at 400 kg/cm^2 for a mirror radius 0.04 cm. The important point noted from this test is that the breaking strength is highest for amorphous material, and that such specimens show a small mirror radius. With increase of mirror radius, the breaking strength decreases to a minimum value of 400 kg/cm^2. The reason for the decrease of strength from 600 to 400 kg/cm^2 is definitely due to the scatter of strength value that exists in glassy materials. The discontinuity in materials and the surface conditions of specimens do produce considerable scatter. Another reason for the flexure strength to have the above-mentioned range is the possibility of having a residual stress produced by a small cord or other inhomogeneities in the specimens.

The actual flexure strength determined by bend test is compared with the flexure strength determined from the dimensions of fracture mirror. The ± 10% error noted may be due to inhomogeneities and locked-in residual stresses in amorphous selenium specimens. In the case of amorphous specimens, the dimensions of the mirror were very small in relation to those of the section of the specimen (about 3 to 6%

TABLE 13

Mirror Radius, Function f(D,r), Breaking Stress and $\sigma_m(\rho)^{\frac{1}{2}}$ Values for Amorphous Selenium Specimens

HEAT TREATMENT		MIRROR RADIUS (cm)	FUNCTION f(D,r)	BREAKING STRESS (kg/cm^2)	$\sigma_m(\rho)^{\frac{1}{2}}$
AMORPHOUS SELENIUM					
MELT B	S-1	.0279	.2009	520.35	104.56
	S-2	.0127	.1392	345.37	48.09
	S-2	.0127	.1394	378.11	52.74
	S-2	.0457	.2471	345.37	85.35
	S-3	.0762	.2977	266.76	79.40
	S-3	.0203	.2977	374.06	64.97
MELT C	S-1	.0127	.1392	353.07	49.14
	S-1	.0140	.1455	523.84	76.22
	S-2	.0457	.2364	428.29	101.27
	S-2	.0508	.2464	186.99	46.07
	S-3	.0178	.1618	522.60	84.55
	S-3	.0178	.1619	651.45	105.51

of the depth of the specimen). Since the fracture crack is very small, the applied force does not get relaxed in this case. Hence the error due to load relaxation phenomenon does not affect the results.

4.4.2 Flexure Strength of Partially Crystallized Selenium as Determined by the Dimensions of Fracture Mirrors

Flexure strength of partially crystallized selenium is tabulated in Table 6. The results of mirror-area studies have been summarized in Table 14. The mirror area of specimens are shown in Figure 60. The mirror area for different specimens having volume fractions of spherulitic selenium varying from 2.09 to 8.13% is given in Figure 58. The function f(D,r) is calculated and listed in Table 14. The plot of f(D,r) as a function of mirror radius is shown in Figure 56. The mean value of $\sigma_m(\rho)^{\frac{1}{2}}$ equals 70.00 for partially crystallized selenium specimens having volume fractions of spherulites between 2.09 and 3.73%. For increased volume fractions of spherulites, i.e., between 6.55 and 14.16%, the mean value of $\sigma_m(\rho)^{\frac{1}{2}}$ equals 66.00, as seen in Table 14. The breaking strength has a maximum value 450 kg/cm^2 for a mirror radius 0.012 cm. The breaking strength decreases non-linearly and tends to decrease sharply in case of low volume fractions, as seen in the curves for volume fractions $V_s = 6.55\%$ and $V_s = 14.16\%$. There are no significant changes in the trends of the curves, as can be seen from Figure 58. The relation between mirror radius and nominal breaking stress, as determined for the point of fracture for varying volume fractions of spherulitic selenium, does not change. Plots of breaking strength versus mirror radius for (a) amorphous selenium, (b) partially crystallized selenium, (c) Glass No. 7740 (from Shand[55]), and (d) Glass Ceramics No. 9606 (from Shand[55]), show similar trends. Amorphous selenium is stronger and has a larger value of $\sigma_m(\rho)^{\frac{1}{2}} = 75.00$ compared with

TABLE 14

Mirror Radius, Function f(D,r), Breaking Stress and $\sigma_m(\rho)^{\frac{1}{2}}$ Values for Partially Crystallized Selenium Specimens

HEAT TREATMENT				MIRROR RADIUS (cm)	FUNCTION f(D,r)	BREAKING STRESS (kg/cm^2)	$\sigma_m(\rho)^{\frac{1}{2}}$
V_s = 2.09%							
MELT A	62°C	200 hr	S-2	.0127	.1376	292.33	40.00
	62°C	250 hr	S-4	.0254	.1871	283.10	52.98
			S-5	.0254	.1884	382.28	66.87
			S-6	.0254	.1859	257.56	66.72
MELT B	62°C	250 hr	S-4	.0381	.2190	304.72	57.85
			S-5	.0140	.1448	450.79	71.20
			S-6	.0356	.2164	384.07	83.12
MELT C	62°C	200 hr	S-1	.02667	.1938	438.17	79.76
			S-2	.0279	.1972	380.58	70.03
			S-3	.0423	.2344	328.76	69.90
V_s = 3.73%							
MELT A	62°C	311 hr	S-7	.0279	.1950	254.66	33.95
MELT B	62°C	311 hr	S-7	.0635	.2737	213.38	62.76
			S-8	.0457	.2330	305.10	71.09
MELT C	62°C	250 hr	S-4	.0457	.2223	203.13	57.247
			S-5	.0724	.2628	347.54	82.28
			S-6	.0762	.2779	313.08	86.93
MELT A	82°C	4 hr	S-1	.0203	.1727	455.79	78.74
			S-2	.0413	.2255	351.53	83.80
			S-3	.0330	.2116	362.83	65.59
MELT B	100°C	45 min	S-1	.0152	.1486	360.10	63.24
			S-2	.0279	.1974	289.61	67.22
			S-3	.0381	.2193	267.75	58.47
V_s = 6.55%							
MELT A	82°C	6 hr	S-4	.0267	.1951	325.17	47.01
			S-6	.0203	.1710	358.74	53.71

TABLE 14 (Continued)

MELT B	82°C	4 hr	S-1	.0406	.2276	252.65	57.50
			S-2	.0406	.2313	386.04	62.57
			S-3	.0178	.1595	321.24	49.51
MELT C	82°C	4 hr	S-1	.0127	.1381	501.54	69.26
			S-2	.0127	.1369	407.35	64.60
MELT C	62°C	311 hr	S-7	.1016	.2596	225.25	64.58
			S-8	.0508	.2432	232.67	60.52
			S-9	.0762	.2661	181.97	63.11
V_s = 8.13%							
MELT A	100°C	45 min	S-1	.0381	.2201	244.31	53.76
			S-3	.0508	.2361	295.62	78.38
MELT B	82°C	6 hr	S-5	.0318	.2055	360.60	64.96
			S-6	.0381	.2141	386.38	73.13
MELT C	100°C	45 min	S-1	.0762	.2399	278.24	59.54
			S-2	.0127	.1355	399.92	68.21
			S-3	.0762	.2595	242.07	69.17
V_s = 14.16%							
MELT A	82°C	8 hr	S-7	.0203	.1723	245.26	41.97
			S-8	.0254	.1871	298.35	53.19
			S-9	.0254	.1839	190.49	41.83
MELT B	100°C	1 hr	S-4	.0178	.1616	350.74	56.67
			S-5	.0508	.2395	352.74	76.82
			S-6	.0445	.2281	306.01	69.80
MELT B	82°C	8 hr	S-7	.03683	.2130	331.64	70.46
			S-8	.0311	.1977	350.66	71.45
			S-9	.0318	.2028	199.11	61.29
MELT C	100°C	1 hr	S-4	.0203	.1666	245.64	57.16
			S-5	.0203	.1703	275.09	59.41
MELT C	82°C	6 hr	S-4	.0762	.2803	246.24	67.942
			S-5	.0762	.2755	292.72	73.64
			S-6	.0762	.2790	336.30	70.55

Fig. 58. Plot of the breaking stress as a function of mirror radius for partially crystallized selenium.

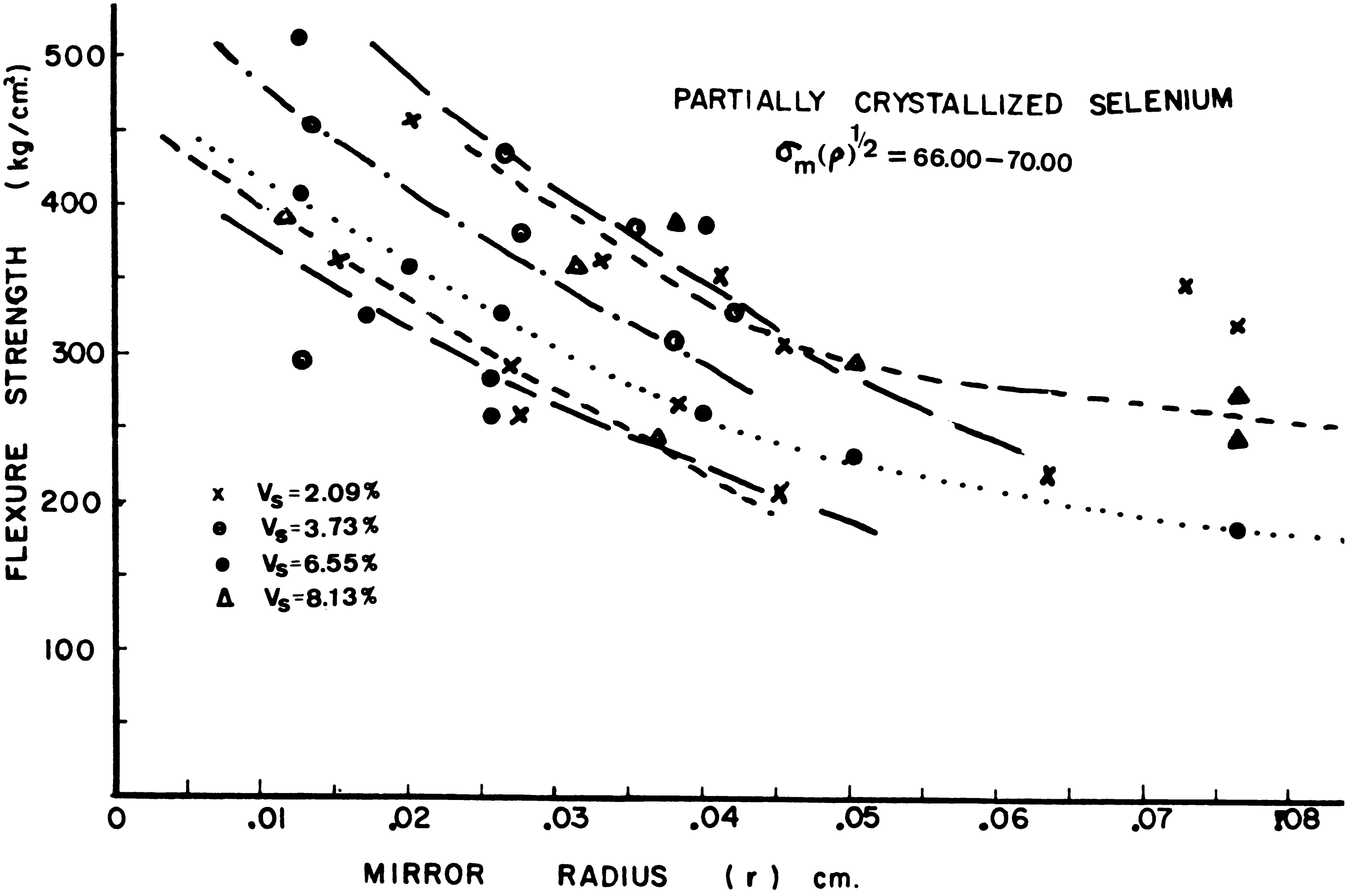
PARTIALLY CRYSTALLIZED SELENIUM
$\sigma_m(\rho)^{1/2} = 66.00-70.00$
FLEXURE STRENGTH (kg/cm^2)
500
400
300
200
100
0
.01
.02
.03
.04
.05
.06
.07
.08
MIRROR RADIUS (r) cm.
× $V_s = 2.09\%$
⊙ $V_s = 3.73\%$
● $V_s = 6.55\%$
Δ $V_s = 8.13\%$

Fig. 59. Plot of function f(D,r) versus mirror radius for small fracture cracks, with the addition of curve corrected for flexure conditions (Shand[55]).

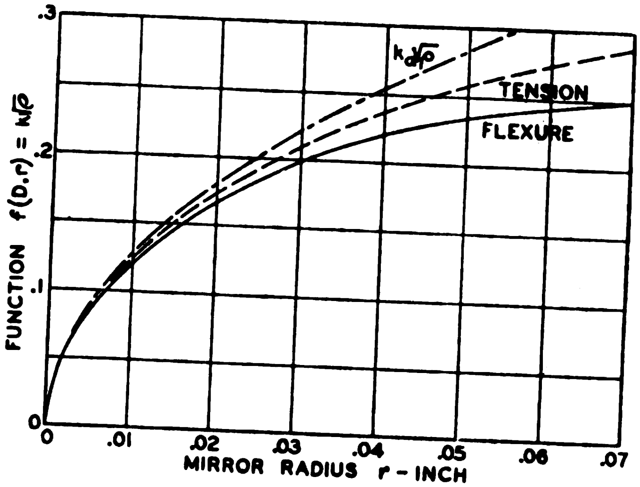
.3
.2
.1
0
FUNCTION $f(D,r) = k\sqrt{\rho}$
$k_d\sqrt{\rho}$
TENSION
FLEXURE
0
.01
.02
.03
.04
.05
.06
.07
MIRROR RADIUS r - INCH

Fig. 60. Mirror areas of partially crystallized selenium.
(A) Specimens heat-treated at 62°C for 200 hr, 250 hr, and 311 hr (70x).
(B) Specimens heat-treated at 82°C for 4 hr, 6 hr, and 8 hr (70x).
(C) Specimens heat-treated at 100°C for 45 min, 1 hr, and 1½ hr (70x).

A

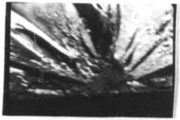
62°C, 200 hr.


62°C, 250 hr.

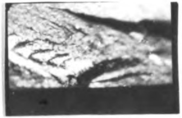
62°C, 311 hr.

B

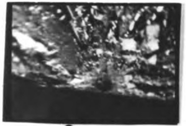
82°C, 4 hr.

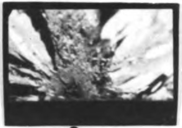
82°C, 6 hr.


82°C, 8 hr.

C


100°C, 45 min.

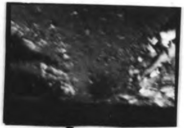
100°C, 1 hr.

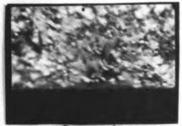
100°C, 1 1/2 hr.

Fig. 61. Plot of $\sigma_m(\rho)^{\frac{1}{2}}$ values as a function of volume fraction of crystallites of selenium.

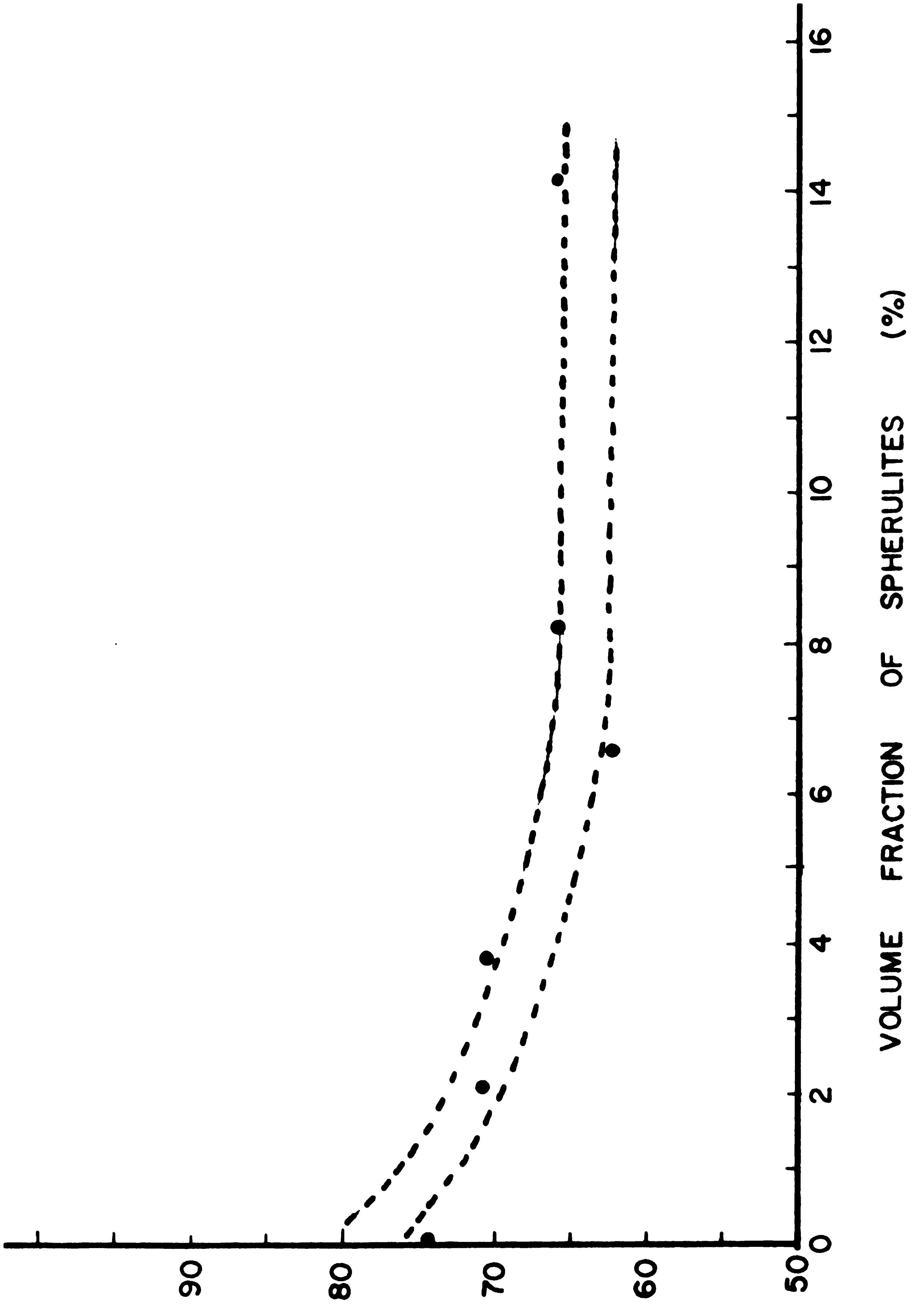

σm/ρ →
90
80
70
60
50
0
2
4
6
8
10
12
14
16
VOLUME FRACTION OF SPHERULITES (%)

the partially crystallized selenium specimens. The flexure strength of the crystallized specimens is lower than that of the amorphous specimens, and they have a lower value of $\sigma_m(\rho)^{\frac{1}{2}} = 66$ to 70. In Figure 61, the values of $\sigma_m(\rho)^{\frac{1}{2}}$ are plotted as a function of volume fraction of spherulites. The curve indicates that the amorphous selenium has the highest value of $\sigma_m(\rho)^{\frac{1}{2}}$ and, with increase of crystalline phase in the amorphous matrix, the value of $\sigma_m(\rho)^{\frac{1}{2}}$ decreases non-linearly. The specimens with 45 to 50% crystallinity do not show any mirror area. With increased volume fraction of crystallites, the strength decreases and the mirror radius increases to large values. As a result, no mirror area is formed. From results shown in Table 14 it can be seen that specimens having greater than 14% volume fraction of spherulites do not possess mirror areas.

The actual flexure strength determined by bend test is compared with the flexure strength determined from the dimensions of fracture mirror. The ± 10% error noted may be due to the following factors:

a) the partially crystallized selenium specimens may not possibly be free from residual stress, because of the complex stresses introduced owing to the crystalline phase.

b) the mirror dimension increases with increase of volume fraction of the crystalline phase. Shand[55] has noted that the relaxation of the applied force occurs when the fracture of the crack becomes large. For the bending tests, the limiting dimensions of the mirror radius was taken as 15% of the diameter of the specimen. In the present work, the ratio (r/D) varies from 5 to 20%, and hence the error due to relaxation of applied force does affect the flexure strength calculated from the mirror radius. The loading rate was so selected to make the time of test as short as possible (15-30 seconds in the present work). The rate of loading minimizes the error created owing to relaxation of breaking load resulting from large fracture crack.

c) the partially-crystallized selenium specimen may not record the extent of mirror region, sharply owing to the presence of different size and volume fractions of crystalline phase in the glassy matrix. This factor may introduce a large margin of error, as compared with the results of the amorphous selenium specimens.

4.5 Comparison of Flexure Strength and Elastic Modulus of Amorphous Selenium and Partially Crystallized Selenium with Glassy Materials and Glass-Crystalline Materials

Desirable physical properties not provided by single-phase materials often can be conveniently attained by multiphase composites. For example, oxide glasses can be strengthened by the introduction of spherical crystalline inclusions[63]. Unlike this case, the introduction of spherulites in the glassy selenium matrix decreases its flexure strength. The elastic modulus of glassy selenium, as in the case of oxide glasses, increases with the introduction of the spherical crystalline phase.

4.5.1 Comparison of Flexure Strength and Elastic Modulus of Amorphous Selenium with Oxide Glasses

In Table 15, the flexure strength and elastic modulus of a number of oxide glasses are presented from the work of Davidge and Tappin[62] and from Frey and Mackenzie[63]. The flexure strength and the elastic modulus of linear-chain-structured amorphous selenium as determined in this

TABLE 15

Flexure Strength and Elastic Modulus of Certain Glasses

MATERIAL	FLEXURE STRENGTH (kg/cm^2)	ELASTIC MODULUS (kg/cm^2)
Glass (soda-lime type)		0.71×10^6
Glass I (6810) (soda-zinc type)	504	0.658×10^6
Glass II (7740) (borosilicate type)	490	0.637×10^6
Glass III (1990) (potash-soda-lead type)	441	0.588×10^6
PMMA (ICI Perspex sheet)		0.0308×10^6
Amorphous Selenium	480 to 520	$.07$ to 0.10×10^6

investigation are exactly the same range of some of the network-structured oxide glasses, such as soda-lime, soda-zinc (glass I), borosilicate (glass II), and potash-soda-lead glasses (glass III).

4.5.2 Comparison of Flexure Strength and Elastic Modulus of Partially Crystallized Selenium with Glass-Ceramics and Glass-Crystal Composites

An interesting comparison can be made with the results of the present investigation and those of Frey and Mackenzie[62], who worked with glass-Al_2O_3 and glass-ZrO_2 composites. Table 15 lists the pertinent physical properties of all glasses and the crystalline phases studied. The size of spherical inclusions varied from 125 to 150μm, and volume of the crystalline phase varied from 20 to 40 volume %. In the present work, the size of spherulites of selenium varied from 12.75 to 50.8μm, and the volume fraction of crystallites varied from 0 to 50 volume %. It is worth noting in Figure 62, reproduced from Frey and Mackenzie[62], that both glass I and glass II were strengthened by the Al_2O_3 inclusions even though internal stresses of considerable magnitude were present. In the tangential direction of these inclusions, a tensile stress will develop, since $\Delta\alpha$ is positive but small. Glass III is a typical example where $\Delta\alpha$ is very large and α_p positive, where α_p is the thermal expansion coefficient of the crystalline phase, α_m is the thermal expansion coefficient of the glassy phase, and $\Delta\alpha = (\alpha_p - \alpha_m)$. The large value of $\Delta\alpha$ results in a large tensile stress in the tengential direction at the glass-crystal interface. As a result, the flexure strength tends to decrease up to 20 volume percent of crystalline phase, and then increases. The lack of strengthening in this composite series is attributed to the cracks present in the glassy matrix

TABLE 16

Pertinent Physical Properties of Certain Oxide Glasses and Crystalline Phases

	GLASS I 6810	GLASS II 7740	GLASS III 1990	Al_2O_3	ZrO_2	Amorphous Selenium	Hexagonal Selenium
Density (g/cm^3)	2.65	2.23	3.47	3.91	5.65	4.3	4.81
Strain Point (°C)	490	515	330				
Softening Point (°C)	770	820	500			40-50	
Melting Point (°C)				2000	2550	217	217
Elastic Modulus E(10^6 kg/cm^2)	0.658	0.637	.588	3.85	1.42	0.07	0.588
Linear Coefficient of Thermal Expansion (°C x 10^{-6})	6.9	3.3	12.4	5.47	8.85	37.73	37.79

Fig. 62. Plot of flexure strength versus volume fraction of crystallites (Frey and Mackenzie[62]).

Fig. 63. Plot of elastic modulus versus volume fraction of crystallites (Frey and Mackenzie[62]).

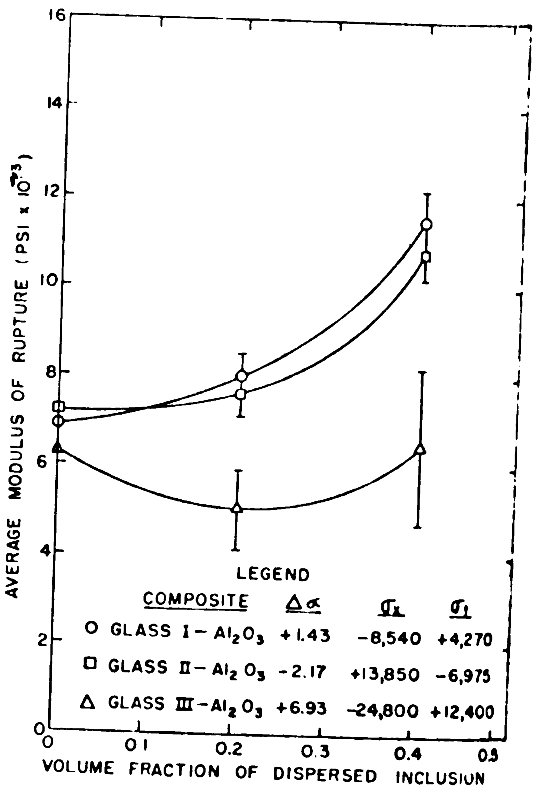
16
14
12
10
8
6
4
2
0
AVERAGE MODULUS OF RUPTURE (PSI x 10^{-3})
0
0.1
0.2
0.3
0.4
0.5
VOLUME FRACTION OF DISPERSED INCLUSION
LEGEND
COMPOSITE $\Delta\alpha$ σ_r σ_t
○ GLASS I – Al_2O_3 +1.43 -8,540 +4,270
□ GLASS II – Al_2O_3 -2.17 +13,850 -6,975
△ GLASS III – Al_2O_3 +6.93 -24,800 +12,400

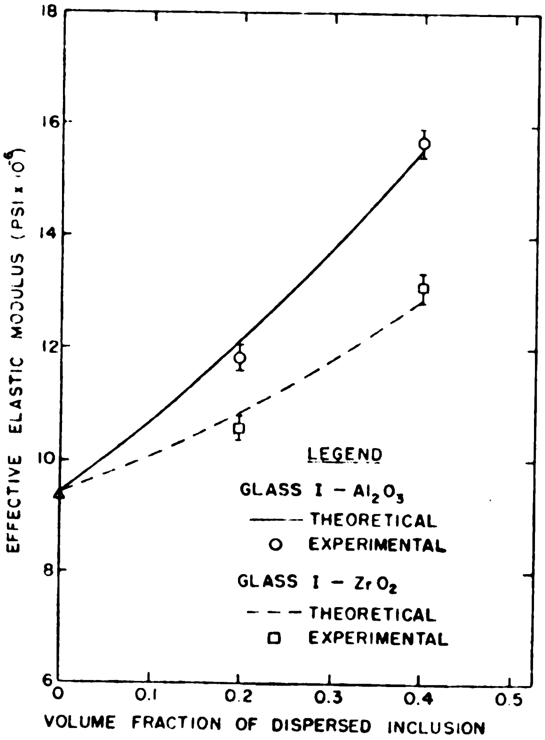
18
16
14
12
10
8
6
EFFECTIVE ELASTIC MODULUS (PSI x 10^{-6})
0
0.1
0.2
0.3
0.4
0.5
VOLUME FRACTION OF DISPERSED INCLUSION
LEGEND
GLASS I – Al_2O_3
—— THEORETICAL
○ EXPERIMENTAL
GLASS I – ZrO_2
– – – THEORETICAL
□ EXPERIMENTAL

before flexure-strength tests were performed. In the case of glass I, there was tensile stress in the tangential direction, but it did not cause premature cracking in the glassy matrix; thus the flexure strength was unaffected. Hence, internal stresses were found to reduce flexure strength only if they were large enough to cause premature fracture of the glassy matrix.

In the case of partially crystallized selenium, the microstructure shows no premature fracture in the glassy matrix for volume fraction of crystalline phase varying from 0 to 50%. The linear thermal-expansion coefficient (α_p) for trigonal selenium is slightly higher than that for amorphous selenium. The spherulites of selenium, because of the internal arrangements of the trigonal selenium lamellas, show a mechanically weak peripheral region, where invariably the fracture originates. The tangential direction would have a tensile stress, and would tend to produce initially radial paths of fracture. The flexure strength of partially crystallized selenium decreases with increase of volume fraction of crystallites. This decrease can be explained by the same reasoning used to explain the behavior of the oxide glasses containing crystalline inclusions having higher expansion coefficient. The only difference in the present system is that the crystalline phase is weaker instead of the glassy phase.

In Figure 63 the elastic modulus of glass-Al_2O_3 and glass-ZrO_2 has been plotted as a function of volume fraction of crystalline phase. The plot of elastic modulus of partially crystallized selenium versus volume fraction of crystallites is shown in Figure 29. The trend of the elastic-modulus curve for partially crystallized selenium is similar to that for oxide glasses containing crystalline inclusions. For low volume fraction (less than 10%) and small size of crystals, the elastic modulus varies linearly and rises sharply. A similar comparison cannot be made in glass-crystal composites since no results exist for this size and volume fraction of crystals. However, the elastic-modulus curve of partially crystallized selenium containing larger-size crystals (50.8μm) with volume fractions greater than 10% is similar to that of glass-Al_2O_3 composite.

The results of the present investigation can be compared with results of Hasselman and Fulrath[45], and of Bertolotti and Fulrath[70]. Hasselman and Fulrath[45] plot flexure strength of glass-Al_2O_3 and glass-pore composites, as shown in Figures 64(A) and (B). Bertolotti and Fulrath[70] plot flexure strength of glass-pore composite, as shown in Figure 64(C). The variation of flexure strength of partially crystallized selenium as a function of volume fraction of crystals (Figure 23) agrees with the plot of Bertolotti and Fulrath[70] of flexure strength versus volume fraction of pores (pore size varying from 20 to 186μm). The reduction in flexure strength with increasing volume fraction of pores (60μm) in Figure 64(B) has been explained by Hasselman and Fulrath[45], as attributable to the stress concentration developed around the pores. Flexure strength of glass-pore composites

(A) decreases severely when pore size (p) is much greater than Griffith's flaw size of glass,

(B) is unaffected when pore size (p) is much less than Griffith's flaw size of glass, and

(C) decreases slightly between case (A) and case (B) when pore size (p) is approximately equal to Griffith's flaw size of glass.

In case of partially crystallized selenium specimens, however, the size of Griffith's flaw present in the amorphous region is always much smaller (less or equal to 5μm) than the size of Griffith's flaw in the spherulites (greater or equal to 30μm). Consequently, flexure strength of partially crystallized selenium decreases with increasing volume fraction of crystallites. The decrease of flexure strength of partially crystallized selenium is dependent on the flaw size in the spherulites, which in turn is determined by the size of spherulites.

Pore sizes of 5 to 10μm strengthen the glass, as seen in Figure 64(C). Contrary to this observation, increasing volume fraction of small-size spherulites ($d_s \leq 15.0\mu m$) tend to drastically reduce the flexure strength of partially crystallized selenium. Bertolotti and Fulrath have explained the strengthening of glass by addition of small-size pores (5 to 10μm) to be due to nickel spheres (the agent for creating the pores) not separating out from the glass matrix.

In lithium-aluminosilicate glass-ceramic the flexure strength decreases with increasing volume fraction of crystallite[71]. In this glass-ceramic the crystalline phase has a lower thermal-expansion coefficient compared with that of the residual glassy phase. As a result, the flexure strength decreases with increasing volume fraction of beta-spodumene crystals. In partially crystallized selenium specimens, the crystalline phase can be considered to have thermal-expansion coefficient greater than that of the glassy phase; in this way, flexure strength decreases with increase of volume fraction of crystalline phase.

It has been shown by Phillips[72], Watanabe[73], McMillan[71], and Freiman and Heinch[48], that flexure strength of certain glasses increases with increase of volume fraction of crystalline phases. McMillan found

Fig. 64. Plot of

(A) Uniaxial and biaxial strength of a soda-borosilicate glass containing alumina spheres 60μ in diameter (Hasselman and Fulrath[45]).

(B) Uniaxial strength of a soda-borosilicate glass containing spherical pores 60μ in diameter (Hasselman and Fulrath[45]).

(C) Uniaxial strength of sodium-borosilicate glass containing spherical pores (Bertolotti and Fulrath[70]).

(A)

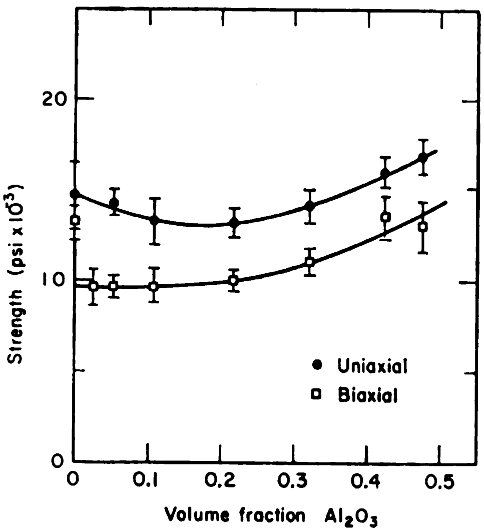
Strength (psi x 10^3)
20
10
0
0
0.1
0.2
0.3
0.4
0.5
Volume fraction Al_2O_3
● Uniaxial
□ Biaxial

(B)

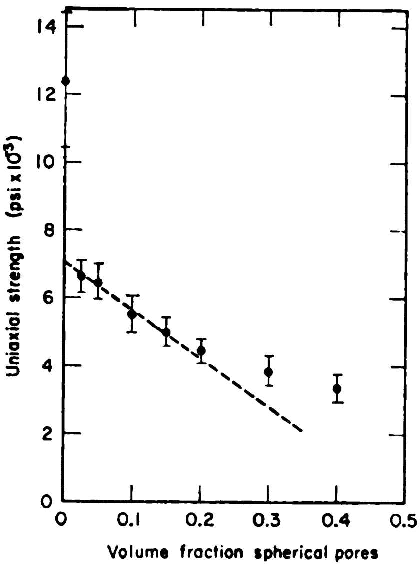
Uniaxial strength (psi x 10^3)
14
12
10
8
6
4
2
0
0
0.1
0.2
0.3
0.4
0.5
Volume fraction spherical pores

(C)

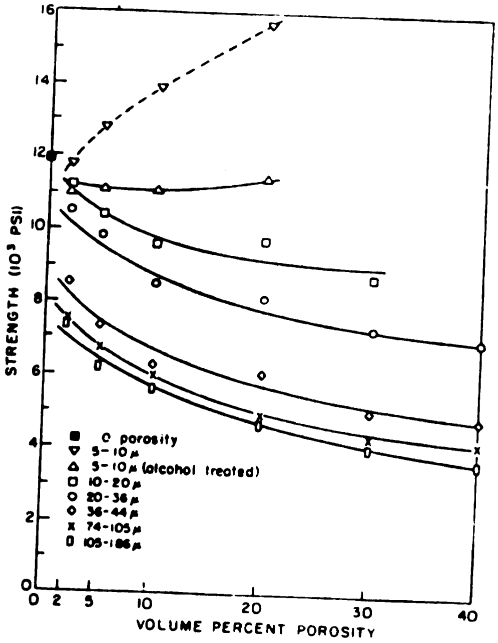
STRENGTH (10^3 PSI)
16
14
12
10
8
6
4
2
0
0
2
5
10
20
30
40
VOLUME PERCENT POROSITY
■ 0 porosity
▽ 5-10 μ
△ 5-10 μ (alcohol treated)
□ 10-20 μ
○ 20-36 μ
◇ 36-44 μ
x 74-105 μ
0 105-186 μ

that Li_2O-ZnO-SiO_2-P_2O_5 type glass showed an increase of strength from 1800 to 3500 kg/cm^2, as a result of heat treatment at 600°C for 1 hour. The differential contraction of crystalline and glass phases causes a favorable system of microstresses to develop in the glass-ceramics. This system results in the increase of flexure strength. Freiman and Hench, working with a series of glass-ceramics developed by heat-treating a glass of molecular percentage composition $(Li_2O)_{.33}(SiO_2)_{.67}$, showed that mechanical strength increases with increasing volume fraction of crystalline phase. The volume fraction of crystals ranged from 0.5 to 0.95, the crystal sizes varied from 4.2 to 61μm. The Griffith flaw size for the glassy phase was 85μm. The strengthening effect is greatest for small-size crystals, because fracture is controlled by the initiation of flaws in the glass phase rather than in the lithium disilicate spherulites.

Although the microstructure of partially crystallized selenium is very similar to that of $(Li_2O)_{.33}(SiO_2)_{.67}$ system, the flexure strength of partially crystallized selenium decreases with increase of volume fraction of spherulites. The spherulite of selenium is the weakest phase in the partially crystallized selenium specimens. Consequently, fracture invariably originates in the spherulites, and the flexure strength of partially crystallized selenium is always lower than that of amorphous selenium.

V. CONCLUSIONS

1. In an elemental glass-former selenium, the spherulites that are produced by heat-treating the glassy selenium weaken the glass-crystal composite. As a consequence, partially crystallized selenium is mechanically weaker than amorphous selenium.

2. The fracture nucleates in the spherulitic region and prefers to propagate through the crystallized regions, indicating that certain regions of spherulite are weaker than the glassy matrix. The peripheral regions of spherulites appear to be mechanically weaker than the core. The fracture originates from microcracks that develop in the peripheral regions of the spherulites.

3. Increase in volume fraction for a given size of spherulites, as well as increase of size for a given volume fraction of spherulites, decreases the mechanical strength of selenium. Increased volume fraction of small size (10-20μm) spherulites drastically decreases the flexural strength of the partially crystallized selenium. Increased volume fraction of large-size spherulites (20-50μm) does not decrease the flexure strength of the composite as drastically as increased volume fractions of small-size crystals.

4. In amorphous selenium, fracture propagates with no preferred direction, as seen in oxide glasses. The fracture in partially crystallized selenium as indicated by fractographs shows the four distinct

regions of fracture (origin, mirror, coarse, and hackle) as seen in glass-ceramics and glass-crystal composites.

5. Fractographs reveal that the mirror area of fracture is small for higher-strength materials. With decrease of flexure strength, the mirror area increases in size. Above a certain volume fraction of spherulites ($V_s > 15\%$), the fracture becomes mixed, and regions of fracture are not clearly identifiable.

6. Elastic modulus of partially crystallized selenium increases with increase of volume fraction of crystallites. For small size of spherulites ($d_s \leq 20\mu m$), the increase of modulus of elasticity is drastic. For larger-size crystals ($d_s \leq 50\mu m$), the increase of elastic modulus with increase of volume fraction of crystallites is not as drastic as that for the small-size crystals. The Maxwell-Eucken relationship best predicts the experimentally-determined elastic modulus of crystallized selenium for the 50.8μm-size crystals.

7. The scatter of flexure-strength data is greatest for amorphous selenium. With increasing volume fraction of crystallites, the scatter is reduced.

8. The following properties of amorphous and partially crystallized selenium have been determined during the course of this work:

   (a) Amorphous Selenium

   Flexure strength (σ): most probable value $450 kg/cm^2$.

   Elastic modulus (E): $0.7 - 1 \times 10^5 kg/cm^2$.

   Fracture surface energy (γ): $1.6289 ergs/cm^2$.

(b) Partially Crystallized Selenium

Flexure strength (σ): 250-400 kg/cm^2

Elastic modulus (E): 14 - 24 x 10^5 kg/cm^2.

Fracture surface energy (γ): 1.4974 ergs/cm^2.

9. The mechanical behavior of the partially crystallized selenium can be explained completely with the existing theories for glass-ceramic and glass-crystal composites.

10. The fracture surface energy of partially crystallized selenium does not depend on the volume fraction or the size of spherulites. The fracture surface energy of amorphous selenium is approximately the same as that of partially crystallized selenium.

    (γ_{cry} = 1.4974 ergs/cm^2 and γ_{amo} = 1.6289 ergs/cm^2)

11. The ratio of calculated Griffith crack size to crystal diameter in partially crystallized selenium varies from 1.10 to 3.00 approximately. This ratio is

    a) 1.10 for composites having large-size crystals ($d_s \leq 50.8\mu m$),

    b) 1.71 for composites having medium-size crystals ($d_s \leq 50.8\mu m$), and

    c) 3.00 for composites having small-size crystals ($d_s \leq 15.0\mu m$).

12. The size of flaws present in amorphous selenium specimens is extremely small compared with the size of flaws in oxide glasses (5μm in amorphous selenium versus 50μm in oxide glasses).

LIST OF REFERENCES

LIST OF REFERENCES

1. R. S. Caldwell and H. Y. Fan, Phys. Rev., 114 664 (1959).
2. G. Briegleb, Z. Physik. Chem., A 144 321 (1929), referred as in W. C. LaCourse Ph.D. Thesis, RPI, New York.
3. H. Krebs, Fundamentals of Inorganic Crystal Chemistry (McGraw-Hill, London 1968), referred as in W. C. LaCourse Ph.D. Thesis, RPI, New York.
4. H. Krebs, Z. Für Naturforschg., 12b 795 (1957), referred as in W. C. LaCourse Ph.D. Thesis, RPI, New York.
5. O. Foss, Acta Chem. Scand., 7 1221 (1953), referred as in W. C. LaCourse Ph.D. Thesis, RPI, New York.
6. F. Tunistra, Ph.D. Thesis, Tech. Hogesch. Delft, Netherlands, (1967), referred as in W. C. LaCourse Ph.D. Thesis, RPI, New York.
7. L. A. Niman, V. D. Neff, R. E. Cantley and R. D. Butler, J. Mol. Spectry., 22 105 (1967), referred as in W. C. LaCourse Ph.D. Thesis, RPI, New York.
8. E. Mooser and W. B. Pearson, J. Phys. Chem. Solids, 7 65 (1958), referred as in W. C. LaCourse Ph.D. Thesis, RPI, New York.
9. R. E. Marsh, L. Pauling and J. D. McCullough, Acta Cryst., referred as in W. C. LaCourse Ph.D. Thesis, RPI, New York.
10. R. D. Burbank, Acta Cryst., 4 140 (1951).
11. A. Eisenberg and A. Tobolsky, J. Polymer Science, 46 19 (1960).
12. R. C. Keezer and M. W. Baily, Material Research Bull., 2 185 (1967).
13. B. Fitton and C. A. Griffiths, J. Appl. Phys., 39 No. 8, 3663 (1968).
14. K. H. Meyer and C. Ferry, Helv. Chim. Acta., 18, 570 (1935), referred as in W. C. LaCourse Ph.D. Thesis, RPI, New York.
15. A. Eisenberg and A. V. Tobolsky, J. Polymer Science, 61 483 (1962).
16. M. Polanyi, Z. Phys., 7 323 (1921), referred as in Ref. 34.
17. J. Frenkel, Z. Phys., 37 572 (1926), referred as in Ref. 34.

18. E. Orowan, Trans. Instn. Engrs. Shipb. Scot., 89 165 (1946).

19. C. E. Inglis, Trans. Instn. Nav. Archit., London, 55 219 (1913).

20. A. A. Griffith, Phil. Trans., A221 163 (1921).

21. A. A. Griffith, Proc. Int. Congr. Appl. Mech. (Delft) (1924).

22. R. A. Sack, Proc. Phys. Soc., Lond., 58 729 (1946).

23. H. A. Elliott, Proc. Phys. Soc., Lond., 59 208 (1947).

24. W. Weibull, Ingen.Vetensk.Akad. Handl., 151 153 (1949), as referred in Ref. 34.

25. J. C. Fisher and J. H. Holloman, Trans. Am. Inst. Met., 171 546 (1947).

26. R. J. Charles and J. C. Fisher, Non-Crystalline Solids, p. 491 (Wiley, New York 1960).

27. E. J. Saibel, J. Chem. Phys., 15 760 (1947).

28. P. Gibbs and I. B. Cutler, J. Am. Ceram. Soc., 34 200 (1951).

29. N. W. Taylor, J. Appl. Phys., 18 943 (1947).

30. E. Poncelet, Trans. Am. Soc. Math., 40a 201 (1948).

31. S. M. Cox, J. Soc. Glass Tech., 32 127 (1948).

32. J. C. Fisher, J. Appl. Phys., 19 1062 (1948).

33. W. Weibull, Ingen. Vetensk.Akad., Proc. 151 No. 153 (1939), as referred in Ref. 34.

34. W. D. Kingery, Introduction to Ceramics, p. 599 Table 17.1 (Wiley, New York 1967).

35. P. W. McMillan, Keynote Lectures, The Glass Phase in Glass-Ceramics, presented in the conference on the role of vitreous phases in technical materials, in Leeds 1972.

36. Z. Hashin, J. Appl. Mech., 29[1] 143 (1962).

37. Z. Hashin and S. Shtrikman, J. Mech. Phys. Solids, 11[2] 127 (1963).

38. F. F. Y. Wang, Matl. Sci. & Engg., 7 109 (1971).

39. R. C. Rossi, J. Am. Ceram. Soc., 51 433 (1968).

40. B. Paul, Trans. AIME, 218 36 (1960).

41. D.P.H. Hasselman and R. M. Fulrath, J. Am. Ceram. Soc., 48 No. 4 218 (1965).

42. D. P. H. Hasselman and R. M. Fulrath, J. Am. Ceram. Soc., 48 No. 10 548 (1965).

43. P. W. McMillan, S. V. Phillips and G. J. Partridge, J. Matls. Sci., 1 269 (1966).

44. H. L. McCollister and M. A. Conrad, "Fracture of Glass-Ceramics" presented at Annual Meeting of American Ceramic Society, (1966), as referred in Ref. 35.

45. D. P. H. Hasselman and R. M. Fulrath, J. Am. Ceram. Soc., 50 No. 8 399 (1967).

46. Y. Usumi and S. Sakka, J. Am. Ceram. Soc., 50 369 (1967).

47. D. P. H. Hasselman and R. M. Fulrath, Ceramic Microstructures, p. 343 (Wiley, New York 1965).

48. S. W. Freiman and L. L. Hench, J. Am. Ceram. Soc., 55 86 (1972).

49. E. B. Shand, J. Am. Ceram. Soc., 37 No. 2 52 (1954).

50. E. B. Shand, J. Am. Ceram. Soc., 37 No. 12 559 (1954).

51. A. Smekal, J. Soc. Glass Tech. Trans., 20 432 (1936).

52. J. B. Murgatroyed, J. Soc. Glass Tech., 26 22 155 (1942).

53. J. M. Barson, J. Am. Ceram. Soc., 51 No. 2 75 (1968).

54. E. Golz, Z. Phys., 120 773 (1943), referred as in Ref. 50.

55. E. B. Shand, J. Am. Ceram. Soc., 42 No. 10 474 (1959).

56. E. B. Shand, J. Am. Ceram. Soc., 44 No. 9 451 (1961).

57. Helmut Wallner, Ceram. Abstr., 19(6) 137 (1940).

58. A. Smekal, Ergeb. Exakt. Naturw., 15 106 (1936), referred as in Ref. 55.

59. N. Terao, J. Phys. Soc. Japan, 8 545-549 (1953).

60. W. C. Levengood, J. Appl. Phys., 29(5) 820 (1958) and Ceram. Abstr., 230i (1958).

61. L. Orr, Shand's Footnote ref. 55 p. 474.

62. R. W. Davidge and G. Tappin, J. Matls. Sci., 3 165 (1968).

63. W. J. Frey and J. D. Mackenzie, J. Matls. Sci., 2 124-130 (1967).

64. D. B. Binns, Science of Ceramics, p. 315 [Academic Press (1962)].

65. J. Selsing, J. Am. Ceram. Soc., 44 419 (1961).

66. W. D. Kingery, Introduction to Ceramics, p. 500 (Wiley, New York 1967).

67. ibid., p. 472, Table 14.1.

68. Y. Usumi and S. Sakka, J. Am. Ceram. Soc., 53 286 (1970).

69. E. Orowan, J. Welding, 34 157 (1955).

70. R. L. Bertolotti and R. M. Fulrath, J. Am. Ceram. Soc., 50 No. 11 558 (1967).

71. P. W. McMillan, Glass-Ceramics, p. 134 [Academic Press, London and New York (1964)].

72. S. V. Phillips, unpublished data Nelson Research Lab. (1962), referred as in Ref. 71.

73. M. Watanabe, R. V. Caporali, and R. E. Mould, "Symposium on nucleation and crystallization of glasses," Am. Ceram. Soc., 23-28 (1962), referred as in Ref. 71.

74. G. R. Irwin, Trans. ASM, 40A 147 (1948).

75. D. H. Winne and B. M. Wundt, Trans. ASME, 80 1643 (1958).

76. J. E. Srawley and W. F. Brown, ASTM (1964) and NASA TM X-52030 (1964).

77. B. Gross and J. E. Srawley, NASA REPORT, Tn-2603 (1965).

78. J. M. Corum, USAEC REPORT ORNL-4030 (1966).

APPENDIX

APPENDIX A

METHODS FOR DETERMINING FRACTURE SURFACE ENERGY OF GLASS AND GLASS-CRYSTAL COMPOSITES

The effective surface energy is defined in Section 1.2.2 as the work done to create unit area of new fracture face, not taking into account the fine-scale surface irregularities of the fracture face. For a given material, the effective surface energy (γ) is not necessarily the same at all stages in the fracture process. Davidge and Tappin[62] define γ_I as effective surface energy pertaining to the initiation of fracture, and γ_F as work of fracture, the value averaged over the whole fracture process.

γ_I is the value of γ appearing in the Griffith equation, and is related to the strain-energy release rate at the instant of fracture by

$$(\partial U/\partial A) \geq \gamma_I$$

where A is the area of new fracture face. $(\partial U/\partial A)$ may be obtained by theoretical or experimental methods. The theoretical method involves determination of $(\partial U/\partial A)$ from the mathematically-computed stress distribution around the notch for the particular specimen geometry. The experimental method derives $(\partial U/\partial A)$ solely from experimental load-deflection curves.

Theoretical Method

Let γ_G be the effective surface energy determined by this method, when the notch depth (c) is small compared with the beam depth (d). γ_G is given by Irwin[74] and Orowan[69] as

$$\gamma_G = -(\partial U/\partial A) = (1 - \nu^2)\pi \, \sigma_F^{\,2} c/2E \qquad [28]$$

where ν is Poisson's ratio,

E is Young's modulus, and

σ_F is the fracture stress.

Plane-strain conditions are assumed in deriving this equation. Equation 28 is essentially the original Griffith's equation.

Winne and Wundt[75] have presented corrections to the Equation 28 for the case when $c/d \geq 0.1$.

Srawley and Brown[76] have reviewed these mathematical treatments and represented the expressions in the form

$$\gamma_G = \frac{9(1 - \nu^2)\, P_F^{\,2} \ell^2 f(c/d)}{8EB^2(d - c)^3} \qquad [29]$$

where f(c/d) is a dimensionless parameter. At small arguments, $(c/d) \cong \pi c(d - c)^3/d^4$, and Equation 29 reduces to Equation 28. Figure 65 shows f(c/d) as a function of its argument, as calculated from results of Gross and Srawley[77] by Corum[78]. Figure 65 strictly applies only to beams deformed in four-point bending, but provided that $\ell \geq 8b$ approximately, corrections due to the shear stresses present during three-point bending are small [< 10%], as discussed by Srawley and Brown[76]. The effective surface energy γ_G can be determined using Equation 28 or the following equation:

Fig. 65. Plot of function f(c/d) versus c/d, as calculated from results of Gross and Srawley by Corum (Davidge and Tappin[62]).

Fig. 66. The general form of stiffness (K) versus crack area (A) plot (Davidge and Tappin[62]).

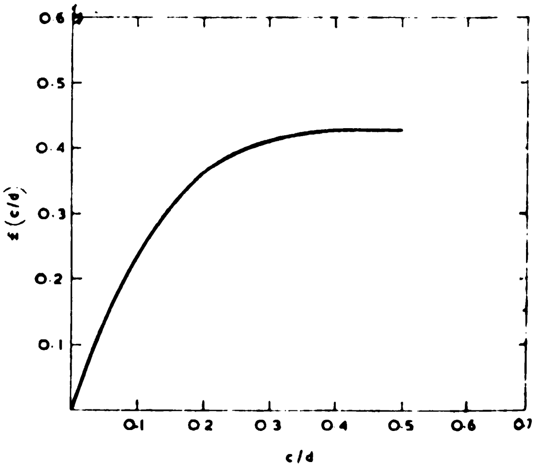
0.6
0.5
0.4
0.3
0.2
0.1
f(c/d)
0.1
0.2
0.3
0.4
0.5
0.6
0.7
c/d

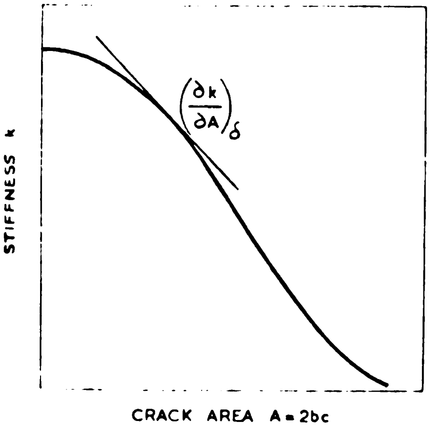
$\left(\frac{\partial k}{\partial A}\right)_\delta$
STIFFNESS k
CRACK AREA A = 2bc

$$\gamma_G = (1 - \nu^2)P_F^2F/E \qquad [30]$$

where $F = 91^2f(c/d)/8b^2(d-c)^3$. Values of F can be substituted in the above equation for different values of $f(c/d)$.

Experimental Method

Let γ_c represent the effective surface energy determined by the experimental method. This value should be equal to γ_G. The load-deflection curve in Figure 13 is given by $P = K\delta$, so that the stored energy at the instant of fracture is

$$V = P_F\delta_F/2, \text{ or } K\delta_F^2/2.$$

Now, γ_c equals $-(\partial U/\partial A)$, and fracture occurs at a fixed deflection. Then,

$$\gamma_c = -(\partial U/\partial K)_\delta \ (\partial K/\partial A)_\delta \quad .$$

But

$$(\partial U/\partial K) = \delta_F^2/2$$

and thus

$$\gamma_c = -\delta_F^2(\partial K/\partial A)/2 \quad . \qquad [31]$$

The specimen stiffness K is experimentally determined and plotted as a function of the initial crack area, $A = 2bc$. For each notch depth, $(\partial K/\partial A)$ is obtained from the slope of the curve at the appropriate value of A, as in Figure 66. Substitution of these values of $(\partial K/\partial A)$ in Equation 31 with the experimental values for δ_F thus gives a series of γ_c values for each notch depth.

Davidge and Tappin have determined the surface energy at the instant of fracture (γ_I) for four brittle materials, namely alumina, poly-methylmethacrylate, glass, and graphite. The theoretical and experimental methods for the determination of γ_I show good agreement. There is no variation of either γ_G or γ_c as a function of c/d, and both γ_G or γ_c show a scatter of up to ± 20% from the mean value. The values of γ_G and γ_c for a particular material are within 10 to 20% of each other. Davidge and Tappin conclude that γ_I values are highly dependent on the precise testing procedure, in particular on the initial distribution of crack sources. The values of γ_I determined, are strictly relevant only to specimens prepared and tested by the above method.